On the damage initiation in dual phase steels: Quantitative insights from *in situ* micromechanics

Dissertation

zur

Erlangung des Grades

Doktor-Ingenieurin

der

Fakultät für Maschinenbau

der Ruhr-Universität Bochum

von

Chunhua Tian

aus

Chongqing, China

Bochum, 2020

AFFIDAVIT

I declare in lieu of oath, that I wrote this thesis myself, using only literature cited in this volume.

15·12·2020

Datum

Chunhua Tian

Unterschrift

Acknowledgements

Finishing PhD! This is not the moment just saying farewell, but also the moment expressing my gratitude for all that support me during this special life experience.

The first one to whom I would like to express my high, respectful appreciation is my direct supervisor Prof. Dr. Christoph Kirchlechner. Without his helpful, insightful and thoughtful guidance, I could not smoothly finish my PhD. He gives intensive training on data processing, public presentation, scientific writing and paper publication. In particular, I learnt efficiency and power of programing skills in data analysing process. While I am not a confident person, my supervisor is always full of passion and encourages me to insist further in a very positive way.

I would like to give my sincere gratitude as well to Prof. Dr. Gerhard Dehm. He bestows me this precious chance to pursue a PhD degree in a highly prestigious research institute. Under his guidance, the SN&NG department has a very friendly comfortable working environment and very professional technical services. I enjoy a lot working here.

I am much grateful to my second supervisor Dr. Dirk Ponge, for the patient, inspiring discussions with his expertise in steel fields and the kind negotiation regarding the equipment access in MA department. I also thank Dr. Stefan Zaefferer for advice on EBSD doubts.

Leon Christiansen also contributes a lot to this work. As technician, he is always patient and ready to help whenever needed. Without his kind instruction, my PhD life could be tougher. Besides, I also thank Herr Andreas Sturm, Herr Uwe Tezins, Dr. Torsten Schwarz and Dr. Huan Zhao for instruction of APT sample preparation, APT operation and analysis. Thank Frau Heidi Bögershausen for ECCI and EPMA sample preparation, Frau Monika Nellessen for taking ECCI images and Frau Irina Wossack for EPMA.

My appreciation goes to my officemates and all colleagues as well, for such a pleasant memorable four years' hanging around, to my best friends Jing Rao, Juan Li for their constant companionship and encouragement, sharing both exciting and occasional depressing moments.

In the end, I am deeply grateful to my parents for bringing me to this wonderful world, to my grandparents for their selfless love in my childhood, to my younger brother for his consistent companionship from a toddler to a grownup as well as to my husband Liang for being there through thick and thin.

Abbreviations

APT	Atom probe tomography
BCC	Body centered cubic
CPFEM	Crystal plasticity finite element modelling
CRSS	Critical resolved shear stress
DIC	Digital image correlation
DP	Dual phase
EBSD	Electron backscatter diffraction
ECCI	Electron channelling contrast image
EPFM	Elastic plastic fracture mechanics
FCC	Face centered cubic
FEM	Finite element modelling
FIB	Focused ion beam
GND	Geometry necessary dislocation
HSLA	High strength low alloy
KAM	Kernel average of misorientations
LEFM	Linear elastic fracture mechanics
PAG	Prior austenite grain
RVE	Representative volume element
SEM	Scanning electron microscope
SRS	Strain rate sensitivity
TEM	Transmission electron microscope

YS	Yield strength
UTS	Ultimate tensile strength
V_m	Volume fraction of martensite
WD	Working distance

Nomenclature

a	Crack length
a_i	Crack length upon i_{th} unloading sequence
Δ*a*	Crack extension
A_{pl}	Plastic area under load displacement curve
B	Beam width
b_0	Initial ligament length
E	Elastic modulus
J	*J integral*
J_{el}	Elastic contribution to *J integral*
J_{pl}	Plastic contribution to *J integral*
J_{IC}	Critical fracture toughness of Mode I by *J integral*
K	Stress intensity factor
K_{IC}	Critical fracture toughness of Mode I by stress intensity factor
K_Q	Conditional fracture toughness
k_i	Specimen stiffness upon i_{th} unloading sequence
L	Beam length

n	Strain hardening exponent
η	Geometry dependent dimensionless constant
P_{max}	Maximum load point
r	Radius of a circle entered at the crack front
r_K	Size of K dominated zone
r_{pl}	Plastic zone size
θ	Angle with respect to crack plane
σ_y	Yield strength
$\sigma_{i,j}(r,\theta)$	Stress component dependent on r, θ
W	Beam thickness
v	Poisson's ratio

Abstract

This work aims to have a micromechanical investigation on damage initiation behaviors of dual phase (DP) steel, which finds wide application in the automobile field. Micro-submicro pillars and cantilevers were produced with focused ion beam and consecutively *in situ* tested in a scanning electron microscope.

Pillar compression tests were performed on ferrite to observe the activated slip systems and calculate the respective critical resolved shear stress (CRSS). Slip activation on all three plane families {110}, {112} and {123} occurs and their activation is primarily directed by Schmid factor, obeying Schmid's law. CRSS on {110}, {112}, {123} slip plane families is nearly identical, namely 147 ± 6, 143 ± 9 and 146 ± 4 MPa of 3 μm sized pillars, respectively. In spite of an identical ultimate tensile strength of two DP grades, ferrite shows a significant strength difference, which is mainly attributed to the dislocation density in two ferrite types, as observed by electron channeling contrast imaging (ECCI) technique. CRSS of ferrite also shows a size-scaling effect that might be closely related with the dislocation density gradient inside ferrite grains. Besides, strength of ferrite pillars exhibits a strong strain rate sensitivity (SRS) m valued as 0.054 ± 0.006 with an activation volume $13b^3$ to $16b^3$.

The extracted martensite pillars contain differently oriented substuctures and show a compressive yield strength as high as 3 GPa. They deform rather isotropically similar to polycrystals or occasionally block boundary sliding induced plastic deformation is observed. Martensite strength can be influenced by carbon distribution, which exists either as interstitial atoms or forms carbides in martensite of two DP800.

By micro cantilever bending tests, the conditional fracture initiation toughness of martensite islands is also obtained and valued as 10.1 ± 0.3 MPa.m$^{0.5}$ by stress intensity factor.

Based on our results, the two DP steel grades, despite similar martensite volume fraction and identical ultimate tensile strength, exhibit a big difference in the micromechanical properties of their phase components ferrite and martensite, which also leads to different damage behaviors. The current obtained results assist in further optimization of microstructures in the next period of DFG Transregios 188 „Damage in metal forming".

Kurzfassung

Ziel dieser Arbeit ist die mikromechanische Untersuchung der Schädigungsinitiierung in einem Dualphasenstahl (DP800), welcher vorwiegend in der Automobilindustrie Anwendung findet. Mikrometer und Submikrometer kleine Druck- und Bruchmechanikproben wurden hierfür mittels fokussierter Ionenstrahlen (FIB) in einzelne Körner des Dualphasenstahls geschnitten und anschließend durch *in situ* im Rasterelektronenmikroskop verformt.

Die Mikrodruckexperimente wurden zunächst mit Ferritproben zur Ermittlung der aktivierten Gleitsysteme und die jeweilige kritische Schubspannung (CRSS) durchgeführt. Auf Basis der Mikrodruckversuche konnte für 3 μm Mikrodruckproben gezeigt werden, dass die CRSS für das Versetzungsgleiten im Ferrit auf drei {110}, {112} und {123} Gleitebenenfamilien gleich ist, nämlich 147 ± 6, 143 ± 9 und 146 ± 4 MPa. Das schmidsche Schubspannungsgesetz behält seine Gültigkeit, d.h. ausschließlich die kritische Schubspannung dient als Kriterium für die Aktivierung von Versetzungsgleiten. Ein Normalspannungseinfluss konnte in den Druckversuchen nicht festgestellt werden. Trotz einer identischen makroskopischen Zugfestigkeit weisen Ferrit in zwei DP-stählen einen großen Unterschied in der kritischen Schubspannung auf. Mittels Elektronenchanneling konnte gezeigt werden, dass dies auf eine deutlich unterschiedliche Versetzungsdichte zurückzuführen ist. Die Mikrodruckproben zeigen ferner eine Größenabhängigkeit, welche zusätzlich zum klassischen Proben-Größeneffekt auf Versetzungsdichtegradienten zwischen dem Korninneren und Kornäußeren zurückgeführt wird. Die kritische Schubspannung der Ferritkörner weist ferner eine hohe Dehnungsgeschwindigkeitsempfindlichkeit 0.054 ± 0.006 auf, wodurch ein Aktivierungsvolumen von $13b^3$ bis $16b^3$ ermittelt wurde.

Die aus unterschiedlich orientierten Substrukturen bestehenden Martensitproben zeigen eine sehr hohe Druckfestigkeit von bis zu 3 GPa und verformen isotrop. Gelegentlich treten plastische Verformungen durch die Gleitphänomen entlang die Blockgrenzen auf. Die Druckfestigkeit der Martensitinseln wird sehr stark durch Kohlenstoff beeinflusst, welcher sowohl interstitiell als auch als Karbid in zwei unterschiedlichen DP800 Güten beobachtet wurde. Dies führt zu unterschiedlichen Martensit-Festigkeiten.

Final wurde die Bruchzähigkeit von Martensitinseln gemessen.

Es konnte gezeigt werden, dass die mikromechanischen Eigenschaften von zwei DP800 Güten, die einen vergleichbaren Martensitphasenanteil und eine makroskopisch identische

Zugfestigkeit besitzen, enorme Unterschiede hinsichtlich der Ferrit- und Martensitfestigkeit aufweisen, wodurch es zu einem signifikant unterschiedlichen Schädigungsverhalten bei gleicher makroskopischer Zugkurve kommt. Die in dieser Arbeit gewonnen Daten dienen zur weiteren Mikrostruktur- und Verformungsoptimierung im Zuge des DFG Transregios 188 „Damage in metal forming".

Contents

1 Introduction

1.1 Motivation

With a rocketing number of running vehicles in the past decades and in the future, automobile manufacturers are obligated to keep resource sustainable and reduce CO_2 emissions [1, 2]. One of the most direct and effective measures is designing lightweight vehicle parts to reduce energy consumption while maintaining the required safety standard. Dual phase (DP) steels, composed of ferrite matrix and dispersed martensite islands, have been a solution for the above mentioned issues, due to their outstanding features such as high strength to weight ratio, low yield strength over ultimate tensile strength and easily adjustable strength and high formability [3-5].

The understanding of failure process of DP steels is of great importance to further improve their mechanical properties. Different void nucleation sites are reported, including decohesion of ferrite-martensite phase boundary, cracking of martensite, debonding of ferrite grain boundaries and cracking or debonding of inclusions [6-9]. A large inconsistency exists concerning void formation mechanisms, which is ascribed to versatile factors in different literature reports, such as grain size, martensite volume fraction, martensite morphology and alloying elements [10-12]. Here, the commonly applied investigation techniques are *post mortem* scanning electron microscope (SEM) observation, digital image correlation (DIC) and X-ray tomography [6, 13]. In spite of certain contribution to recognition and understanding of damage processes through direct visualization, they provide rather phenomena' description and are unable to capture mechanical properties of individual phase components. Quantitatively determining mechanical properties of targeted ferrite and martensite can impart an intrinsic insight on different observed damage initiation modes in various literature reports and is even possible to explore a unified physically based material model considering all influential factors for prediction of damage mechanism(s) in a specific DP steel.

With the appearance of FIB milling technique and a prosperous development in micromechanical testing, it is nowadays of great convenience to perform localized investigation on a targeted feature, for instance, size-scaling effect of materials' strength, dislocation transmission through grain boundaries, fracture toughness of materials at small scale [14-16]. For DP steels, the first extractable and important information is CRSS, slip systems of ferrite and martensite. In a flawless ductile material without pre-cracks or pores, damage usually originates from strain incompatibility at preferential sites such as grain boundaries, phase boundaries and matrix-inclusion interfaces. Whether the local plastic deformation can

accommodate the load enforced geometry change and maintain the continuity of boundaries, strongly depends on respective plastic behavior of each involved component and the magnitude of their mechanical heterogeneity [17]. Hence, we are concerned with plasticity of our microstructure components.

For ferrite, the first focus is identification of activated slip systems which largely influences the strain accommodating capability in deformed polycrystals. Not as in face centered cubic (fcc) structure with unambiguous slip directions and slip planes, there always exists controversy on the activated slip plane in a body centered cubic (bcc) crystal. Despite determined slip directions ⟨111⟩, slip planes in bcc metals can be versatile, {110}, {112}, {123} or pencil glide [18, 19]. After identifying activated slip plane families, it matters further to verify the validity of Schmid's law and quantify their respective CRSS. Breakdown of Schmid's law is frequently discussed concerning the plastic deformation of bcc crystals. The non-glide stress component, as reported, might alter the core structure of screw dislocation and influence the glide stress CRSS [20, 21]. Whether non-Schmid behavior dominates in ferrite as well, therefore, requires a closer investigation. Well-known is that strength of bcc metals is strongly dependent on strain rate [22, 23], a critical variable in the forming process. The high SRS of strength is commonly attributed to the non-planar core structure of rate controlling screw dislocations [24]. However, little explored is the influence of strain rate on the activation of slip systems. Many research proposes that {110} are the elementary slip planes in bcc crystals and the other observed slip traces are comprised of intensive cross slips on {110} planes [25, 26]. Change of strain rate might have an influence on the consistent cross slip process and finally on the observed activated slip systems.

The yield strength and plastic deformation behavior is of particular interest for martensite. The mechanical heterogeneity between ferrite and martensite affects strain partitioning in two phases, requiring geometry necessary dislocations (GND) for compatible deformation at phase boundaries, which directly influences the damage initiation sites [27]. Decrease in martensite strength can reduce the void formation through enhancing co-deformation of ferrite and martensite [28]. Through DIC technique, significant strain in martensite was observed [6]. However, the underlying plastic deformation mechanism was not clearly identified because of limited DIC resolution. Micro tensile tests on bulk martensite show that plasticity is assisted by sub boundary sliding in lath martensite [29]. Whether the sliding phenomenon occurs as well in martensite of DP steels needs further investigation,

16

While plasticity of microstructure components plays the key role in initiation of damages, what matters further for a damage tolerant material is the fracture resistance of initiated defects. Widely accepted is that martensite islands act as one of the most frequent damage initiation sites in DP steels, through rather brittle breaking. However, a quantitative determination of its fracture toughness is still pending. Microscale fracture testing, in particular of non-linear elastic materials, is still confronted with big challenges. Current investigations on small scale elastic plastic fracture mechanics (EPFM) are mostly conducted on several model materials such as ultrafine grained tungsten and tungsten single crystals [30, 31]. Extracting fracture toughness of one targeted feature from an industrially applied material is still rare.

In this work, we will mainly apply pillar compression for plasticity investigation on both ferrite and martensite, while micro cantilever bending tests for fracture toughness capture of martensite islands. All micro samples are fabricated by FIB milling.

1.2 Objective

This work, from micromechanics perspective, strives for understanding damage initiation behaviors of DP steels. The following points should be answered:

1) How large is the mechanical heterogeneity of ferrite and martensite? How does this affect damage initiation and growth in DP steels? (Q1)

2) What is the influence of strain rate on activation of slip system in ferrite? (Q2)

3) What is the fracture initiation toughness of martensite islands? (Q3)

1.3 Strategy

We aim at understanding damage initiation in DP steels from a micromechanical view. *In situ* pillar compression tests on ferrite and martensite samples, capturing plasticity of phase components, are performed using an ASMEC indenter system. All these micro specimen were Ga^+ ion milled, mainly using a Zeiss Auriga® dual beam FIB. *In situ* micro cantilevers tests are conducted with a Hysitron indenter system equipped with a wedge shape tungsten carbide tip. All *in situ* experiments are recorded in a Zeiss Gemini500 field emission microscope. Electron backscatter diffraction (EBSD) technique is applied to determine crystal orientations of ferrite pillars and martensite substructures. We conduct also ECCI for a qualitative observation of dislocation distribution from ferrite grain interior to phase boundary and for a quantitative estimation of dislocation density in ferrite of each steel grade. Further, in order to have an

17

atomic insight on elements' content and distribution, atom probe tomography (APT) is generated on a CAMECA local electrode atom probe LEAP^{TM} 5000 XR.

1.4 Structure of the thesis

Directly after the introduction chapter, summarized in Chapter 2 is the literature review on DP steels and fundamental theoretical knowledge closely pertinent to the current work. In Chapter 3, all the applied experimental procedures are described in detail. Chapter 4 presents results on plasticity of ferrite and martensite, which are already published as *Tian C, Ponge D, Christiansen L, Kirchlechner C, On the mechanical heterogeneity in dual phase steel grades: Activation of slip systems and deformation of martensite in DP800 [J]. Acta Materialia, 2020, 183: 274-284.* Chapter 5 discusses the influence of strain rate on the activation of {110}, {112}, {123} slip in ferrite, which is published as *Tian C, Dehm G, Kirchlechner C. Influence of strain rate on the activation of {110},{112},{123} slip in ferrite of DP800[J]. Materialia, 2020: 100983.* Chapter 6 reports on the fracture toughness of martensite islands, accepted by JMR. In the end, we will summarize our present work and give perspectives that requires further investigation for understanding damage behaviors of DP steels.

2 Literature review and theoretical background

2.1 DP steel

2.1.1 Typical Features

The terminology "dual phase" was coined in the 1970s [5] to describe ferrite-martensite microstructures. This type of steel first drew attention and much research interest upon urgent demands in the US automotive industry to reduce the weight for an energy sustainable perspective and still maintain sufficient strength for the safety potential [4, 5]. In 2015, DP steels were reported to hold a market segment up to one third in automotive parts that exceeds High Strength Low Alloy (HSLA) steels [4] because they exhibit the following typical features.

DP steels are first characterized by continuous yielding behavior and a low ratio of yield strength/tensile strength (YS/TS) as low as 0.4-0.5, which are two intrinsic features. YS represents the stress beyond which plastic deformation begins while UTS is the maximum stress reached during a tensile test before fracture. A comparison between continuous and discontinuous yielding is schematically illustrated in Fig. 2.1 regarding engineering stress versus engineering strain. The YS and UTS in the case of the continuous yielding are labelled out as well as the upper/lower yield point in the case of discontinuous. The absence of upper/lower yielding point can guarantee a homogeneous strain distribution and hence better surface quality while the low ratio of YS/TS facilitates deformation and forming processes [5]. The presence of both characteristics, namely continuous yielding and low YS/TS ratio, can be attributed to the high density of mobile dislocations generated in ferrite due to local volume expansion during martensite formation as experimentally observed with ECCI [3, 4, 32]. A dislocation density gradient exists from the interior of ferrite grain to the region close to martensite. This explanation using mobile dislocations is further supported by tempering DP steels [33]. After tempering at high temperatures above $500\ ℃$, overall dislocation density is largely reduced so that a discontinuous yielding returns. Additionally, a lower limit of martensite volume fraction exists from 3% to 15%, depending on M_s (martensite starting) temperature to guarantee a continuous yielding behavior [4]. Another explanation for low YS and continuous yielding is the assisting effect of the internal stress in the ferrite phase by the martensitic transformation [34], where plastic deformation can occur simultaneously at many sites. YS of DP steels have a similar dependence on martensite fraction as TS.
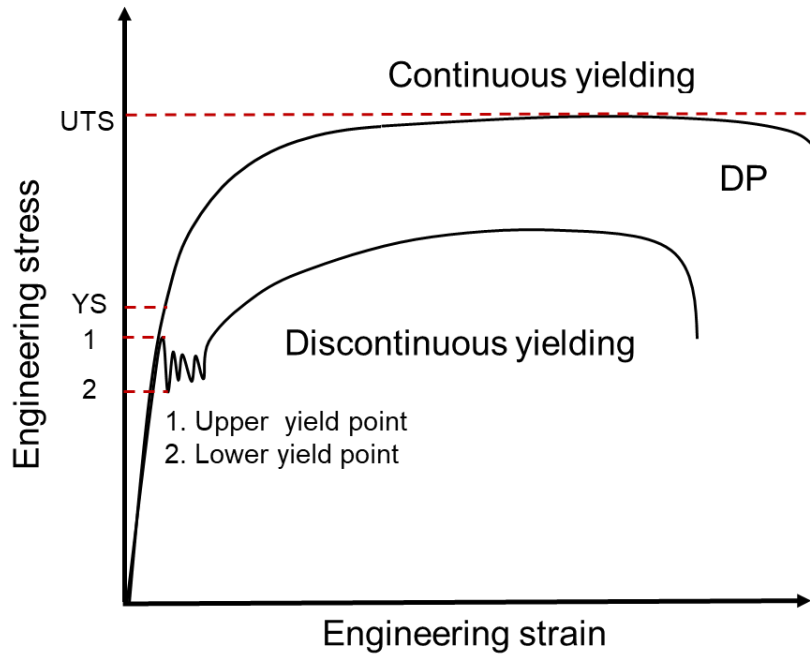
Fig. 2.1 Schematic illustration of engineering stress versus engineering strain curves representative of continuous and discontinuous yielding.

The low ratio of YS/TS implies another important feature of DP steels, high initial work hardening rate [35, 36], which means a high flow stress/strength can be reached after forming, benefitting fatigue and crash resistance even with a reduced thickness. The high initial work hardening rate results also from high density of dislocations that induce strong dislocation interaction at the beginning of ferrite deformation [4].

Furthermore, DP steels have an adjustable high tensile strength (TS) ranging from 450 MPa to 1200 MPa. It is possible to change their strength either through grain size according to the well-known Hall-Petch relationship [37, 38], or more importantly through changing the volume fraction of martensite V_m. V_m is closely related with TS of DP steel that generally increases with martensite phase fraction [4, 39]. There are following alternatives to raise the martensite amount, namely by increasing carbon content, by increasing the quenching temperature and by adding such alloying element as Mo, Mn or V increasing hardenability [12, 40]. However, with an increase in volume fraction, martensite islands will contain a declining carbon content that can cause a decrease in martensite strength [39]. Whether this variance in strength influences on tensile strength of DP steels is still not thoroughly clear. Some found that the intrinsic strength of martensite islands has negligible impact on tensile strength of DP steels [40, 41] while others claimed there exists an maximum tensile strength value at a certain volume fraction of martensite [39, 42, 43].

2.1.2 Martensite in DP steels

It is established that martensitic transformation is a diffusionless process, in which the neighboring atoms remain the same with a specific orientation relation as outlined below. In Fe-C steels, depending on carbon content, different morphologies are observed, frequently including lath martensite at low to medium carbon level ($< 0.6\ wt.\%\ C$) and lenticular martensite in high carbon ($> 1.0\ wt.\%\ C$) steels [44-46]. DP steels typically contain a carbon content of 0.06 - 0.15 wt.% [3] and martensite in DP steels shows lath morphology [47].

The hierarchical structures of lath martensite are schematically shown in Fig. 2.2 with variants formed in one prior austenite grain (PAG). If all variants are formed, a PAG consists of four packets, and in each packet there are three blocks. Each block are composed of two sub-blocks, inside which small laths are arranged with alternating orientation changes of 3-5 degrees [44, 48]. These substructures do not randomly arrange but follow Kurdjumov-Sachs ($K - S$) orientation relationship with PAG. The $\{110\}_{\alpha\prime}$ planes of the formed martensite are parallel to $\{111\}_{\gamma}$ in PAG and the $\langle 111 \rangle_{\alpha\prime}$ directions parallel to $\langle 110 \rangle_{\gamma}$. This is further explained by the schematic drawing in Fig. 2.3, in which the orientation relationship between martensite within a packet and the parent austenite is shown. One $\{111\}_{\gamma}$ plane can have six martensite variants (variant equals to sub-block) and PAG with fcc structure has four $\{111\}_{\gamma}$ planes so that 24 variants are possible to originate from one single PAG [44, 45]. The packet is accordingly characterized by a bunch of blocks with a common $\{111\}$ habit plane from PAG and the blocks in one packet align themselves differently as shown in Fig. 2.3.
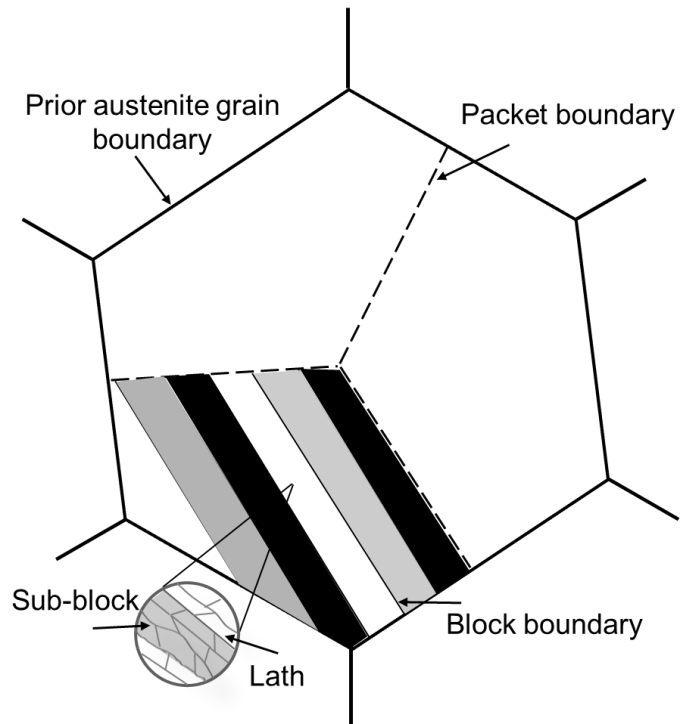
Fig. 2.2 Schematic illustration of the hierarchical lath martensite formed inside one PAG, redrawn from [44].
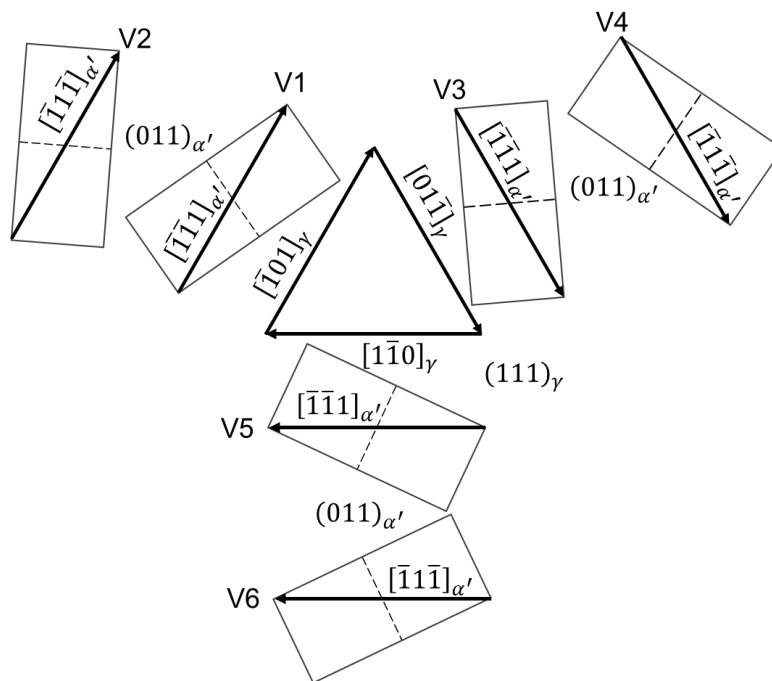

Fig. 2.3 Six crystallographic variants evolved from (111) austenite plane according to $K-S$ orientation relationship. The triangle and the rectangles represent (111) and (011) plane of austenite and martensite, respectively. On (111) plane, three $\langle 110 \rangle_\gamma$ directions can be found.

Table 2-1 The 24 crystallographic variants of $K-S$ orientation relationship and the misorientation angle with respect to V1 [45].

Variant	Plane parallel	Direction parallel	Rotation axis from V1	Angle [°]
V1	$(111)_\gamma \parallel (011)_{\alpha'}$	$[\bar{1}01]_\gamma \parallel [\bar{1}\bar{1}1]_{\alpha'}$	———	
V2		$[\bar{1}01]_\gamma \parallel [\bar{1}1\bar{1}]_{\alpha'}$	$[0.577\ 0.577\ -0.577]$	60.00
V3		$[01\bar{1}]_\gamma \parallel [\bar{1}\bar{1}1]_{\alpha'}$	$[0.\ 0.707\ 0.707]$	60.00
V4		$[01\bar{1}]_\gamma \parallel [\bar{1}1\bar{1}]_{\alpha'}$	$[0-0.707-0.707]$	10.53
V5		$[1\bar{1}0]_\gamma \parallel [\bar{1}\bar{1}1]_{\alpha'}$	$[0-0.707-0.707]$	60.00
V6		$[1\bar{1}0]_\gamma \parallel [\bar{1}1\bar{1}]_{\alpha'}$	$[0\ 0.707\ 0.707]$	49.47
V7	$(1\bar{1}1)_\gamma \parallel (011)_{\alpha'}$	$[10\bar{1}]_\gamma \parallel [\bar{1}\bar{1}1]_{\alpha'}$	$[-0.577\ -0.577\ 0.577]$	49.47
V8		$[10\bar{1}]_\gamma \parallel [\bar{1}1\bar{1}]_{\alpha'}$	$[0.577\ 0.577-0.577]$	10.53
V9		$[\bar{1}\bar{1}0]_\gamma \parallel [\bar{1}\bar{1}1]_{\alpha'}$	$[-0.615\ 0.186-0.767]$	50.51
V10		$[\bar{1}\bar{1}0]_\gamma \parallel [\bar{1}1\bar{1}]_{\alpha'}$	$[-0.739\ -0.462\ 0.490]$	50.51
V11		$[011]_\gamma \parallel [\bar{1}\bar{1}1]_{\alpha'}$	$[0.933\ 0.354\ 0.065]$	14.88
V12		$[011]_\gamma \parallel [\bar{1}1\bar{1}]_{\alpha'}$	$[-0.357\ 0.603\ 0.714]$	57.21
V13	$(\bar{1}11)_\gamma \parallel (011)_{\alpha'}$	$[0\bar{1}1]_\gamma \parallel [\bar{1}\bar{1}1]_{\alpha'}$	$[0.354-0.933-0.065]$	14.88
V14		$[0\bar{1}1]_\gamma \parallel [\bar{1}1\bar{1}]_{\alpha'}$	$[-0.490\ 0.462-0.739]$	50.51
V15		$[\bar{1}0\bar{1}]_\gamma \parallel [\bar{1}\bar{1}1]_{\alpha'}$	$[-0.738-0.246\ 0.628]$	57.21
V16		$[\bar{1}0\bar{1}]_\gamma \parallel [\bar{1}1\bar{1}]_{\alpha'}$	$[0.659-0.659-0.363]$	20.61
V17		$[110]_\gamma \parallel [\bar{1}\bar{1}1]_{\alpha'}$	$[-0.659\ 0.363-0.659]$	51.73
V18		$[110]_\gamma \parallel [\bar{1}1\bar{1}]_{\alpha'}$	$[-0.719-0.302\ 0.626]$	47.11
V19	$(11\bar{1})_\gamma \parallel (011)_{\alpha'}$	$[\bar{1}10]_\gamma \parallel [\bar{1}\bar{1}1]_{\alpha'}$	$[-0.186\ 0.767\ 0.615]$	50.51
V20		$[\bar{1}10]_\gamma \parallel [\bar{1}1\bar{1}]_{\alpha'}$	$[0.357\ 0.714-0.603]$	57.21
V21		$[0\bar{1}\ \bar{1}]_\gamma \parallel [\bar{1}\bar{1}1]_{\alpha'}$	$[0.955\ 0-0.296]$	20.61
V22		$[0\bar{1}\ \bar{1}]_\gamma \parallel [\bar{1}1\bar{1}]_{\alpha'}$	$[-0.302\ 0.626\ 0.719]$	47.11
V23		$[101]_\gamma \parallel [\bar{1}\bar{1}1]_{\alpha'}$	$[-0.246-0.628-0.738]$	57.21
V24		$[101]_\gamma \parallel [\bar{1}1\bar{1}]_{\alpha'}$	$[0.912-0.410\ 0]$	21.06

The detailed orientations of the martensite variants and misorientation angles with respect to V1 are listed in Table 2-1. V1 and V2 share the twin relationship, and the smallest

misorientation angle is 10.53°, which relates V1 and V4. This pair variants (sub-blocks) with the smallest misorientations normally stay together and form blocks. A further key information is most of sub-boundaries inside the lath martensite are high angle boundaries larger than 15° [49], which raised great interest in studying its deformation behavior [48, 50, 51]. By micro tension tests, lath martensite is observed to deform plastically either though intra lath crystallographic slip or though the apparent boundary sliding mechanism, depending on the ratio of the maximum in-plane Schmid factor of retained austenite and the maximum out-of-plane Schmid factor [51]. All sub-boundaries including lath, sub-block and block boundaries are possible to activate the boundary sliding mechanism [29]. This interfacial plasticity is also reported in [50] and strengthened further by an optimal 45 °alignment of interfaces with respect to the loading axis.

The orientations of all the 24 martensite variants can be presented by the pole figures obtained by EBSD. In Fig. 2.4, the {100} poles of all 24 variants originated from one PAG with orientation ⟨001⟩{100} are illustrated and the red squares, which are located at the center of each Bain zone, represent uniquely the PAG orientation. For a random PAG orientation, this Bain zone will also change along as shown in Fig. 2.4b. Based on this fact, one can reconstruct the PAGs and label the variants combined with the different colors from EBSD [45]. This method, however, has some deficiencies. First, it requires the existence of a large amount of variants to form a relatively clear Bain zone and is unable to acquire the exact PAG orientation angles. Further, the inaccuracy of EBSD data brings also difficulties in identifying variants or reconstruction of PAGs. Another method based on the transformation matrix can be applied which only needs more than three variants to clearly reconstruct PAGs with known orientation [52].
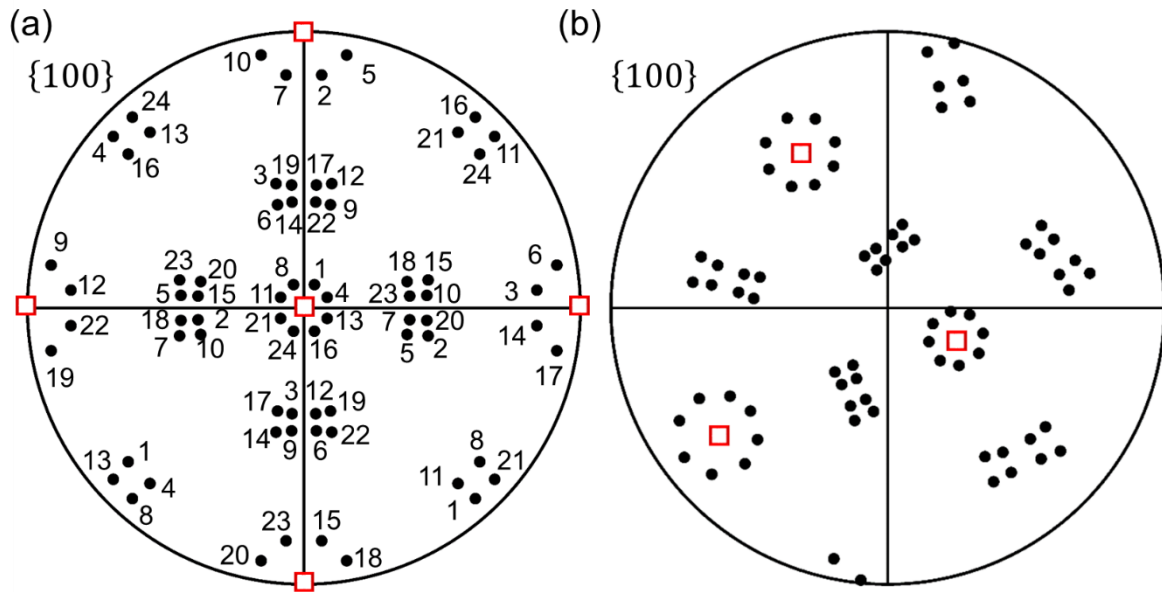
Fig. 2.4 (a) {100} pole figures showing the 24 martensite variants' orientation formed from one austenite with orientation ⟨001⟩{100} and (b) from one austenite of random orientation. The red squares denote the Bain zone, formed by austenite {100} poles. Drawn by mathematica following the orientation transformation matrix.

2.1.3 Processing route of DP steels

The core step to produce DP steels is the so-called intercritical annealing (IA) heat treatment. Hereby, the initial material is heated up to the ferrite and austenite two-phase zone, namely between A_1 and A_3 temperature range, where austenization takes place, respectively. This is labelled out on the iron-carbon (Fe_3C) phase diagram as in Fig. 2.5, where ferrite and austenite coexist. After holding for a certain duration, a quenching step is conducted to transform the austenite into martensite so that a ferrite-martensite microstructure is obtained.

The initial microstructures for IA heat treatment can be versatile. Three different heat treatment routes for DP steels are schematically shown in Fig. 2.6, namely the intermediate quenching (IQ), single IA and step quenching (SQ) [53, 54]. In the IQ route (Fig. 2.6a), a full austenization step is performed and quenched martensite acts as the starting microstructure for the following IA. Since the quenched martensite has lath structures, austenite nucleates preferentially along lath boundaries in the IA step, which finally results in a fibrous martensite morphology in the DP steels (Fig. 2.7a). For the single IA route (Fig. 2.6b), the initial microstructure is frequently ferrite-pearlite, where austenite prefers to nucleate at ferrite/carbide interfaces. Fine globular martensite distributing along ferrite grain boundaries is the resulting microstructure (Fig. 2.7b).

However, with ferrite-pearlite as the initial microstructure in the industrial manufacturing involving hot rolling and cold rolling, a banded martensite morphology is the common case. This is attributed to the segregation of alloying elements, in particular manganese, during the dendrites' formation of solidification step. Aligned with those dendrites, alternate lean and rich manganese bands are formed. Carbon redistributes and pile up at the rich manganese region, which provides a preferential site to nucleate pearlite. These features are inherited through hot rolling and cold rolling. High cooling rates avoiding pearlite formation can hide band morphology [55, 56]. In the SQ route, after full austenization, the sample is directly cooled into the two-phase region. In a full austenite state, ferrite will first nucleate at austenite grain boundaries and grow into austenite. The resulting structure is coarse martensite surrounded by ferrite (Fig. 2.7c).
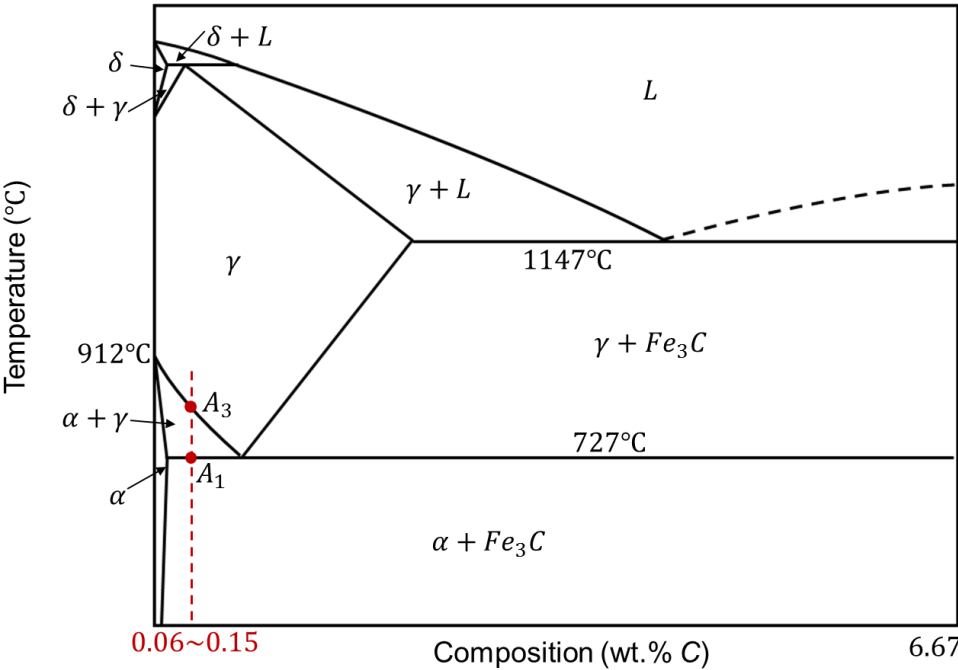

Fig. 2.5 Metastable iron-carbon phase diagram showing the A_1, A_3 and the intercritical region, redrawn and revised from [57].
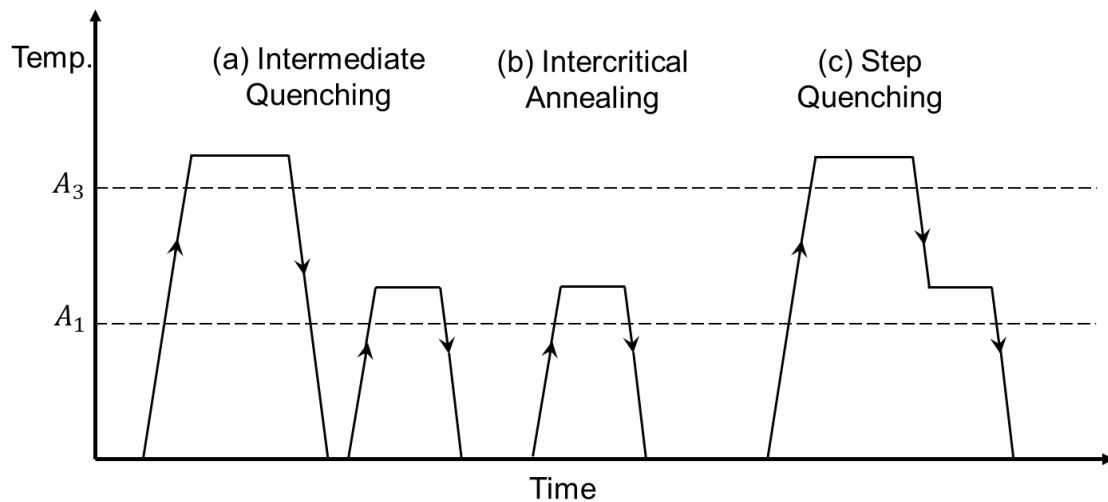
26

Fig. 2.6 Schematic three heat treatments for DP structure generation: (a) intermediate quenching, (b) intercritical annealing and (c) step quenching. Redrawn from [54].
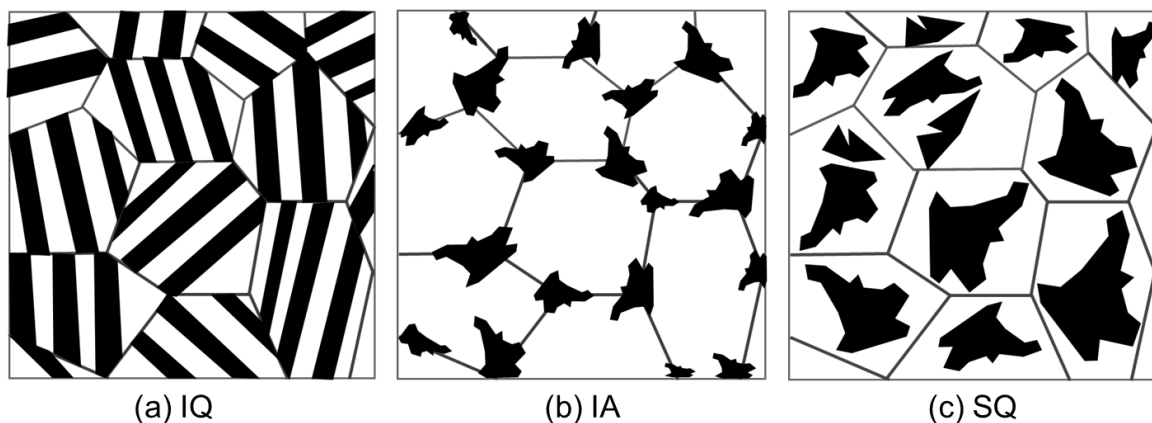

Fig. 2.7 Schematic typical microstructure features corresponding to each heat treatment route: (a) IQ, (b) IA and (c) SQ. The black regions represent martensite and the white ones stands for ferrite, drawn based on descriptions and micrographs in [54].

2.1.4   Fracture mechanisms in DP steels

Two main fracture mechanisms are responsible for the failure of DP steels, namely, transgranular cleavage fracture and ductile fracture, depending on grain size, martensite volume fraction, martensite hardness as well as the phase morphology of martensite [53, 54, 58, 59]. The fractography of cleavage fracture is characterized by river patterns and relatively smooth facets. Since cleavage fracture includes bonds' breaking, a sufficient high stress, which could be realized by local discontinuity such as microcracks or inclusions, should be present to initiate

this process. Additionally, planes with low packing density are preferred and for bcc cleavage planes are {100} type [60]. Ductile fracture typically includes three stages, void nucleation around hard particles, void growth and void coalescence. Its fractography is featured by dimple morphology [60].

DP steels with large grains reaching dozens of micrometers frequently fracture in cleavage mode [53, 58]. Its initiation site is mainly the breaking of martensite, especially in a banded state, caused by constrained plastic flow in ferrite [59]. The microcracks in martensite can provide stress concentration for further growth into ferrite. According to the formed facet size, the effective grain size for cleavage fracture is reported to be either the prior austenite size or the prior ferrite size corresponding to IQ or IA in Fig. 2.6 [53]. In spite of large grains, it is still possible to adjust the fracture mechanism by changing the phase morphology or by tempering heat treatment. A phase morphology with ferrite surrounding martensite (isolated martensite) as obtained in SQ tends to facilitate ductile fracture [58, 59], which can be also realized by tempering to reduce martensite hardness. In most cases, with an increase of martensite volume fraction, ductility and fracture toughness are deteriorated. However, when its carbon content and defects inside decrease and martensite arrives at a softer state, an increasing trend of impact energy can be observed with a rising amount of martensite volume fraction and ductile fracture occurs [43]. During ductile fracture, the void nucleation sites can be versatile, most frequently at martensite/ferrite phase boundaries, or inclusion/ferrite boundaries [6, 9].

2.2 Dislocation based plasticity of bcc materials

2.2.1 Core structure of screw dislocation

The anomalous behaviors of bcc materials compared to fcc, such as breakdown of Schmid's law [61, 62], compression-tension asymmetry [63, 64], strong temperature dependence [65], large SRS [66], solute defects softening phenomenon [67-69], can be attributed to the core structure of screw dislocations, which are believed to control the plastic deformation of bcc structures [70-72]. As cited in [73], Hirsch was the first to put forward the suggestion that the $\frac{1}{2}a\langle 111 \rangle$ screw dislocation might be sessile due to the three-fold symmetrical dissociation of the dislocation core.
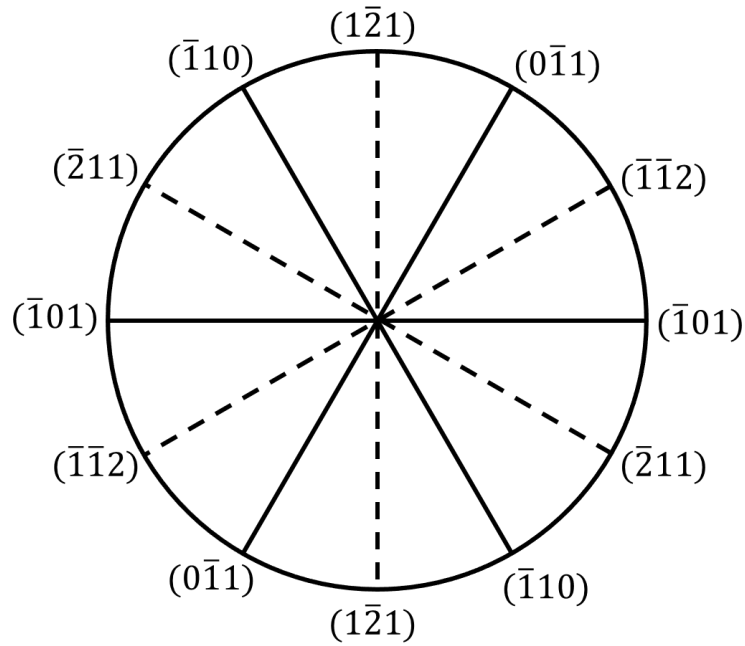
$(1\bar{2}1)$

$(\bar{1}10)$ $(0\bar{1}1)$

$(\bar{2}11)$ $(\bar{1}\bar{1}2)$

$(\bar{1}01)$ $(\bar{1}01)$

$(\bar{1}\bar{1}2)$ $(\bar{2}11)$

$(0\bar{1}1)$ $(\bar{1}10)$

$(1\bar{2}1)$

Fig. 2.8 [111] stereographic projection showing orientations of all {110} and {112} planes belonging to [111] zone axis, reproduced from [61].

Generally, despite of controversial slip planes in bcc metals, the Burgers vector is unambiguously considered as $\frac{1}{2}a\langle 111\rangle$ (a the lattice constant). The $\langle 111\rangle$ direction is an axis of threefold symmetry and each $\langle 111\rangle$ zone consists of three {110} and three {112} planes as shown in Fig. 2.8. For a better visualization of atoms' arrangement along a $\langle 111\rangle$ direction, the bcc crystal is considered as a hexagonal lattice of $\langle 111\rangle$ columns with a lattice parameter $\sqrt{\frac{2}{3}}a$ that can be calculated [71, 72], as schematically depicted in Fig. 2.9 along [111] direction. Note that the different colors mean atoms at various Z altitude along this zone axis. Atoms in three first-neighbor columns forming an upward triangle as in Fig. 2.9 and each of the three atoms has the reference altitudes of $0, \frac{b}{3}, \frac{2b}{3}$ when turning clockwise in the triangle.
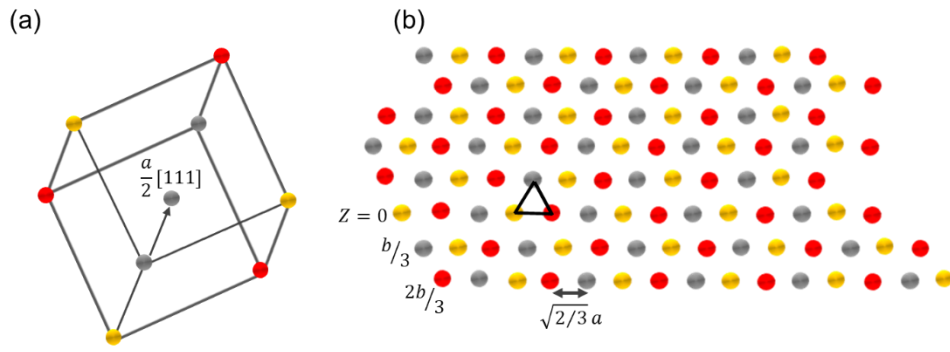
Fig. 2.9 (a) A bcc unit cell showing [111] axis. (b) The hexagonal lattice formed by atoms stacking along the [111] axis. Different colors represent atoms at different altitude. Redrawn from [71].

Atomistic simulation contributed tremendously to understanding the core structure of screw dislocations [73-76]. Generally, screw dislocations in bcc metals split neither on {110} nor on {112} planes to form well-defined partials and stacking faults like in fcc crystals [74]. They rather spread the core structure onto three nonparallel {110} planes according to the crystallography symmetry such as the threefold axis ⟨111⟩ and ⟨101⟩ diad. Depending on the adopted modelling schemes or on alloying elements, two types of core structure were reported, the asymmetrical and symmetrical one [74] as shown in Fig. 2.10, which is a differential displacement map to have a better visualization of core structure in atomic simulations as introduced in the previous section [73, 75]. The length of arrows linking two first neighbor columns as in Fig. 2.9, is proportional to the displacement difference induced by the screw dislocation along the ⟨111⟩ direction between two columns. The arrow is so directed from column of smaller displacement to that of larger displacement. In the core structure in Fig. 2.10a, the displacement map is invariant by the threefold symmetry of ⟨111⟩ axis, however, short of ⟨101⟩ diad symmetry. Therefore, the asymmetrical core structure has two variants related by the ⟨101⟩ diad (upper and lower in Fig. 2.10a), which is called degenerate. By contrast, the symmetrical core structure maintains both symmetry operation and keeps invariant so that it is called nondegenerate.
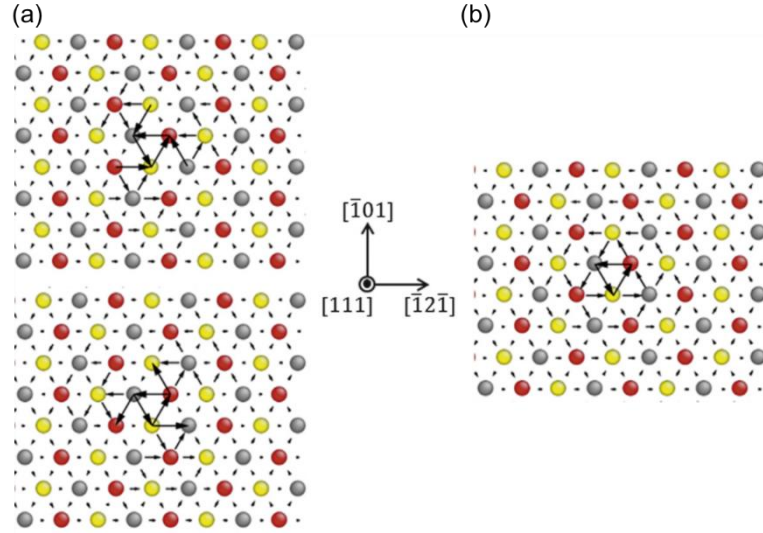
Fig. 2.10 (a) Asymmetrical and (b) symmetrical core structure, depicted by differential displacement maps [71].

2.2.2 Breakdown of Schmid law

Dislocations moving in a single crystal are subjected to hindering friction forces that can be described by Peierls-Nabarro model [77] as Eq. (2.1).

$$\tau_p = \frac{2G}{1 - v} exp\left(-\frac{2\pi}{(1 - v)}\frac{d}{b}\right)$$

(2.1)

Here, τ_p the Peierls stress, G the shear modulus, d lattice spacing and b Burgers vector. Hence, according to the Eq (2.1), a combination of slip plane and slip direction should have largest lattice spacing and smallest slip distance. For fcc structures with both closest packed planes and directions, dislocations move unambiguously on 12 slip systems $\{111\}\langle 110\rangle$. By contrast, bcc materials have only closest packed direction $\langle 111\rangle$ so they have more possible slip systems including 48 in total, $\{110\}\langle 111\rangle$, $\{112\}\langle 111\rangle$, $\{123\}\langle 111\rangle$ [18, 49] or maximum resolved shear stress plane (MRSSP) or general non-crystallographic orientations.

Among the slip systems, the firstly activated one upon loading is well predicted by Schmid law for fcc structures. It states that the shear stress upon which dislocations start to move is called the critical resolved shear stress τ_0 (CRSS) and this value should be the same for every equivalent slip system and independent on the shearing sense [78]. The resolved shear stress (RSS) imposing on dislocations to move equals the normal stress applied to the single crystal multiplied by Schmid factor [78] as Eq.(2.2),

$$\tau = \sigma \cdot \cos \lambda \cos \kappa \qquad\qquad (2.2)$$

Herein τ is the resolved shear stress, σ the applied normal stress, λ the angle between the applied stress with slip direction and κ with the slip plane normal as schematically shown in Fig. 2.11. The product $\cos \lambda \cos \kappa$ is called Schmid factor m.

However, non-Schmid behavior is frequently reported in bcc metals and almost regarded as one typical feature of their plastic deformation. The breakdown of Schmid law in bcc metals is mainly divided in two categories [61, 62, 75]. The first is due to intrinsic effects caused by the lattice symmetry feature, stating that the CRSS varies from each other when the plane and direction of slip is changed, in particularly reflected by the so-called twinning-antitwining (TAT) slip asymmetry on the slip planes {112}, where CRSS is typically lower in the twining shearing sense than the antitwinning sense. This TAT slip asymmetry, however, does not occur in {110}⟨111⟩ slip systems, since the bcc structure possesses ⟨110⟩ axis diad symmetry. The other category is the extrinsic effect, where CRSS can change when the applied stress tensors other than the glide shear stress are present. This non-glide shear stress component perpendicular to the slip direction can alter the core structure of the screw dislocation by interaction with those small edge dislocation components in the course of general core dissociation. Moreover, according to the atomic simulation, metals with nondegenerate core structure as shown in Fig. 2.10b exhibit a smaller TAT asymmetry and weaker dependence on the non-glide stress component. Although the atomistic simulation to investigate and observe these features is in most cases conducted on solid dislocations at zero temperature without considering the kink pair mechanism, the properties of solid dislocations are believed to be similar at the finite temperature, at least qualitatively [75].
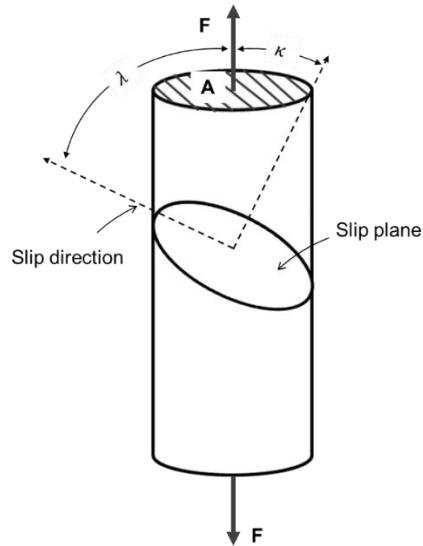
Fig. 2.11 Schematic description of geometry relation in Schmid law, redrawn according to [49].

2.2.3 Peierls process

Peierls first put forward that a straight dislocation has the lowest energy when it lies at the Peierls' potential valley as schematically shown in Fig. 2.12, which varies periodically on the slip plane [79, 80]. When the dislocation is displaced from this valley position, the configuration of atoms in its core is altered and its energy increases. Different functions were put forward to describe the potential variation, including the most common sinusoidal potential, Eshelby potential, antiparabolic potential and the abrupt potential (Fig. 2.12). Under the sinusoidal periodicity, the potential shape between two valleys was further reported to have two variants, one with single maximum and one with a camel-hump depending on the applied models [81, 82]. The camel-hump potential shape is labelled out on Fig. 2.12 as well. Iron, for example, by DFT starting from the first principle quantum-mechanical description, shows a single maximum. By contrast, using the interatomic interactions, a camel hump shows on the Peierls potential [82, 83]. Further, the shape and height of Peierls' potential can be influenced by the applied force [84].
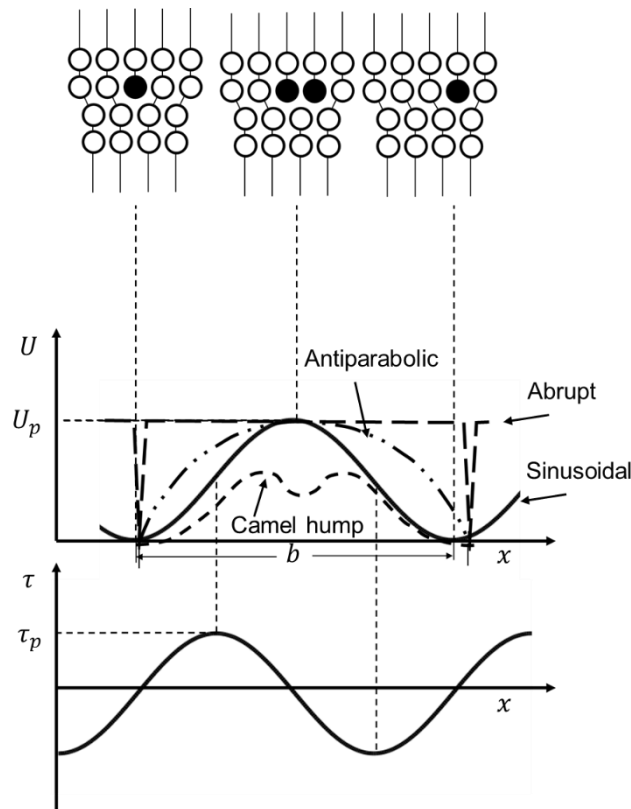
Fig. 2.12 Schematic illustration of the several Peierls potential shape varied with lattice and the Peierls stress illustration based on the sinusoidal potential, redrawn and revised [49, 85].

Hindered by the periodic potential, to move the dislocation from one valley to another, an energy barrier needs to be compensated. The applied maximum shear stress to pull this solid dislocation without any thermal activation assistance at $0\ K$ is called the well-known Peierls' stress τ_p (see Fig. 2.12). Here, a perfect pure crystal other than this single dislocation is assumed. Although different Peierls' potential functions were brought forward, they estimate a similar Peierls' stress. This stress value is normally much higher for bcc structures than for fcc due to the complex non-planar core structure in the former. Comparing mechanically tested Fe and Al, τ_p of high purity iron is 390 MPa [86] and of aluminum is even smaller than 10 MPa [87-89]. Note that a big stress discrepancy in magnitude of τ_p exists when applying atomistic simulations. In this way, Peierls stress τ_p of iron can reach 1000 MPa, which is explained by the stress concentration inside the deforming crystal [90]. As a result of high Peierls stress, among all those motion obstacles such as intersections of forest dislocations, Peierls process is most possible to be the controlling factor in bcc metals' plasticity under low to medium temperature ranges.
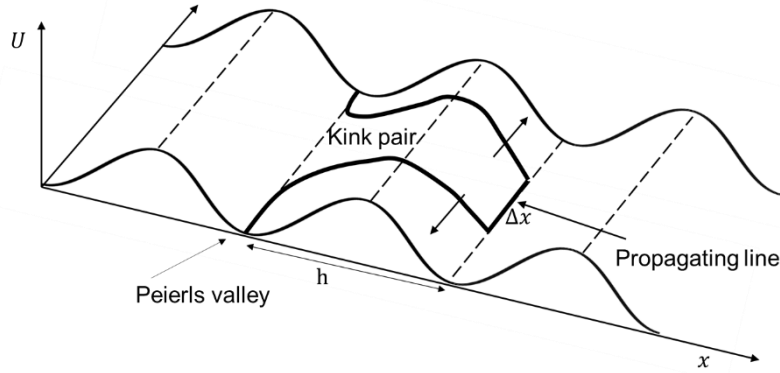
Fig. 2.13 Schematic representation of the thermally activated glide process of a dislocation overcoming the Peierls potential through a kink pair mechanism, redrawn based on [91].

However, at finite temperatures, the dominant screw dislocations in bcc metals in most cases do not move forward as a rigid whole restricted by their complex core structure. With thermal activation assistance, they move from one low energy position to another by the double kink (DK) mechanism under a smaller stress than τ_p [71, 85, 92]. Here, a part of dislocation line perturbs out and extends to the next valley, forming two kinks as shown in Fig. 2.13. The kink separation (width) is denoted by Δx and the kink height denoted by h. Dislocation motion by the DK mechanism consists of two stages, namely, kink nucleation and kink migration. The kinks are so mobile that the kink nucleation is generally regarded as the velocity controlling factor. This new configuration of a kink nucleus introduces energy change in this system, added by extra two kinks and subtracted by the work $\tau b \Delta x h$ of external force. τb is the force per unit dislocation length, multiplied by kink separation Δx (length) to obtain the total force, further multiplied by kink height h (moved distance) to finally evaluate the done work. A critical kink width x_c, hence, exists, above which a successful nucleation occurs. The corresponding energy peak is called the activation energy of kink nucleation $U_{KP}^{(c)}(\tau)$, is strongly dependent on the applied stress through work done. Researchers devoted themselves a lot to linking kink nucleation mechanisms with bcc structures peculiar behaviors. The line energy model raised by Dorn and Rajnak gains a good fit with experiments and according to that, the nucleation rate of kink-pairs per unit dislocation length can be described by Eq. (2.3) [92],

$$P_{KP} = \nu_D \frac{b}{x_c^2} exp\left(-\frac{U_{KP}^{(c)}(\tau)}{kT} \right)$$

(2.3)

Where ν_D is the Debye frequency and b the Burgers vector. Further, the dislocation velocity, under the assumption of high mobility of kinks, can be approximated as Eq. (2.4),

$$v = \nu_D \frac{bL}{x_c^2} h exp\left(-\frac{U_{KP}^{(c)}(\tau)}{kT}\right)$$
(2.4)

Here, L denotes the length of screw dislocation. This equation additionally suggests that the forward velocity of screw dislocations should be linearly proportional to its length, which is verified by *in situ* TEM observations [67].

In order to identify the Peierls process, the most reliable approach is the effective activation volume v^* defined as Eq. (2.5) [93],

$$v^* = -\frac{dU_{KP}^{(c)}(\tau)}{d\tau^*}$$
(2.5)

However, this is not intuitively simple to be correlated with macroscopic deformation experimental data. Hence, we need to link this definition with the Orowan's equation regarding the strain rate $\dot{\gamma}$ expression and combine it with the velocity derived from kink nucleation mechanism arriving at Eq. (2.6),

$$\dot{\gamma} = \rho_m b v = \rho_m \nu_D \frac{b^2 Lh}{x_c^2} exp\left(-\frac{U_{kp}^{(c)}(\tau)}{kT}\right)$$
(2.6)

Here, ρ_m is the mobile dislocation density. The pre-exponential term $\rho_m \nu_D \frac{b^2 Lh}{x_c^2}$ is considered as unvaried when changing the strain rate, which requires an instant change of strain rate to maintain a nearly identical initial state. Therefore, in the strain rate jump tests of one specimen, an experimental machine with high stiffness is in demand. Accordingly, by rearranging Eq. (2.6) and Eq. (2.5), the activation volume can be evaluated experimentally through Eq. (2.7),

$$v^* = -\frac{dU_{kp}^{(c)}(\tau)}{d\tau^*} \cong v_a = kT \frac{\partial ln\dot{\gamma}}{\partial \tau^*}$$
(2.7)

Note that the experimentally obtained activation volume is only apparent due to two reasons: first, we ignore the microstructural change such as dislocation density in the pre-exponential term and this might not be always true. Second, the shear stress τ we usually adopt to calculate the activation volume is composed of thermal τ^* and athermal τ_a part, which is difficult to separate each other strictly, as shown Fig. 2.14. A critical temperature T_c exists above which, Peierls' barrier can be overcome solely by thermal activation and plays a minor role in the deformation behavior of crystals, while below this temperature extra stress τ^* has to be

provided. The (apparent) activation volume range for the Peierls process is 10^1-10^2 b^3 while for the dislocation intersection it is of the order of 10^2-10^4 b^3 [93].
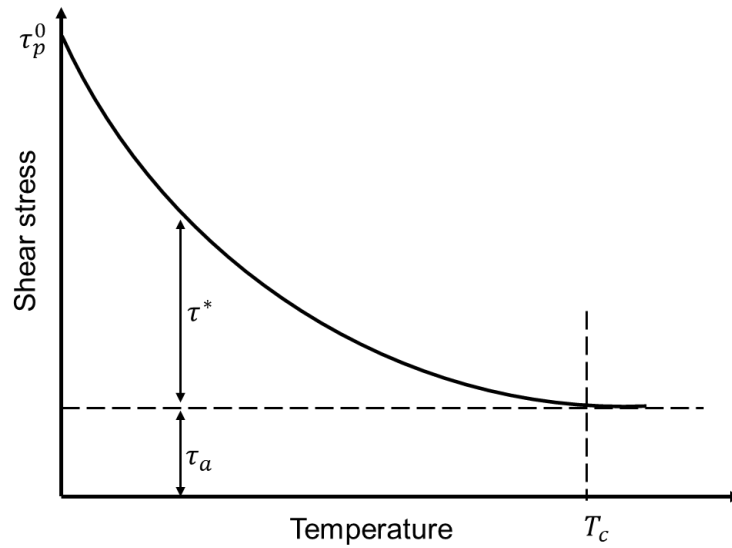

Fig. 2.14 Schematic description of the stress-temperature relationship in bcc metals, redrawn and revised based on [94]. τ^* is the thermal component of shear stress while τ_a the athermal part. T_c is the critical temperature, above which shear stress shows negligible dependence on temperature.

2.3 Fracture mechanics

2.3.1 Linear elastic fracture mechanics (LEFM)

Fracture mechanics has a history of approximately 100 years. Griffith is one of the most contributing predecessors in this field, who brought forward the energy concept to analyze the fracture propagation with a preexisting crack in the 1920s [95]. A crack can grow only if the propagation process causes the total energy to decrease or remain constant. According to that, if a through-thickness crack in an infinitely wide plate is subjected to a remote tensile stress, the required fracture stress σ_f should fulfill the following equation,

$$\sigma_f = \left(\frac{2E\gamma_s}{\pi a}\right)^{1/2}$$

(2.8)

Where E is Young's modulus, γ_s the surface energy of a material, the energy needed to break atomic bonding per unit area, and a is the half crack length.

However, Griffith's theory can be only applied to ideally brittle materials until Irwin [96] and Orowan [97] extended Griffith's theory to metals by considering the energy dissipation by local

plastic deformation. So the revised version simply adds the plastic energy term γ_ρ as in Eq. (2.9),

$$\sigma_f = \left(\frac{2E(\gamma_s + \gamma_\rho)}{\pi a}\right)^{1/2} \tag{2.9}$$

Later, Irwin [98] put forward the concept of energy release rate G. Note that the term *rate* is not related with time, but represents the change rate of potential energy with respect to the crack area. It is also called the crack driving force. The driving force G remains identical for both load and displacement control, but the derivative of G with respect to crack length a is distinguished, which indicates that the crack growth is more stable under displacement control loading mode. This is also the common loading mode in experimental tests in order to obtain a crack resistance curve.

Besides understanding fracture process from the energy view point, we can also comprehend it through the stress distribution in front of a crack [99-101]. In a linear elastic, isotropic material, the near crack tip stress field can be describe as followed,

$$\sigma_{ij}(r,\theta) = \frac{K_{I,II,or\ III}}{\sqrt{2\pi r}} f_{ij}^{(I)}(\theta) \tag{2.10}$$

where σ_{ij} is the stress tensor, $K_{I,II\ orIII}$ is the stress intensity factor of loading *Mode I, II, III*, r the distance from the crack tip and $f_{ij}^{(I)}(\theta)$ the angular dependent dimensionless term [60]. Each mode produces the $\frac{1}{\sqrt{r}}$ singularity at the crack tip. Consider the *Mode I* singularity on the crack plane with $\theta = 0$, the normal stress σ_{yy} is $\frac{K_I}{\sqrt{2\pi r}}$ as Fig. 2.15 over distance from crack tip (dashed line). The solid line can be obtained by finite element modelling (FEM) simulation. By comparing the two curves, the singularity formula can correctly describe the normal stress field only at regions close to the crack tip. Outside this domain, the stresses are governed by the remote boundary conditions like the subjected remote tensile stress.
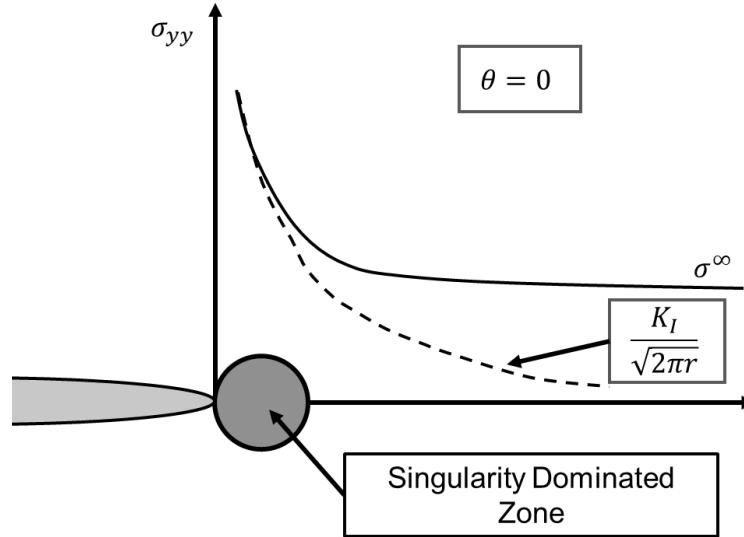
Fig. 2.15 Stress normal to the crack plane under fracture *mode I*, redrawn from [60].

The stress intensity factor K_I, defines the amplitude of the crack tip singularity. With a known K_I, it is possible to solve all stress components in front of a crack tip. It can be obtained from the remote loads and the geometry, generally expressed by Eq. (2.11),

$$K_I = \frac{P}{B\sqrt{W}} f\left(\frac{a}{W}\right)$$

(2.11)

Here P denotes the applied load, B is the sample width, W sample thickness and a the crack length. The last term $f\left(\frac{a}{W}\right)$ represents the dimensionless geometrical factor that depends on specific tested geometry. For several standard specimen types, it is directly tabulated in ASTM E399 while for non-standardized geometry, FEM can be applied to access it.

Fracture toughness of a material is an intrinsic property that describes the geometry independent fracture resistance under plane strain condition which is called K_{Ic},

$$K_{Ic} = K_I = Y\sigma\sqrt{\pi a}$$

(2.12)

Hereby, Y is a dimensionless constant depending on geometry and loading mode (I, II, III).

Whether we consider fracture mechanics problem from energy concept or from stress analysis, does not direct us differently, although the former describes global behavior and the latter is a local parameter. As a matter of fact, the energy release rate G_c and the stress intensity factor K_c can easily correlate with each other for a linear elastic isotropic material [100],

$$G_c = \frac{K_{Ic}^2}{E'}$$

(2.13)

Where E' depends on the stress state, either plane stress or plane strain.

2.3.2 Elastic plastic fracture mechanics

LEFM only applies to ideally brittle materials or materials with small scale yielding where the plastic zone is embedded in the K dominated zone. When yielding cannot be neglected, EPFM should be adopted. The *J integral* is a widely used concept that was put forward by Rice [102]. *J integral* can be regarded both as an energy parameter and as a stress intensity parameter. As an energy parameter, Rice [102] showed that J is a path independent line integral and equals the strain energy release rate. As the stress intensity parameter, Hutchinson, Rice and Rosengren [103, 104] found that J can characterize the crack conditions in a nonlinear elastic material. The stress field of the plastically deformed zone near the crack tip is expressed as followed,

$$\sigma_{ij}(r,\theta) = \sigma_0 \left(\frac{EJ}{\alpha \sigma_0^2 I_n r} \right)^{\frac{1}{1+n}} s_{ij}(n,\theta) \tag{2.14}$$

Here, σ_0 is the reference stress used in the power law description between plastic stress and strain that is usually equal to the yield strength. E, the Young's modulus, α, a dimensionless constant, I_n, a constant that depends on n, the hardening exponent and s_{ij} a dimensionless function of n and θ. This stress field expression $r^{\frac{-1}{n+1}}$ is named after Hutchinson, Rice and Rosengren called HRR-field. Note that the hardening exponent for linear elastic materials equals 1, which also consistently predicts a $\frac{1}{\sqrt{r}}$ singularity near crack tip.

2.3.3 Fracture toughness testing of metals

For linear elastic materials, the ASTM E399 standard is widely applied to obtain the critical fracture toughness K_{Ic} [105]. Four specimen configurations are permitted here, including the compact tension, single edge notched bending, arc-shaped and disk-shaped specimens. The load and displacement of the precracked specimen upon loading is recorded until failure and three types of curves occur frequently as shown in Fig. 2.16. Depending on the type of curves, the critical load P_Q for fracture toughness calculation is defined differently. A 5% secant line method is proposed, where a secant line is constructed from the origin with a slope equal to that of the initial elastic loading [60, 105]. With a Type I curve, P_Q equals P_5, the intercept of the secant line with loading curve. For a Type II curve, P_Q is defined at the pop-in point, while $P_Q = P_{max}$ when the specimen fractures completely before reaching a 5% nonlinearity.
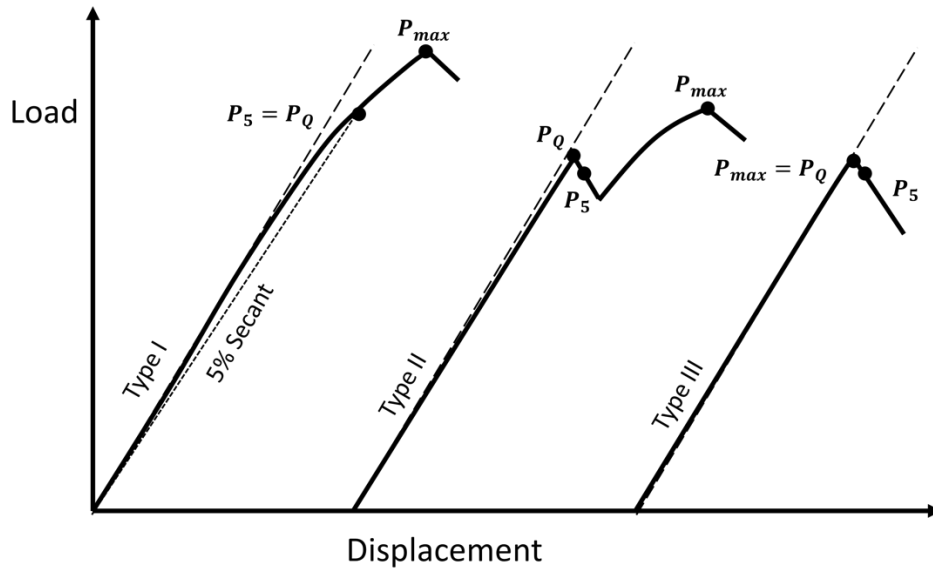
Fig. 2.16 Three types of load-displacement behavior in a K_{Ic} test, redrawn based on [105].

After determination of the critical load, one can compute a provisional fracture toughness according to Eq. (2.11), which can be considered as the valid K_{Ic} only if the following stringent requirements are fulfilled,

$$0.45 \leq a/W \leq 0.55 \tag{2.15a}$$

$$B, a \geq 2.5 \left(\frac{K_Q}{\sigma_{YS}}\right)^2 \tag{2.15a}$$

$$P_{max} \leq 1.10 P_Q \tag{2.15a}$$

However, metals, ensuring the safe application, in most cases do not show a linear elastic fracture behavior. So experimentally, the J integral represented fracture toughness J_{Ic} is measured according to standard ASTM E1820 that has two alternative methods: the basic procedure and the loading-unloading sequence procedure [106].

In the basic procedure, the crack growth is not monitored during testing. Rather several identical samples are prepared and loaded to different levels then unloaded. In this case, different crack

growth states can be reached, each of which generates a J value forming finally a $J - R$ curve. For calculation, J is divided into elastic and plastic parts:

$$J = J_{el} + J_{pl} \qquad (2.16)$$

The elastic part is obtained from the elastic stress intensity K according to Eq. (2.11):

$$J_{el} = \frac{K^2(1 - \nu^2)}{E} \qquad (2.17)$$

The plastic part is computed as followed:

$$J_{pl} = \frac{\eta A_{pl}}{B b_0} \qquad (2.18)$$

Here, η is a dimensionless constant and A_{pl} the plastic area under the load-displacement curves schematically shown in

Fig. 2.17, b_0 the initial ligament length and B the sample width. Note that the ligament length is not updated with crack growth, since it has a negligible influence on the aimed crack initiation fracture toughness J_{Ic}.
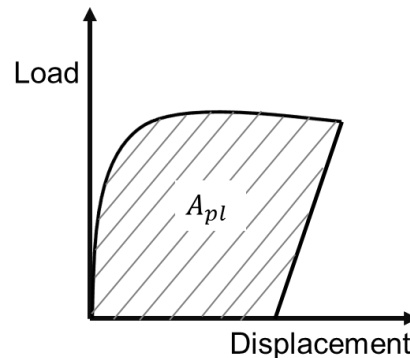
Fig. 2.17 Schematic loading curve showing the plastic energy absorbed by test specimen during a J_{Ic} test.

The definition of J_{Ic} is shown in **Error! Reference source not found.**, including ideally all hree stages of crack growth, namely, stationary crack blunting, transition stage and steady state crack growth. Note that during the steady state, the stress/strain state around the crack reach a constant state, which is not usually observed in experimental labs, since very large specimens are required for tough materials. J_{Ic} is the toughness at the transition point from crack blunting to crack initiation, which is less geometry dependent and can be used for comparison between different materials. However, similar to the yield strength, the initiation toughness is in most cases not unambiguously identified. Hence, in the ASTM E1820, there are certain regulations. Only data points within defined ranges can be used for curve fitting, lying below J_{max} and

between exclusion lines of Δa_{min} (0.15 mm) and Δa_{max} (1.5 mm), as outlined by the red dash lines in Fig. 2.18. The maximum J value is defined by Eq. (2.19),

$$J_{max} = \frac{b_0 \sigma_Y}{15} \qquad (2.19)$$

The valid data points are then fitted with a power-law expression:

$$J = C_1 (\Delta a)^{C_2} \qquad (2.20)$$

The J_Q is determined as the intersection between the power-law expressed curve and the 0.2 mm offset line with a slope equal to $M\sigma_Y$ as shown by the solid red line. M can take a default value of 2 and σ_Y is the flow stress as the average of the yield and tensile strengths. J_Q can be regarded as J_{Ic} additionally requiring that the following size conditions are fulfilled:

$$B, b_0 \geq \frac{25 J_Q}{\sigma_Y} \qquad (2.21)$$
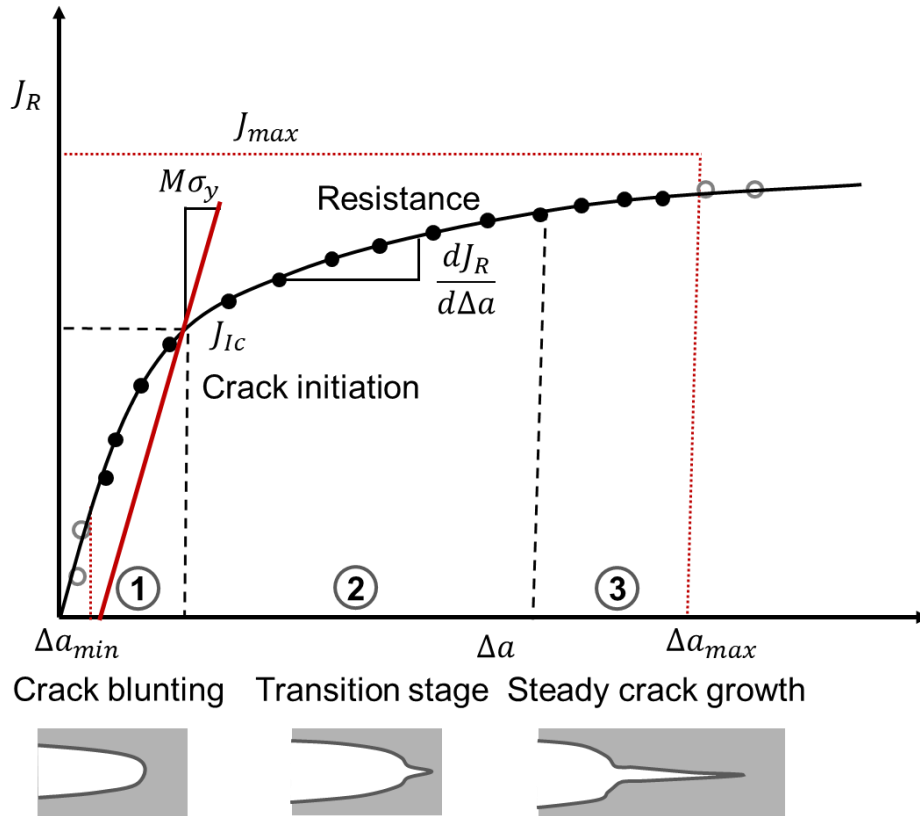
Fig. 2.18 A schematic $J - R$ curve showing three stages of crack growth and the data points regulated in E1820 for valid J_{Ic} evaluation, recombined based on [60, 106].

Compared with the basic procedure that requires multiple identical specimens, the loading-unloading sequence method is possible to work out the $J - R$ curve based on a single specimen. Here, the crack growth needs to be monitored by partial unloading during the testing. One common way is to measure the compliance upon each unloading sequence as illustrated in Fig.

2.19. The cross section of the specimen decreases with crack growth and the compliance of the specimen increases so that they can be correlated by:

$$a_i = W - \sqrt[3]{\frac{4k_i L^3}{BE}}$$

(2.22)

The a_i and k_i corresponds to the respective crack length and specimen stiffness of the i_{th} unloading sequence. The additional protocol is similar with that in the basic procedure for a $J - R$ curve.
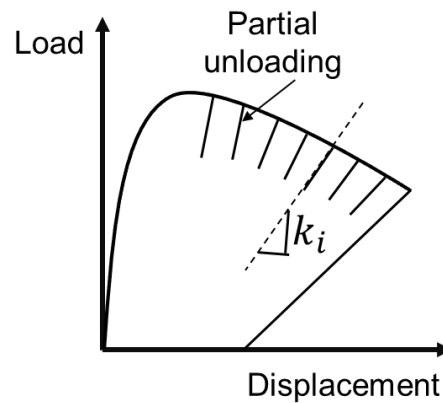

Fig. 2.19 Schematically showing compliance method to record the crack growth, redrawn based on [106].

2.3.4   Fracture mechanics at microscales

The common standard fracture tests were established for macroscopic samples in the order of mm or even of cm. However, the development of small sized microelectromechanical systems (MEMS) and thin films accelerates the necessity of extending fracture mechanics to micro or sub-micro regime, since they also contain flaws that cause functionality failure [107, 108]. The microscale fracture testing also provides insights of the interplay between plastic deformation and microstructure components, assisting in an understanding the fracture mechanisms[109-111].

With assistance of FIB milling, the currently applied microscale fracture tests include pillar splitting, single cantilever bending, double cantilever bending and clamped beam bending [14, 112-115], among which single cantilever bending is most popular. It provides possibility both for brittle and semi-brittle materials like metals [14, 30, 116].

One main challenge of fracture tests on micro- or submicro-sized samples is that size requirements defined in ASTM are dissatisfied. Well-known is the fracture toughness increases with decrease in sample thickness, changing from plane strain to plane stress state. In plane strain, the stress triaxiality in front of a crack suppresses plastic deformation, leading to a small plastic zone size and less plastic energy dissipation, which is in contrary with that in plane stress state. Generally, the plastic zone size r_{pl} is an important parameter to evaluate if the acquired fracture toughness is material characteristic value or not, and can be estimated as:

$$r_{pl} = c_1 \frac{K^2}{\sigma_y{}^2} \qquad (2.23)$$

r_{pl} strongly depends on fracture toughness, yield strength as well as the factor c_1 which is influenced by the loading geometry and stress state [60, 117]. For small scale yielding, where the plastic zone is embedded in the K-dominated zone ($r_{pl} < r_K$) as illustrated in Fig. 2.20, both J integral and K can be applied to describe the stress distribution of the crack front following Eq.(2.10). Some brittle materials were microscopically tested and found to have comparable fracture toughness with macroscopic samples [113]. If the plastic zone is further increased, K dominated zone can disappear and only J integral is valid. Although the sample size requirements for J integral are not as stringent as K (See Eq. (2.21) and Eq. (2.15)), it remains a challenging issue when micro- or submicro-sized samples are tested, where even the J dominated zone might disappear. The obtained J in micromechanical experiments cannot reflect the geometry independent property. Besides, the concept of K and J integral are based on the continuum mechanics, assuming a homogeneous, monolithic body without considering physically important microstructural heterogeneity such as different phases and grain boundaries. Only if the characteristic microstructure size is much smaller than tested sample dimensions like crack length, width and thickness, a geometry independent fracture toughness can be acquired [117].
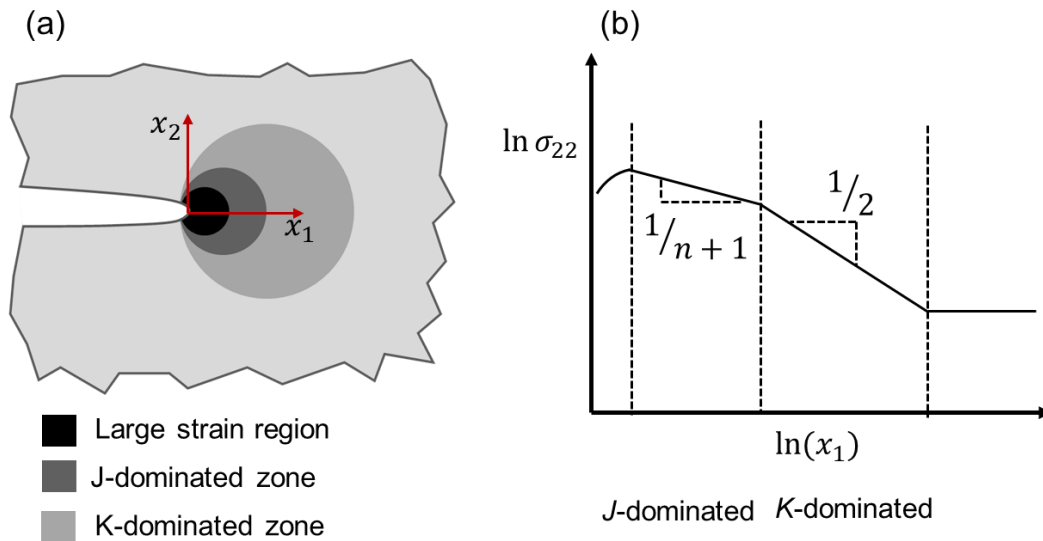
45

Fig. 2.20 (a) Illustrative representation of the different characteristic zones under small scale yielding and (b) the stress strain distribution in front of the crack. Redrawn and revised according to [60, 117].

Another issue for microscale fracture tests is introduced during the sample fabrication by FIB. The applied source ions, mainly Ga^+ can introduce such defects as segregation, clusters, amorphization and lattice distortions which are not intrinsic to materials [118, 119]. By applying different ion sources for notching the microcantilever beams, an inconsistent fracture toughness value is obtained for CrN, which is mainly attributed to the interaction of incident ions and probed materials [120]. However, a different notch radius is also found in this case, which acts as also one important factor. Moreover, the prenotch as the initial crack is challenging to arrive at an ideal situation as schematically depicted in Fig. 2.21a. The red dashed lines outline the crack plane for a microcantilever. By contrast, the prenotched crack by FIB milling frequently finishes as Fig. 2.21b and Fig. 2.21c, corresponding a bridging and over-fibbing case, respectively. The geometry of crack shape is shown by Abaqus FEM to have nonnegligible influence on the obtained fracture toughness value. An overestimation of fracture toughness occurs when the crack is not through and with bridge material at two ends, while an underestimation is possible when the crack is rounded by over-fibbing [121]. Therefore, a final careful fine milling to remove the rounded part in the over-fibbing case is proposed to arrive a straight through crack [31].

46
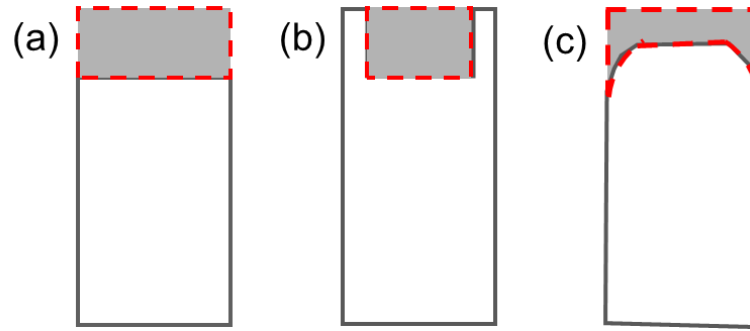
Fig. 2.21 Three different schematic crack planes: (a) straight through crack, (b) bridged crack and (c) over-fibbed crack, redrawn based on [121].

3   Experimental procedure

3.1   Material preparation (chemical, metallography)

In this work, two types of industrial DP800 steels (DP1 and DP2) were investigated. The chemical composition analyzed by wet chemical analysis is shown in Table 3-1. They have an identical carbon content and the main difference lies in the Cr content. Both steel grades were provided in a sheet form with a thickness of 1.5 mm. DP2 was additionally zinc-coated and if not specifically mentioned, the presented results are from this steel grade.

Table 3-1 Chemical composition in weight percent (%) as determined by wet chemical analysis for both DP800 steel grades denoted by DP1 and DP2.

	C	Si	Mn	P	S	Al
DP1	0.131	0.206	1.51	0.008	0.0023	0.03
DP2	0.131	0.194	1.69	0.0088	0.0016	0.038
	Cr	Mo	Nb	Ti	V	B
DP1	0.0187	<0.005	0.0188	0.0014	0.0084	<0.001
DP2	0.718	0.0035	<0.001	0.0303	0.0027	<0.001

Before producing any micro specimens using focused ion beam (FIB) or conducting microstructural investigation, basic metallographic preparation was performed. The massive steel sheets were first mechanically cut into pieces of $8\times5\times1.5$ mm^3. For the FIB fabrication, the cross section 5×1.5 mm^2 of specimen pieces was grinded up to 4000$^\#$ and polished using oxide polishing suspension (OPS) with particle size 30 nm. Such a surface preparation was also guaranteed for EBSD measurements, which was used for measuring orientations of ferrite pillars and martensite substructures. Besides, based on the confidence index (CI) of ferrite and martensite, the grain size distribution of two phases was determined. For the observation of

phase components via SEM, specifically Zeiss Gemini500 field emission microscope, an additional etching step of 5 s was performed using 1% Nital (a mixture of nitric acid and ethanol) on the OPS polished surface. Point counting was applied on the images of etched samples to obtain the phase volume fraction. For ECCI observations, due to the extremely high demand on the surface quality, the samples were embedded, grinded and finally vibropolished with Mastermet 2. For the fabrication of micro cantilevers, the cross section 8×5 mm^2 was also grinded up to $4000^{\#}$ since the micro beams of martensite were to mill at the very edge of specimen pieces aimed for a reduced milling time. A clean sample edge with small roughness was, hence, required.

3.2 FIB specimen fabrication

FIB technique is indispensable in our microscale study, which was applied to produce annular pillars for plasticity investigation of both ferrite and martensite, to generate micro cantilevers for fracture toughness of martensite islands and to obtain needle-like sharp tips for chemical analysis at an atomic scale.

The annular micropillars were in an aspect ratio (height/diameter) of 2 to 4. The diameter of ferrite pillars has three types, 1 µm, 2 µm and 3 µm sized, while of martensite only one type of 800 nm limited by its small colony size. The pillar specimens were mainly milled on a Zeiss Auriga® dual beam FIB. A three-step milling strategy using 30 keV Ga$^+$ ions was adopted for their production: rough milling of the outermost ring with 16 nA ion current, a middle ring with 2 nA and final fine shape with 240 pA. In the section of investigating the strain rate influence on the slip system activation, those pillars were produced on an FEI Helios NanoLab 600TM using also 30 keV Ga$^+$ ions. The coarse milling was performed under an ion current of 9.3 nA and the final fine milling with 80 pA. By crosschecking data from pillars milled on two FIB systems, no significant difference was observed in our case.

The micro cantilevers were produced by Zeiss Auriga® dual beam FIB. Our targeted feature is the relatively large martensite islands, which can be first identified from the top view, according to the slight topographical contrast induced by OPS polishing. Following that, a small cut using fine current 120 pA was carefully made at the boundary of a presumably large martensite island to determine as much as possible the three dimensional size of the island. Only martensite islands extending more than 1 µm in depth were considered for further milling into micro

cantilever shapes as illustrated in Fig. 3.1a. The ion current for coarse milling, intermediate and fine milling were 16 nA, 2 nA and 240 pA, respectively. In the end, a through thickness notch was milled using a current of 15 pA. This specific geometry compared with the standard single cantilever beam was motivated by two aspects: one is the very limited martensite islands' size and the other is to prevent plastic deformation in the significantly softer ferrite. This is required to link the force-displacement curve directly to processes during crack initiation and growth at the harder martensite without being obstructed by ferrite plasticity. The neck area ensures, to the largest extent, a full martensite microstructure in the highly stressed gauge section, while the ferrite suffers considerable low stresses due to the increased sample thickness. In Fig. 3.1, *M* denotes martensite while F ferrite. L is the length of the beam, from the notch to the loading point. *W* is the thickness, a_0 the initial crack length (red mark) and B the cantilever width. The aspect ratios are kept constant at $W : B : a_0 : L = 1 : 1 : 0.2 : 5$ with a nominal cantilever width of $B = 1$ µm.
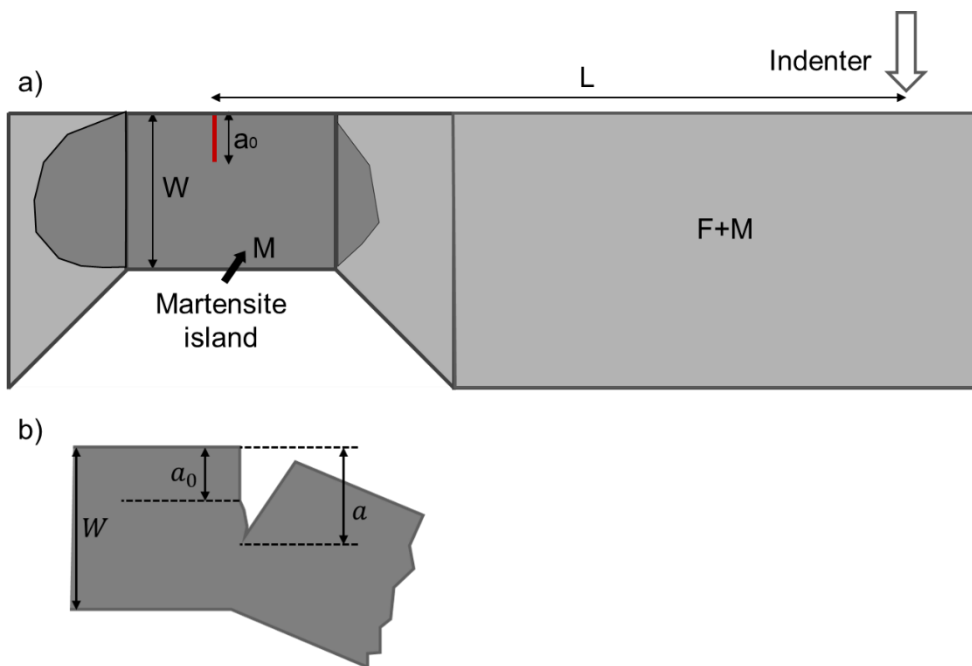
Fig. 3.1 (a) Schematic of the cantilever geometry used in the bending testing; (b) Definition and measurement of crack length.

The needle-like sharp tips for APT analysis were fabricated on the FEI Helios NanoLab 600TM. Wedge shaped lamellas with the targeted feature was FIB milled free and lifted out by a manipulator. These lamellas were approximately 15 µm long and 2 µm wide. After cutting into 3-5 small pieces of 2×2 µm^2 from top view, they were consecutively stacked on the numbered silicon coupon for further sharpening. Constantly, each piece was reshaped with circles by

30 keV Ga^+ ions. The ion current 0.23 nA was applied for coarse milling to roughly 700 nm in diameter, followed by 80 pA to 300 nm and 24 pA to 100 nm. In the end, the sharp tip was cleaned using 5 keV Ga^+ ions under a current of 15 pA.

3.3 Pillar compression tests

Since the ferrite pillars were extracted randomly from polycrystalline bulk, before performing pillar compression tests, EBSD was carried out on top of each pillar in order to determine the orientation and further to calculate CRSS of ferrite and analyse its activated slip systems. We conducted EBSD measurements using the same Zeiss Auriga® microscope equipped with an EDAX system with Hikari® charged coupled device (CCD) and the orientation information was compiled through the TSL OIM 7 software package. By contrast, no EBSD was performed on martensite pillars as the small martensite colony contains differently oriented variants. We simply aimed for a compressive yield strength of martensite pillars.

All the *in situ* micropillar compression tests were performed in the Zeiss Gemini500 equipped with an ASMEC Unat II device (Asmec GmbH, Radeberg, Germany) in displacement mode and constantly flat diamond tips provided by Synthon MDP (Switzerland) were applied. A loading rate of approximately 1×10^{-3} s^{-1} was set for all the tests except for those aimed at investigating the influence of strain rates, where 1×10^{-1} s^{-1}, 1×10^{-2} s^{-1} and 1×10^{-4} s^{-1} were additionally applied. For the calculation of the engineering stress versus engineering strain curves, the force was divided by the area of the pillar top and the displacement divided by the initial pillar height. The initial pillar size was measured before testing.

After the *in situ* tests, the compressed pillars were first imaged for slip pattern identification under the Zeiss Gemini500 and Zeiss Auriga®. Besides, in respect to ferrite, by taking advantage of the previous EBSD orientation, a virtual pillar superimposed with all 48 slip system candidates can be drawn by Mathematica scripts. By comparing the slip patterns directly obtained from microscopes and those from the mathematica programming, the activated slip system can be identified. Consecutively, the CRSS can be calculated by taking the engineering normal stress σ at the onset of yield and the Schmid factor m of the activated slip system into account and applying $\tau = \sigma \cdot m$.

3.4 Cantilever bending test

The *in situ* micro cantilever bending tests were performed as well in the Zeiss Gemini500. In this case, a Hysitron indenter system with a wedge shape tungsten carbide was used. The tests

were conducted also in a displacement controlled mode, with a displacement rate of 5nm/s. Loading and unloading segments were applied for the convenience of measuring crack growth through SEM snapshots, for which the stage tilt angle was always corrected. The snapshots during unloading segments were used to measure the crack length a according to the definition provided schematically in Fig. 3.1b.

During the data processing, EPFM was applied to analyse the fracture toughness of martensite islands, where both the elastic and plastic contributions were taken into account as listed in Eq.(2.11) and Eq.(2.16) - (2.18). The geometry factor $f\left(\frac{a}{w}\right)$ specific for our shape is expressed as in Eq.(3.1),

$$f\left(\frac{a}{W}\right) = 1.46 + 24.36\left(\frac{a}{W}\right) - 47.21\left(\frac{a}{W}\right)^2 + 75.18(\frac{a}{W})^3 \tag{3.1}$$

This equation is based on a cantilever geometry as proposed by Matoy [122]. However, by comparing with that fitted for our specific shape modelled in the Abaqus, they match each other quite well. Details are presented in the Appendix I.

3.5 ECCI investigations

ECCI currently evolves as a powerful tool to characterize such crystal defects as stacking faults, dislocations and nanotwins [123-125]. Compared with TEM that requires extremely thin samples, a bulk specimen after metallographic preparation can be directly investigated using the ECCI technique.

ECCI observations were conducted on a Zeiss Merlin^{TM} electron microscope that is equipped with a BSD detector (backscatter electron detector). The following settings were used: accelerating voltage 30 kV, working distance (WD) 7.7 mm and the stage tilt angle 0°. In contrast to the EBSD technique, a much smaller WD is required for ECCI to increase the amount of backscatter electrons collected by the detector, usually between 5-7 mm [123]. We did not tilt the stage for an intended ferrite grain or martensite island since the primary goal was rather a qualitative visualization of the dislocation distribution across the ferrite grain interior to the phase boundary. Therefore, we simply randomly located a target showing electron channeling contrast in the zero tilt condition. Otherwise, one can take advantage of the software TOCA (tools for orientation determination and crystallographic analysis) to guide the tilt and rotation angles, arriving at a two-beam condition so that the dislocation density on a specific

crystal plane can be determined and also the Burgers vector combined with the inclination angle of dislocation lines with respect to the surface [125].

3.6 EBSD

EBSD technique was applied for determination of ferrite pillar orientation and also observation of substructures in martensite islands. All measurements were performed on a Zeiss Auriga® microscope equipped with an EDAX system with Hikari® charged coupled device (CCD) and the TSL OIM 7 software package.

For determining orientation on top of ferrite pillars, the scan rotation was to turn off and the stage rotation was so fixed that that the horizontal line of a previously FIB-milled reference cross is parallel to the image frame. These two settings ensure the comparability of SEM post mortem images of pillars and those drawn in Mathematica, identifying activated slip traces. Further, to minimize the influence of the possible FIB induced redeposition on top of pillars on Kikuchi patterns and increase the diffraction intensity, a high voltage 15kV or 20kV was used together with high current on and a large aperture of 120 μm. The WD is always 16 mm and the step size is set as 0.01 μm. These settings are kept the same when investigating the substructures of martensite islands. The step size is set as small as 0.01 μm to acquire more details of small features. The index phase for martensite is constantly loaded as ferrite. As martensite is saturated with carbon and contains large number of defects, the confidence index is lower compared with ferrite, which is a standard to differentiate the two phases.

3.7 APT measurement

APT is becoming an important technique for material scientists to characterize especially the chemical information of matter at an atomic resolution. It can reveal atomic architecture in solid solutions, the interface chemistry and precipitates composition.

We conducted all APT measurements on a CAMECA local electrode atom probe LEAP^{TM} 5000 XR (reflection fitted with a flight path 382 mm) using the voltage mode. The choice of voltage pulse mode instead of laser mode is attributed to the good conductivity of steel and the low tip fracture tendency under a high electric field. Besides, although the laser mode can largely solve the conductivity limitation, which evaporates ions by instant thermal rise, it usually results in a worse spatial resolution [126-128].

Two parameters, the pulse fraction and base temperature, are of great importance to ensure a good reconstruction of 3D tomography and a high spatial resolution. The pulse fraction is defined as the ratio between the amplitude of the high voltage pulse and the direct current (DC) voltage. This additional voltage pulse was imposed on the sharp needle shape tip to overcome the potential energy barrier and ionize the tip atom by atom. In the course of measurement, the tip radius becomes larger so that the pulse voltage needs to increase its amplitude as well with DC voltage to keep a constant pulse fraction. According to [129, 130], we set the pulse fraction as 20% and the base temperature was set as low as 60 K, minimizing the surface diffusion and increasing the lateral resolution. Additionally, the pulse repetition rate was set to 250 kHz. Generally, a high pulse rate can guarantee a high data collection rate. However, for heavy molecular ions, a lower value is preferred since they require more time of flight [128]. All measurements were carried out under an ultrahigh vacuum environment in the order of 10^{-11} Torr that helps reduce the background noise.

4   On the mechanical heterogeneity in dual phase steel grades: activation of slip systems and deformation of martensite in DP800[1]

4.1   Introduction

DP steels – comprised of a soft ferrite matrix and dispersed hard martensite islands – are widely used as structural material, e.g. for automotive applications because they offer a good combination of high strength and ductility. Furthermore, strength and ductility can be controlled by several metallurgical and thermomechanical factors including the carbon content, additional alloying elements, or heat treatments to tune the martensite volume fraction, the grain size of ferrite and martensite as well as the texture [10, 131-134]. Because of their special composite structure, DP steels behave heterogeneously during deformation at the microstructural length scale. Also, the heterogeneity complicates the understanding of the deformation behavior, particularly during damage initiation and growth, which has been intensively investigated both by experiments and modelling work. Experimentally, the heterogeneity is characterized either through analyzing the strain localization and the evolution of damage [135-137] by digital image correlation (DIC) *in situ* or by EBSD based kernel average misorientation (KAM) [138].

In case of modelling a representative volume element (RVE) based on the real microstructure is used to analyze stress and strain partitioning upon loading [139, 140].

While the important role of heterogeneity on the mechanical behavior of DP800 is evident, an explicitly quantitative and mechanism based description of the mechanical properties of ferrite and martensite and their impact on damage initiation and growth had rarely been studied. Kumar's research group [141-143] significantly contributed to this field by measuring the compressive yield strength of individual phases via pillar compression. Also, they calibrated a CP-FEM using their experimental stress-strain curves of ferrite pillars [141, 143, 144]. However, a comprehensive study on the activation of different slip systems and a thorough analysis of the CRSS of single crystalline ferrite is still lacking. This data can then serve as input parameter in CP-FEM, for which constitutive models of deformation at the single grain level are vital. The most prominent parameter of these models is the CRSS of all contributing slip systems. Despite the controversy on activated slip systems in bcc iron it became common practice to assume $\{110\}\langle111\rangle$ and $\{112\}\langle111\rangle$ slip systems only [145-147]. This practice partially ignores the experimental observations of slip on the other closed packed planes, like $\{123\}$. Due to the lower velocity compared to edge dislocation, screw dislocation motion is controlling the plastic deformation of bcc [25]. The core structure of screw dislocation in bcc is non-planar, which is commonly regarded as the key reason for the breakdown of Schmid´s law in bcc materials [24]. Gröger et al. [21] proposed that not only the resolved shear stress on the slip plane in the slip direction but also the entire stress state play an important role for CRSS. All these factors result in a complex, time, temperature and orientation dependent dislocation slip behavior, which requires constitutive material laws for simulating bcc materials by CP-FEM.

Micropillar compression [143] is the ideal tool to study microstructure heterogeneity at the micron level as it can be used to isolate individual phases, grains or interfaces and estimate the local CRSS by analyzing the activated slip system [148-150]. Within this study we are applying micropillar compression to measure the mechanical properties of bcc ferrite and martensite of two different DP800 steel grades with an identical macroscopic ultimate tensile strength (UTS) but different elongation to failure. We show that – in both cases – three different slip system families behave identically in terms of CRSS and that – in our case – the Schmid factor is the dominant cause for slip system activation. The results are also used to explore pathways for reducing the damage occurring during metal forming.

4.2 Results

4.2.1 Characterization and tensile result

We have performed microstructure characterization and analyzed the element distribution of two commercial DP steels. The microstructure of both DP steel grades exhibit a banded morphology of martensite and partly dispersed martensite islands in the ferrite matrix (see labelled banded martensite with double ended arrow in Fig. 4.1a and b). The martensite volume fraction of DP1 and DP2 was evaluated by point counting in 10 regions, which is comparable for both steel grades $42 \pm 1\%$ and $38 \pm 1\%$[2]. However, the grain size distribution shows larger martensite colonies and smaller ferrite grains in DP1 compared to DP2 (Fig. 4.1c). The average colony size of martensite is $1.1 \pm 0.1\,\mu m$ and $1.0 \pm 0.1\,\mu m$, while of ferrite grains it is $5.9 \pm 0.1\,\mu m$ and $7.0 \pm 0.1\,\mu m$, correspondingly.

---

[2] Unless otherwise stated the error bars are always provided as the error of the mean.
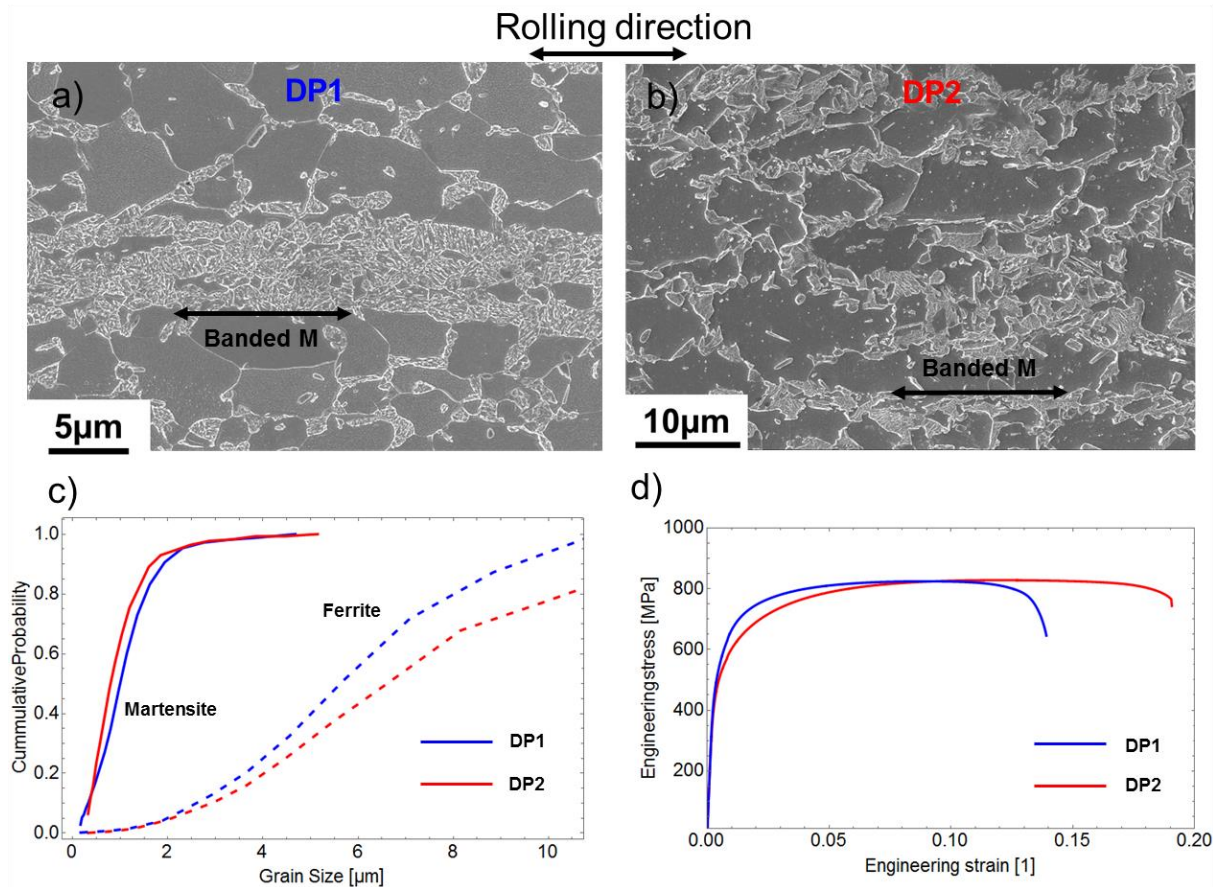
Fig. 4.1 Secondary electron image of (a) DP1 and (b) DP2 steels. (c) Grain size distribution of ferrite and colony size of martensite for both steel grades. (d) the macroscopic tensile test results for both steel grades.

The engineering stress versus strain curves obtained by the macroscopic tensile testing (Fig. 4.1d, according to DIN EN ISO 6892-1) shows two distinct differences of the two steel grades in rolling direction: (i) DP1 yields at 530 MPa which is 36 MPa higher compared to DP2 (494 MPa). (ii) Also, DP1 fractures at an elongation of 14.4% which is lower compared to DP2 with a strain to failure of 18.6%. Similarly, the uniform elongation of DP1 is also smaller (compare 8.8% to 11.5%). Nevertheless, both steel grades reach an identical ultimate tensile strength of 830 MPa.

The martensite colonies have a complex substructures as shown in Fig. 4.2a and b. They exhibit a hierarchical structure with lath morphology. The laths reveal a well-known orientation relationship to the parent austenite, namely, $\{111\}_\gamma \,//\, \{110\}_\alpha$ and $\langle 110\rangle_\gamma \,//\, \langle 111\rangle_\alpha$ being consistent with literature (e.g. [45]). The packets are highlighted in Fig. 4.2a and b by white lines and the variants are labeled by numbers. Within our islands we do not simultaneously see all 24 variants expected for one PAG. Even in one packet, the variants are not complete as we

56

observe less than 6 variants (see for instance the packet 1 in Fig. 4.2a). The block width of martensite in both DP grades is similar and of the order of 100nm (see black arrow Fig. 4.2a and b). We identify this unit as block through the pole figure that follows later in deformation behavior of martensite (section 4.2.3). However, the martensite islands in DP1 contain more PAG boundaries.
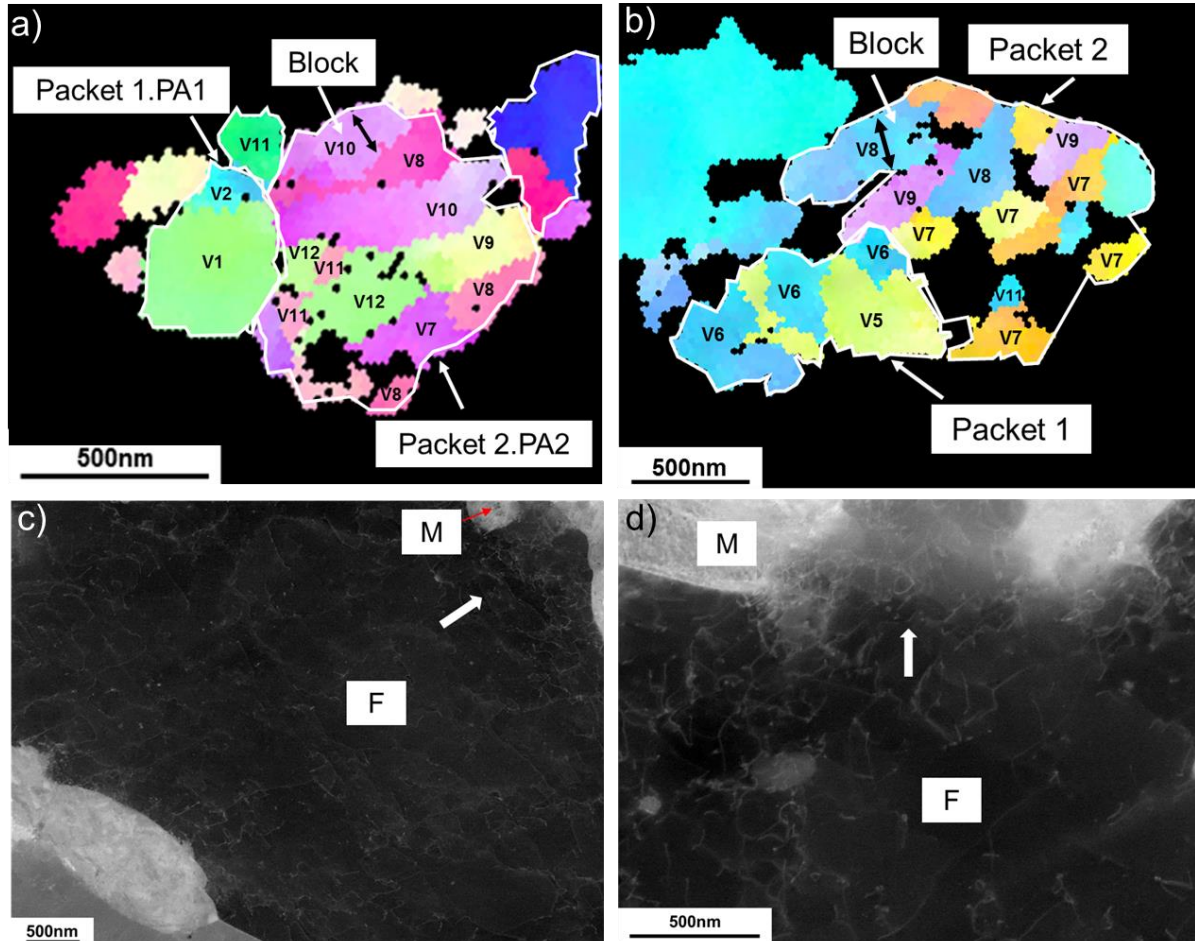
Fig. 4.2 (a) and (b) are the IPFs of two martensite islands out of DP1 and DP2, respectively, showing the identified substructures. Detailed interpretation of variants is referred to [45]. (c) and (d) are the ECCI images of DP1 and DP2. F represents ferrite and M means martensite.

In addition, we have applied ECCI to investigate the dislocation structure in our materials. Both DP grades have a high dislocation density in ferrite of the order of 1×10^{13} m^{-2}. In the shown grain, the approximate value is 4.5×10^{13} m^{-2} for DP1 and 1.6×10^{13} m^{-2} for DP2, indicating a higher dislocation density in the ferrite of DP1. Besides, a dislocation density gradient exists with low dislocation density in the ferrite interior towards a higher dislocation density near the phase boundary (see Fig. 4.2c and d, along the arrow).

We further measured the local element distribution using APT to thoroughly understand the differences of both DP steels. One example is presented in Fig. 4.3, showing the elemental distribution at a ferrite/ martensite boundary from DP2. Two aspects are observed: First, there is an enrichment of Mn, Cr and C along the interphase boundary but a homogenous distribution of Mn and Cr in ferrite and martensite. Second, almost all carbon is located inside the martensite, where the C content reaches an average value of 3.12 ± 0.13 at.%. The result is consistent with three other pure martensite tips from the same DP grade. However, the C content drops significantly to 0.28 ± 0.03 at.% inside ferrite. The content of Mn, Cr and Si in martensite are 2.08 ± 0.05 at.%, 0.80 ± 0.04 at.% and 0.58 ± 0.03 at.% while in ferrite they reach 1.37 ± 0.03 at.%, 0.52 ± 0.03 at.% and 0.44 ± 0.02 at.%. Note that the element distribution is consistent within three pure ferrite tips of DP2, and DP1 has a similar element content of ferrite except that it contains almost no Cr, as coinciding with the wet chemistry results.
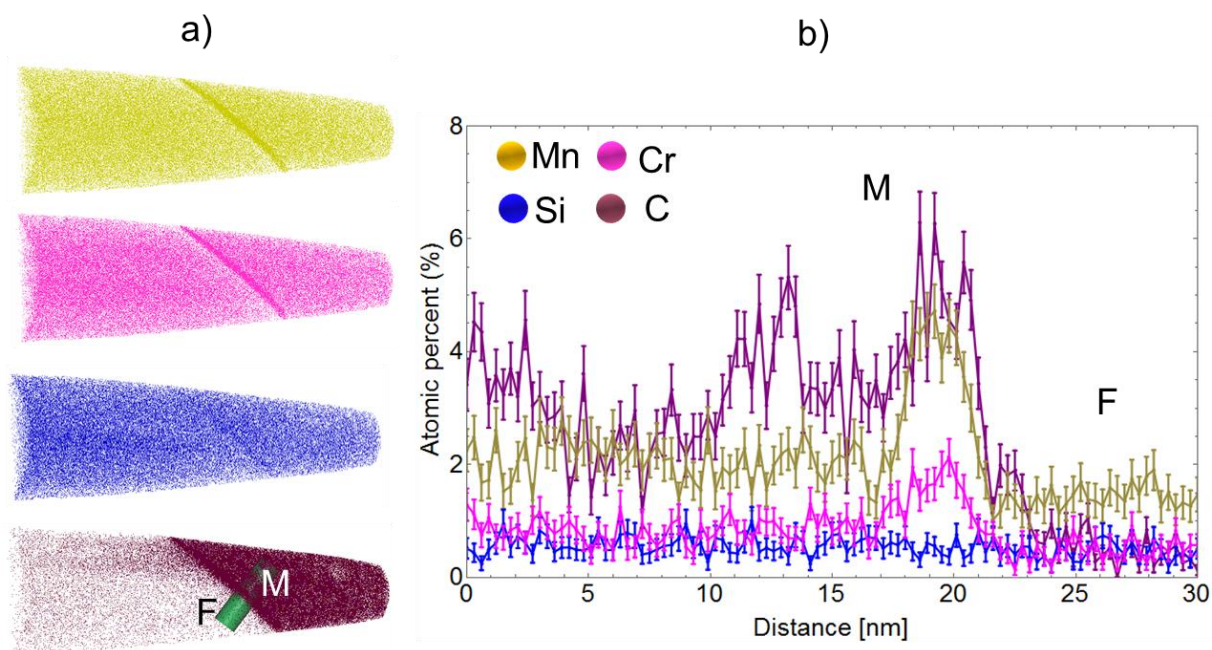
Fig. 4.3 (a) One representative APT tip from DP2 with ferrite and martensite phase boundary showing elements distribution; (b) element content variation along the green cylinder region.

Differences of the carbon distribution inside the martensite of the two DP steel grades are shown in Fig. 4.4, where the 5 at.% carbon isosurface is used. The C distribution is heterogeneous in martensite, especially in DP1 where it locally can reach up to 25 at.% (Fig. 4.4c), implying that Fe_3C carbides formed in the martensite in DP1. The forming sites are very likely to be at block boundaries, since the two highly carbon concentrated isosurfaces have a distance in the order of 100nm which correlates well with the block width (see Fig. 4.2a). By contrast, the carbon

enrichment in martensite in DP2 is significantly lower (maximum up to 10 at.%) and the distance between regions with high C content is smaller. Hence, here we conclude that C is enriched either at laths boundaries or at dislocation lines, but not at block boundaries.
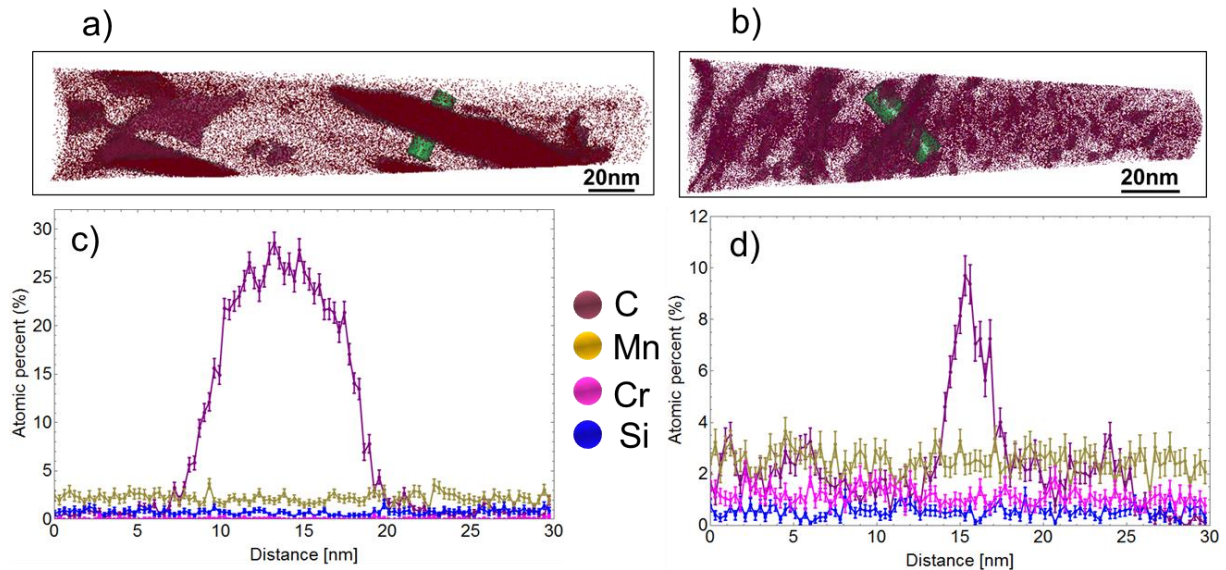
Fig. 4.4 (a) and (b) show the carbon distribution in two martensite tips from DP1 and DP2 together with the 5 at.% carbon isosurface. (c) and (d) are element content variation inside the two green cylinder regions. The two cylinders have the same size.

4.2.2 Micro plasticity of ferrite

This chapter mainly describes the DP2 steel grade. For determination of the activated slip system and the CRSS we combine post mortem SEM images and snapshots taken from the *in situ* deformation. By this approach we can identify the slip system activated first which will be the one analyzed subsequently. Differences between the two steel grades DP1 and DP2 are summarized in the last section of this chapter (4.2.2.4). In total, 73 ferrite pillars and 33 martensite pillars were tested on DP2, while 50 ferrite pillars and 31 martensite pillars on DP1. Only those with identifiable slip trace for ferrite and those with full martensite were considered in data analysis.

4.2.2.1 Measuring the cumulative distribution function (CDF) of the CRSS

Micro compression testing was performed to analyze the CRSS in the ferrite grains with different orientations. The crystallographic slip plane was indexed on *in situ* and *post mortem* SEM images using EBSD data as described above. The code thereby is superimposing the

{110}, {112} and {123} plane families as typically observed for bcc structures (Fig. 4.5, Column III).
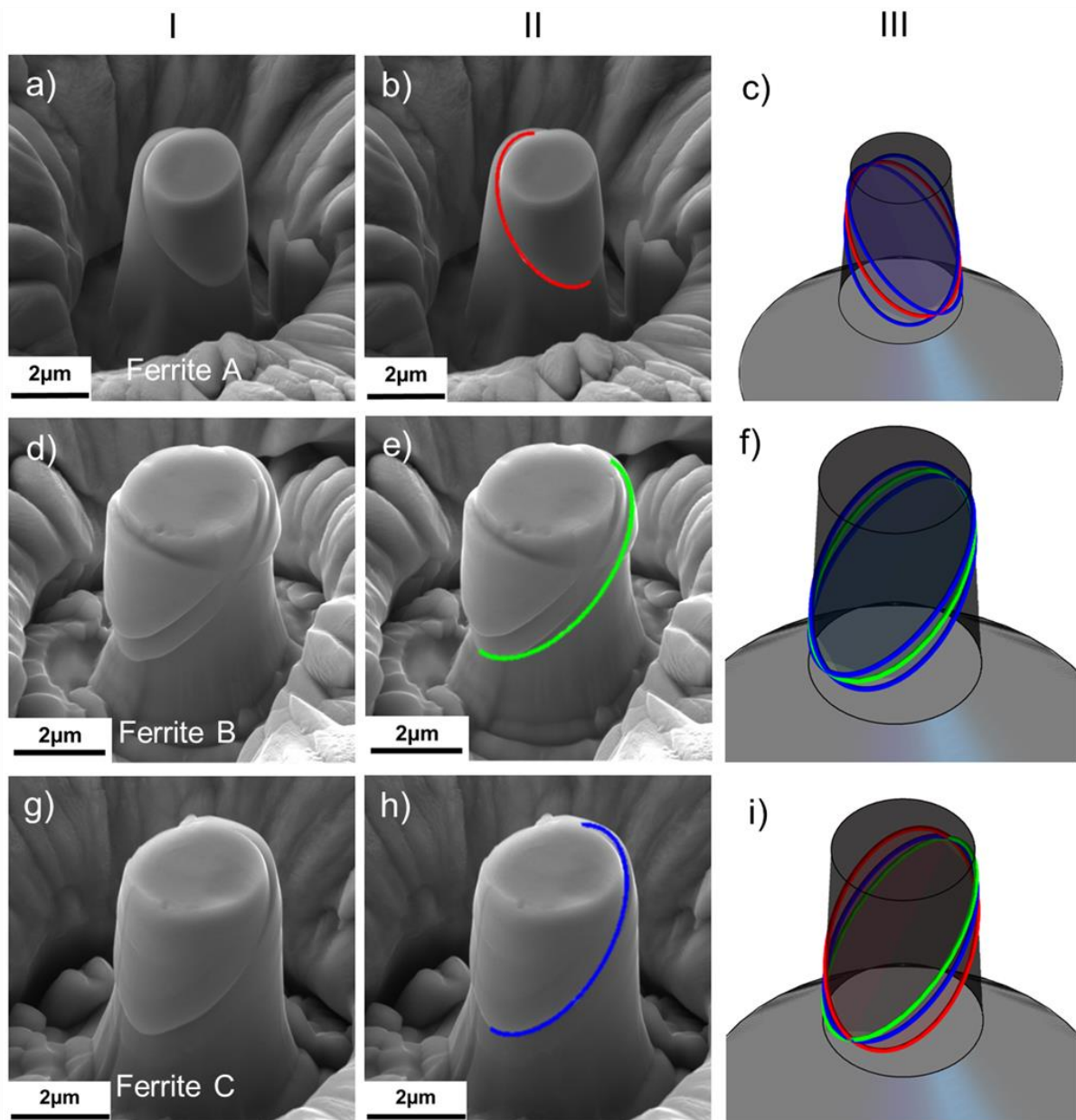
Fig. 4.5 Slip traces in ferrite. Colum I presents the post mortem SEM images. Column II shows superimposed identified slip traces and column III additional but not identified slip traces. Pillar (a), (d) and (g) are representative for {110}, {112} and {123} slip plane activation, respectively.

In far most cases, the single crystalline compression pillars exhibited only one dominating slip plane after an engineering strain between 10% and 15% (see for instance Fig. 4.5a). All three slip plane families are found active during pillar compression in our tested samples with examples for every family presented in each row of Fig. 4.5. In total, eight successfully tested

60

pillars activate the {110} slip planes, six pillars the {112} and twelve pillars the {123} first. The corresponding activated slip system and Schmid factor are given in Table 4-1. As expected from Schmid´s law all activated slip systems have a very high Schmid factor, however, not necessarily the highest (e.g. Ferrite C), especially if several slip systems exhibit a similar value. This phenomenon has been reported previously by Ng and Ngan [151] and is rather attributed to the limited number of dislocation sources in the finite pillar volumes then to non-Schmid effects. When a second slip system is activated (e.g. shown in Ferrite B), only the first activated system as determined by the *in situ* recording was taken for the subsequent CRSS calculation.

Table 4-1 Analysis of the activated slip systems for pillars presented in Fig. 4.5. The three closest planes possibly matching the experimental pattern best are shown. The identified slip system and corresponding Schmid factor are highlighted.

Representative Pillars	Drawn slip systems	Schmid Factor	Compressive yield strength /[MPa]	CRSS /[MPa]
Ferrite A	*$(0\bar{1}1)[\bar{1}11]$*	*0.50*	277	138
	$(13\bar{2})[\bar{1}11]$	0.48		
	$(1\bar{2}3)[\bar{1}11]$	0.46		
Ferrite B	*$(\bar{1}12)[1\bar{1}1]$*	*0.50*	334	166
	$(\bar{2}13)[1\bar{1}1]$	0.49		
	$(\bar{1}23)[1\bar{1}1]$	0.49		
Ferrite C	$(0\bar{1}1)[\bar{1}11]$	0.49		
	$(13\bar{2})[\bar{1}11]$	*0.49*	304	149
	$(12\bar{1})[\bar{1}11]$	0.46		
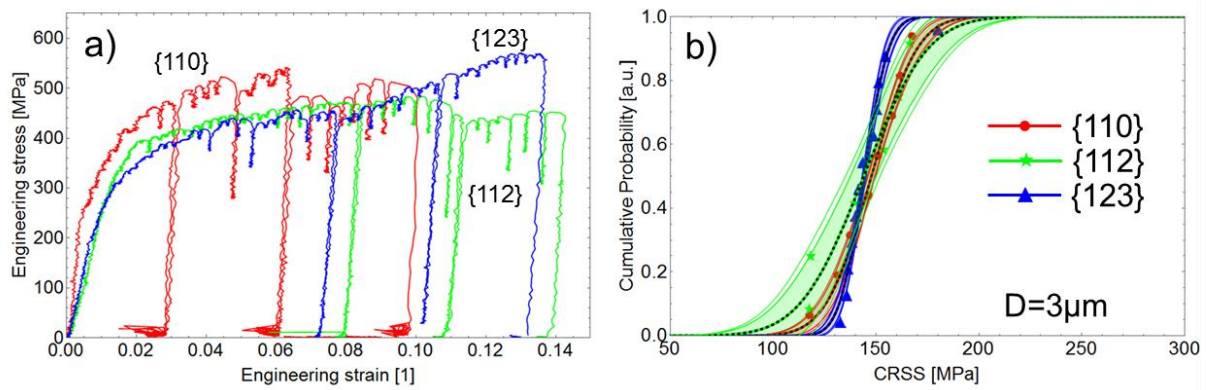
Fig. 4.6 (a) Engineering stress versus strain curves for three representative pillars, labeled with the determined activated slip plane. (b) The cumulative probability function (CPF) of the CRSS for the three slip plane families. In total, twenty-six 3 µm sized samples of the DP2 steel grade are used for this plot.

The engineering stress versus engineering strain curves of the single crystalline micro pillars show a jerky-like flow typical for the investigated size regime (see Fig. 4.6a) [63, 150, 152]. The engineering stress at a plastic strain of 0.5% was taken to compute the CRSS based on the previously identified slip plane.

Finally, the cumulative distribution function (CDF) of the CRSS was plotted for all three slip plane families (see Fig. 4.6b) and fit by a Gaussian distribution as summarized in Table 4-2. In case of 3 µm sized pillars the mean CRSS of the {110} family equals 147 ± 6 MPa, of the {112} 143 ± 9 MPa and of the {123} 146 ± 4 MPa. Hence, surprisingly, within the standard error of the mean value, the CRSS of all three families is identical (here shown for 3 µm sized pillars of the DP2 steel grade).

4.2.2.2 Size effects of the DP2 steel grade

Ferrite grains exhibit a clear size effect (see Fig. 4.7 for the {110} ⟨111⟩ slip system) with 2 µm sized pillars being systematically stronger than their 3 µm sized counterparts (2 µm: 179 ± 11 MPa, 3 µm: 147 ± 6 MPa). Also, the 2 µm sized pillars show a higher dispersion, as evident from the distribution width in the cumulative distribution plot (see Fig. 4.7a) and the scatter in CRSS for pillar diameters (see Fig. Fig. 4.7b). Unfortunately, it is impossible to test pillars larger than 3 µm in diameter due to the limited grain size and smaller pillars than 1 µm due to

the limited force resolution of the indenter, which prevents a meaningful quantification of a size scaling law.
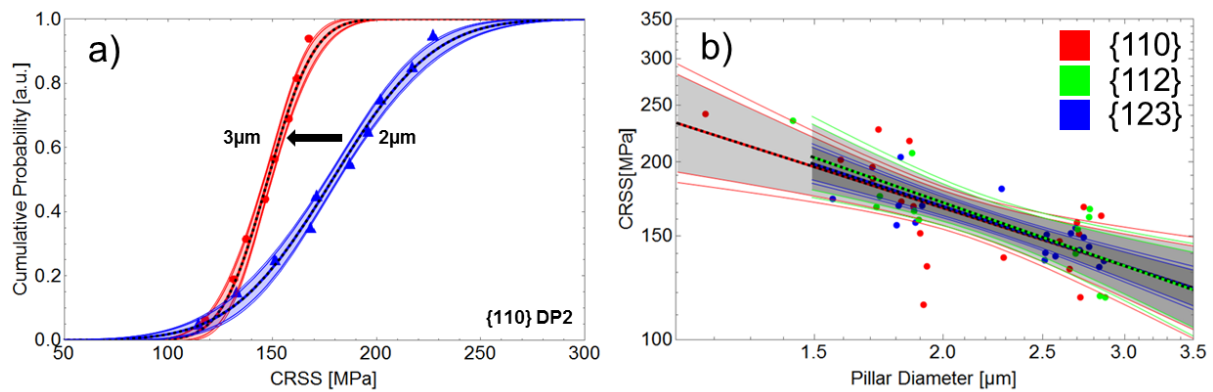
Fig. 4.7 (a) The CRSS distribution curves of 2 µm and 3 µm sized pillars of DP2. (b) Size scaling of the CRSS in the size regime from 1 µm to 3 µm.

4.2.2.3 Orientation effects on the activation of slip systems in the DP2 steel grade

The aforementioned CRSS distribution of the three families as well as their size distribution might also allow for analyzing orientation effects on the CRSS. For this purpose we have color coded the activation of the $\{110\} \langle 111 \rangle$, $\{112\} \langle 111 \rangle$ and $\{123\} \langle 111 \rangle$ slip systems in an inverse pole figure (IPF, see Fig. 4.8a). The plot thereby assumes an identical CRSS of all three slip system families, which agrees well with the findings reported in section 4.2.2.1.

In addition, the experimentally identified slip systems for 2 and 3 µm sized pillars are presented in Fig. 4.8b and c. In case of the 3 µm sized pillars the experimentally observed slip system activation predominantly follows the Schmid predictions with only few outliers documenting the dominance of Schmid´s law for the 3 µm sized samples. In case of 2 µm sized pillars the number of outliers seems to slightly increase (see Fig. 4.8e), nevertheless, the majority of pillars still follow Schmid´s law and non-Schmid effects do not play a significant role in slip activation here. We address the outliers to the limited number of dislocation sources in the finite sample volume which results in a statistical "Break Down of Schmid´s law" as proposed by Ng and Nghan [151]. Also, it should be noted that in the case of outliers the CRSS of the activated slip system is very close to the CRSS of the primary slip system exhibiting the highest available Schmid factor.
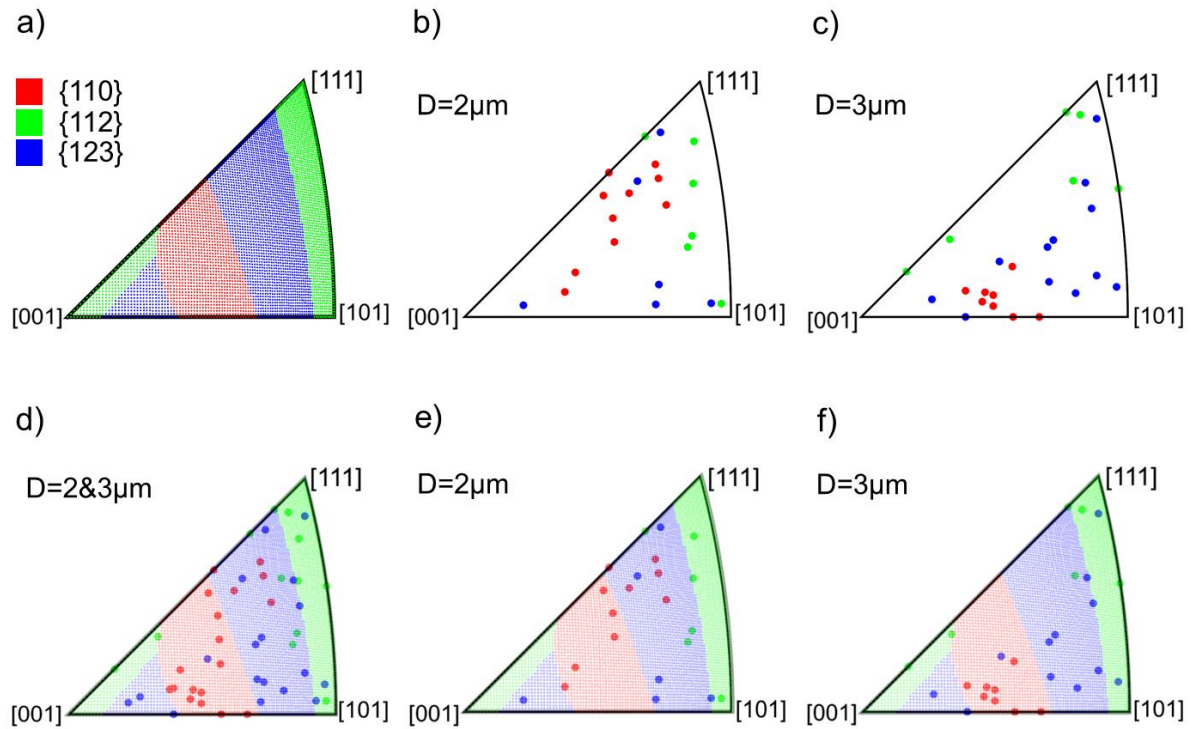
Fig. 4.8 (a) A colored IPF that shows the region where {110}, {112} or {123} plane groups possess the highest Schmid factor. (b)-(c) are the tested orientations of 2 µm and 3 µm ferrite pillars. They are colored according to experimentally identified activated primary slip planes, {110} as red, {112} as green and {123} as blue. (d)-(f) comparison of the experimental data points with the distribution of highest Schmid factor.

4.2.2.4 Grade effect of DP1 and DP2

Finally, let us focus on the differences of the ferrite of the two steel grades DP1 and DP2 as shown in Fig. 4.9. The 3 µm pillars milled from DP1 systematically yield at a significantly higher stress and exhibit a substantially higher CRSS as compared to the ones obtained from DP2. The mean CRSS of DP1 {110} slip plane group reaches 205 ± 8 MPa, which is approximately 60 MPa larger in comparison to 147 ± 6 MPa of DP2 (see Fig. 4.9b and c).

Similar to the previously described size scaling in DP2 (see section 4.2.2.2), the 2 µm pillars of DP1 show a very broad distribution of the CRSS ranging from 200 MPa to 300 MPa, while the 3 µm are less dispersed. Hence, comparing the two steel grades with macroscopically identical UTS we can conclude that, irrespective of the pillar size, DP1 exhibits a higher yield strength than DP2.

64

As a summary, the results of all the tested pillars are given in Table 4-2 with the mean value and dispersion width of CRSS. The abovementioned points in terms of activated slip planes, orientation dependence and size effect are valid as well in the DP1 steel grade.
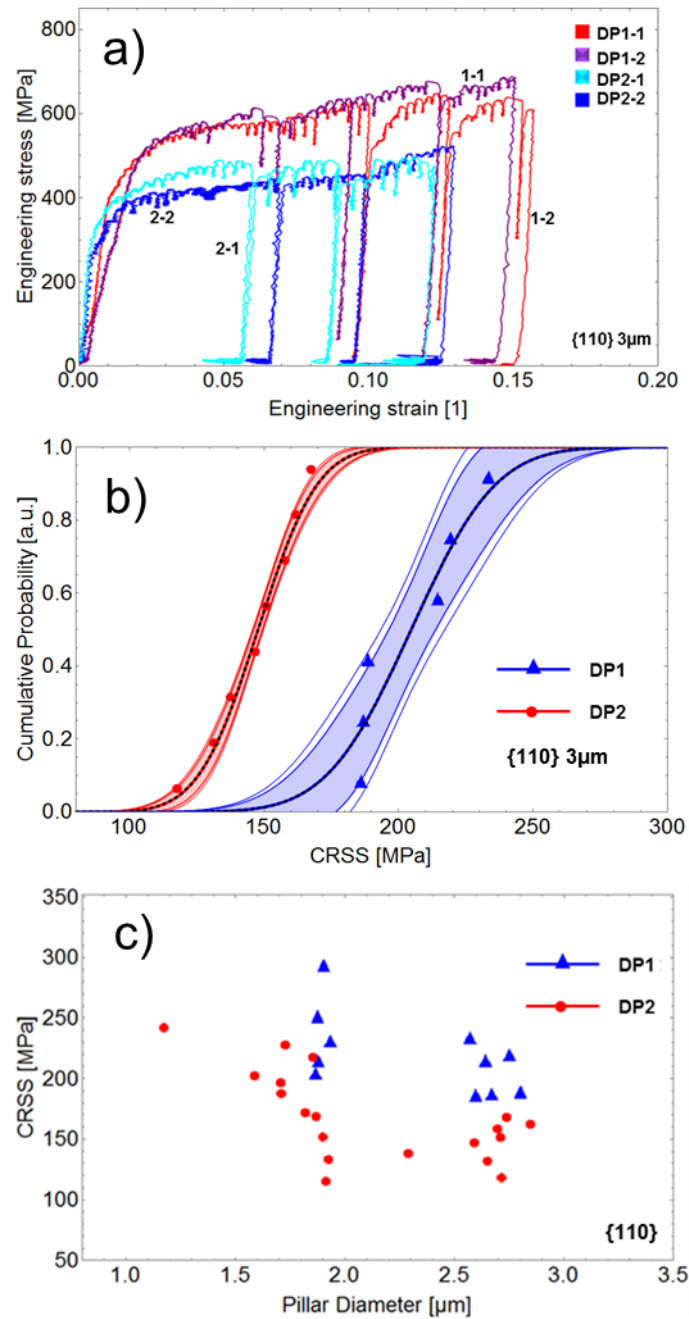
Fig. 4.9 Comparison of two DP800 steel grades: (a) Engineering stress versus strain curves of ferrite compression pillars; (b) the ferrite CRSS distribution of 3 µm pillars and (c) the size scaling plot of the CRSS in the limited size regime from 1 µm to 3 µm. Only {110} slip systems are shown.

Table 4-2 Summary of the CRSS of ferrite pillars of the two steel grades and different diameters. The mean CRSS value and the dispersion of the CRSS are given. In both cases the error bars are given as the standard error of the mean.

Steel grade	Pillar size	Slip planes	Mean value [MPa]	Dispersion width [MPa]
DP1	2μm	{110}	239 ± 16	32 ± 5
		{112}	197 ± 16	46 ± 7
		{123}	220 ± 17	41 ± 12
	3μm	{110}	205 ± 8	25 ± 6
		{112}	204 ± 6	11 ± 5
		{123}	199 ± 9	29 ± 3
DP2	2μm	{110}	179 ± 11	38 ± 2
		{112}	185 ± 12	30 ± 10
		{123}	172 ± 7	11 ± 3
	3μm	{110}	147 ± 6	17 ± 1
		{112}	143 ± 9	24 ± 4
		{123}	146 ± 4	9 ± 1

4.2.3   Micro plasticity of martensite islands

Within this section we focus on the deformation behavior of the martensite islands with their complex colony structure. The hierarchical microstructure of our martensite islands, including a number of interfaces forming a complex substructure, is shown in the IPF (see Fig. 4.10a). The block size (see Fig. 4.10a) typically reaches dimensions of approximately 100 nm. Therefore, our micropillars do not contain one isolated martensite block but involve single martensite islands including their complex substructure.
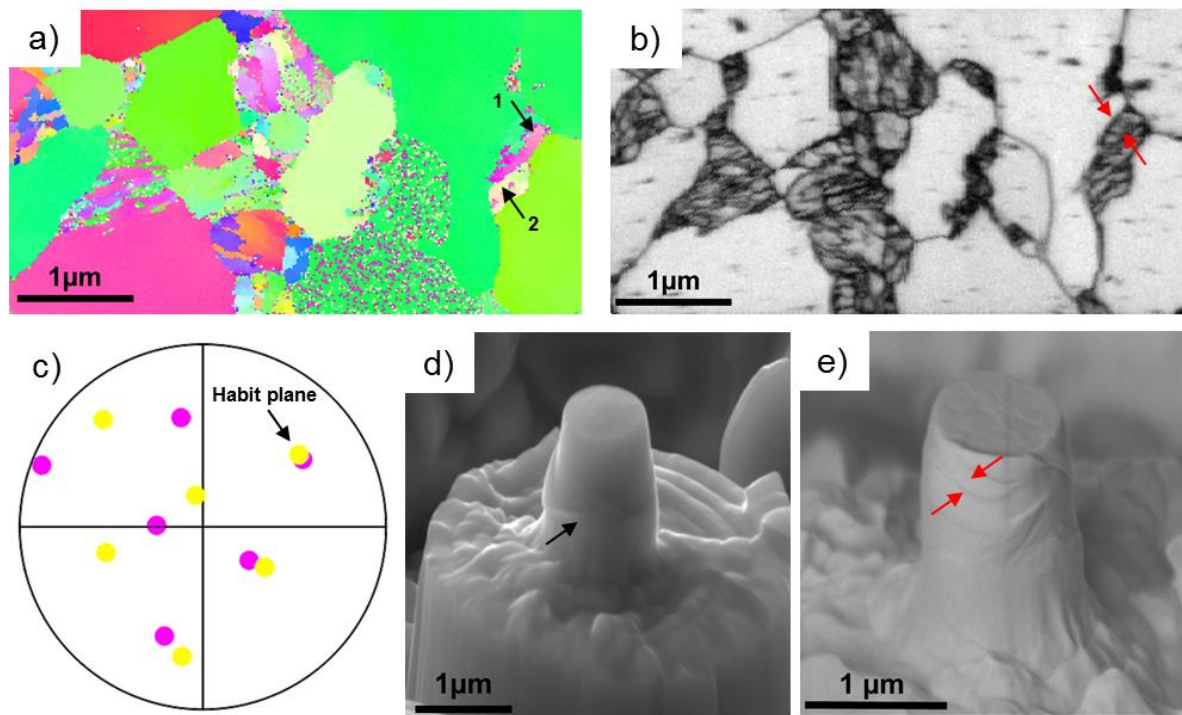
Fig. 4.10 (a) and (b) IPF and IQ map of DP1 indexed by ferrite to show the substructures of martensite. (c) presents the {110} pole figure of substructure 1 and 2 in (a). (d) and (e) show two compressed martensite pillars, where the black arrow indicates sink-in (d) and red arrow the slip trace in (e).

During pillar compression, we observe barreling of the entire pillar which is occasionally accompanied by discrete slip traces. The discrete slip traces had previously been interpreted as slip at block-boundaries [153-155]. Also in our case the block size as measured from EBSD image quality (IQ, Fig. 4.10b) maps show a similar dimension as observed in the slip traces in Fig. 4.10e. Furthermore, as proven through the ⟨110⟩ pole figures of the substructures 1 and 2 (Fig. 4.10c), the interface between them is a block boundary. Hence, the discrete slip traces on the pillar surfaces are consistent with the interpretations of C. Du et al. [153] and Y. Mine et al. [155].

Also the engineering stress versus engineering strain curves (see Fig. 4.11a) document the deformability of martensite islands at the micron scale. After linear elastic loading the martensite of both DP grades exhibit significant plastic deformation during the compression experiment. Even though some stress drops occur in the microscale martensite, the overall appearance of the engineering stress vs. strain curve is much smoother compared to the ferrite pillars.

Due to the limited martensite island size the martensite pillars might contain softer ferrite at the bottom, which significantly influences the stress strain behavior (see black curve in Fig. 4.11a). By testing more than 30 pillars, we differentiated such cases by two aspects: (i) the ferrite containing pillars tend to exhibit a sink-in upon compression, where the entire pillar or parts of it can be pushed into a plastically deforming ferrite island (see Fig. 4.10d); (ii) fully martensitic pillars exhibit significantly higher flow stresses among the compression engineering stress versus engineering strain curves (see Fig. 4.11a). Following this approach we cannot exclude the possibility of a significantly softer martensite at the bottom of our martensite pillars, similar as previously observed in TEM [14]. Therefore, our data only contains the high strength martensite and would not allow to discuss the occurrence of low strength martensite – if at all existing or present.
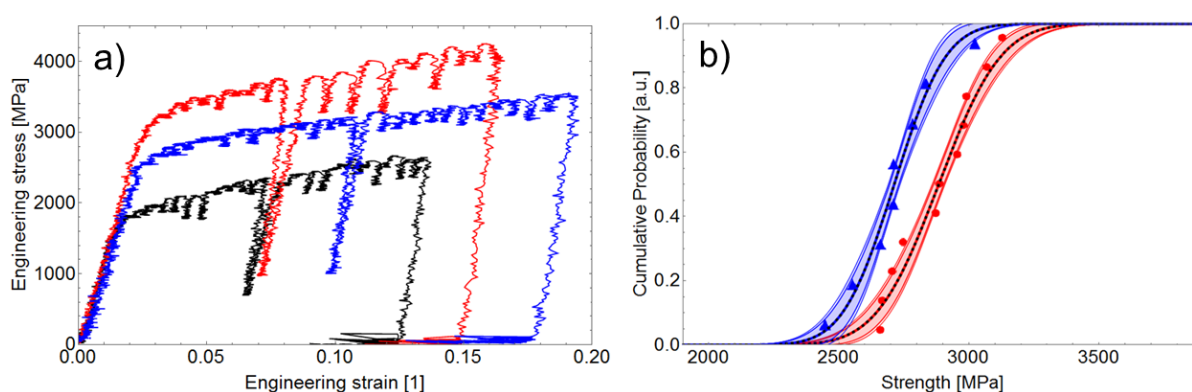
Fig. 4.11 (a) Engineering stress versus strain curves of martensite micropillars from the two DP800 grades. The black curve represents a martensite pillar which sunk in due to an invisible ferrite base. (b) The distribution of the compressive yield strength extracted at a plastic strain of 0.01 martensite micropillars of DP1 and DP2.

In this way, the pure martensite pillars of both DP steels and their strength distribution function were analyzed (see Fig. 4.11b). The martensite islands in both DP1 and DP2 yield at a surprisingly high mean stress level of 2716 ± 62 MPa and 2880 ± 49 MPa, respectively. I.e., on average, martensite colonies in DP1 have a slightly lower yield strength.

4.3 Discussion

4.3.1 Slip systems of ferrite

We performed micropillar compression tests on the microstructure constituents ferrite and martensite in DP800 to microscopically investigate their deformation behavior to deeper understand their macroscopic mechanical behavior. Our BCC ferrite pillars showed the

68

activation of all three possible slip plane families, namely {110}, {112} and {123} all owning a ⟨111⟩ Burgers vector at comparable CRSS.

As first crude estimate we want to refer to the stress required to move a dislocation through a lattice, the Peierls stress $\tau_p = \frac{2G}{1-v} \exp\left(-\frac{2\pi}{(1-v)}\frac{d}{b}\right)$ with G being the shear modulus, v the Poisson´s ratio, d the lattice spacing and b the magnitude of the Burgers vector. The Peierls stress on higher index planes should be significantly higher and, therefore, it should be more difficult for dislocations to move on those planes. The Peierls equation above was originally deduced based on the Peierls-Nabarro (P-N) model, where a single straight edge dislocation with a planar core structure in a simple cubic structure was considered at 0 K [156, 157]. However, the screw dislocations that dominate the deformation of BCC metals are believed to have non-planar structures and move forward through the kink-pair mechanism including nucleation of a kink-pair and lateral motion of the kinks. Temperature and stress have a great influence on the core structure and hence the kink-pair formation [24, 158] which renders slip in bcc more complex. Therefore, it is not reasonable to assess the possibility of the activated slip systems merely based on the Peierls stress of the P-N model. The simple Peierls stress approach does not work [156-158].

Our result are complementary to the observations reported in references [159-162] showing the activation of {110} and {112} slip planes only. A possible explanation for the additional activation of {123} slip is that the former studies of C. Du et al. [159] and Franciosi et al. [162] were not conducted on orientations favoring {123} slip (e.g. see Fig. 4.8). Although constant efforts have been made to explain the hardening/softening of iron caused by the addition of the foreign atoms, their complex influence on the activation of slip planes still remains an open question [67, 163]. Hence, another reason might be that we investigated chemically non-pure iron pillars from a commercial DP800 steel grade and not high purity iron [161].

Let us note that the above mentioned slip planes are all identified by means of SEM images and, therefore, are averaged planes within the resolution provided by field emission SEM microscopy. Caillard concluded from thorough transmission electron microscopy (TEM) investigations with significantly higher lateral resolution that the elementary slip planes are {110} types in Fe, irrespective of the investigated alloying elements (see the work of [25, 26, 67, 163]). According to Caillard an apparent average plane – as we observed – can be realized by continuous intensive cross slip between two {110} planes. Caillard´s view is supported by molecular dynamics simulations from Gilbert et al. [164], who identified that glide on {112} in

pure iron is only observed from length scales far above the atomistic one. Also in their case {112} slip occurs via numerous cross-slip events on {110} planes at an atomic scale. Note that the cross slip phenomenon is particularly strong in bcc structures since the plastic deformation is mainly controlled by the slower motion of screw dislocations [18, 165]. In light of the atomistic simulations [164] and experimental work [25, 26, 67, 163] an identical CRSS of slip on {110}, {112}, and {123} can be explained in terms of averaged Schmid factors on constituting, elementary {110} slip planes. It´s still interesting to note that the slip traces appear to originate from flat slip planes in the SEM, which requires that the cross-slip process on two elementary {110} planes happens extremely periodically.

A non-Schmid behavior is frequently discussed for bcc [166-168]. In our work, the magnitude of the CRSS of the three slip plane families is within the resolution provided by pillar compression identical for all three systems irrespective of the loading direction. The Schmid factor reasonably well predicts the activation of activated slip systems in ferrite for both steel grades (see Fig. 8). The slip plane experiencing the highest Schmid factor, e.g. the highest resolved shear stress, is in far most cases activated first. This behavior indicates that the non-Schmid phenomena, at least in our case, play a minor role. Nevertheless, occasionally – particularly for the smaller sized pillars and in regions with minor differences in Schmid factors – we observed the activation of the slip plane with the second or third highest Schmid factor. This phenomenon had previously been entitled "Breakdown of Schmid´s law" and reflects the important role of the availability and size of dislocation sources in micron sized samples [151]. Du et al. and Francioso et al. found similar results for {110} and {112} planes [159, 162].

4.3.2 Size effects in DP800 ferrite grains

The breakdown of Schmid´s law at small dimensions is not the only consequence of reduced sample dimensions we observe here. Due to the dimensional constraints dislocation sources are potentially smaller in smaller pillars, resulting in a "smaller is stronger" effect [169, 170]. This also holds true for both of our DP steels. In our work, smaller pillars indeed exhibit a higher mean CRSS than larger ones (see Table 4.3). Also, a much larger CRSS dispersion of 2 µm sized pillars exists compared to 3 µm (compare the scatter in Fig. 4.8b), being another aspect of the size effect (see for instance Bei et al. [171] and Phani et al. [172]).

The dislocation density gradient across the ferrite grain in our DP steels as observed via ECCI imaging (see Fig. 4.2c and d) also contributes to the size scaling in the ferrite grains. A higher

dislocation density is observed near the phase boundary between ferrite and martensite to accommodate the volume expansion during the martensitic transformation. This observation is consistent with research work of Tasan et al. [131] and Kadkhodapour et al. [138]. We have milled all our pillars with the intention to locate them in the center of one ferrite grain. Hence, a 3 µm pillar is more likely to contain a higher density of dislocations (therefore dislocation sources) than a 2 µm pillar. Since the number of dislocation sources is known to play a dominant role in the deformation behavior of materials at the micron scale we ascribe the significant drop of the CRSS within the small changes of the pillar diameter to the increased number of pre-existing dislocation sources and lower activation stress. Hence, the size scaling effect of the CRSS observed here is a sampling effect where larger pillars contain disproportionately more dislocations due to the vicinity to the martensite (see Fig. 4.8b and c).

4.3.3   Deformation behavior of martensite

The martensite in both investigated steel grades presents, in accordance with low carbon steel with less than 0.8 wt% C, a lath morphology [173]. The martensite islands in our DP steels exhibit homogenous plasticity with only few deformation traces. The plasticity at the traces is related to the deformation along the block boundaries because the block boundary is {110} plane type that is a potential slip plane family for near bcc martensite. If the block boundary exhibits a high resolved shear stress, gliding along the block boundary is observed [153]. Hence, sliding of block boundaries can enhance plasticity of martensite. However, if the maximum resolved shear stress has a large angle to the block boundary, this interface acts as an effective barrier for dislocation slip and, therefore, restricts plasticity of martensite [155].

In our tests the milled pillars can contain several block boundaries that are even non-parallel to each other if more than one packet exists. As a result, multiple slip systems can be activated. Instead of simple slip traces observed in ferrite, the martensite pillars show barreling in most cases with occasionally local deformation traces along the block boundaries. The local deformation appears to terminate at packet boundaries. These local sliding along the block boundaries might cause the small load drops on the engineering stress versus engineering strain curve, while the packet boundary contributes to the high yield strength of the martensite island. Ghassemi-Armaki et al. [142] found that micropillars containing one packet boundary behave similar to bulk lath martensite in terms of the yield strength. Therefore, we can expect that a

bulk martensite comprised of such fine substructures like in our case can reach a yield strength up to 3 GPa.

4.3.4 Comparison of the DP steel grades

We have studied two DP steels and both have identical ultimate strength fitting the DP800 classification. However, under the same tensile test conditions, they show significantly different uniform and fracture elongation as well as yield strength. DP2, with a larger mechanical heterogeneity, unexpectedly exhibits a higher uniform and total elongation that might be caused by a higher work hardening potential of softer ferrite in DP2 and can suppress a rapid growth of cracks. However, the current work does not allow for an quantitative assessment of the local work hardening ability of ferrite and, therefore, additional work at different engineering macro strain levels needs to be done to shine light on the damage behavior.

Besides, we found that ferrite with higher CRSS corresponds to a higher yield strength of DP steels which is consistent with the picture of ferrite playing the dominant role in the early yielding behavior. Still, the differences in ferrite CRSS can be discussed.

Our APT data shows that the chemical composition of ferrite in both DP steel grades does not vary significantly. Cr is the only element differing, which is entirely in solid solution. The minor chemical variation between the two steel grades cannot explain the strength difference observed in pillar compression.

In contrast to the chemical distribution, the dislocation density is different for both steel grades. The ferrite having a smaller grain size in DP1 possesses a higher dislocation density (see Fig. 4.2c and d). Hence, we hypothesize without proof that the ferrite CRSS difference at yielding is rather caused by differences of the dislocation density instead of chemistry of ferrite.

By contrast, the carbon distribution and content in martensite of two DPs varies largely. The formation of carbides in DP1 significantly decreases the carbon in the solid solution state (Fig. 4.4). The C depletion of martensite can reduce the strength of martensite by allowing for local dislocation activity. The critical substructure size for deformation in the martensite island is the block width that is approximately 100 nm in both steels (Fig. 4.2c and d). Hence, we think that the dominating factor for the differences in martensite strength here is the heterogeneous carbon distribution and formation of carbides.

4.4 Conclusion

We have performed micropillar compression tests on ferrite and martensite in two DP steels in order to investigate their micromechanical behavior. Besides investigating and quantifying the microscopic mechanisms of slip in the two phases we also linked the microscopic properties to the macroscopic mechanical behavior in terms of yield strength. Our findings can be summarized as:

- All three slip plane families, namely {110}, {112} and {123} can be activated in ferrite, tested at room temperature and a strain rate of 1×10^{-3} /s. The corresponding CRSS is identical (147 ± 6 MPa, 143 ± 9 MPa and 146 ± 4 MPa) for 3µm pillars. In the vast majority of the samples the activated slip system can be predicted by the Schmid factor.

- A size effect exists for the single crystalline ferrite pillars. Namely, the CRSS of 2 µm sized pillars is significantly larger than the one of 3 µm pillars (compare 179 ± 11 MPa to 147 ± 6 MPa). Besides the current explanations of the sample size effect, the dislocation density gradient from the grain center to the phase boundary plays an important role as the number of pre-existing dislocation sources is disproportionately higher in larger pillars.

- The martensite island yields at a very high strength up to nearly 3 GPa. The pillars mostly exhibit barreling similar to polycrystalline structures under compression. This is caused by the complex substructures and boundaries with a significantly smaller length scale as the pillar diameter. Occasionally, deformation traces occur at block boundaries.

- The two DP steel grades show an identical macroscopic ultimate tensile strength (UTS). However, the individual phases show totally different strength. For instance, the CRSS of ferrite in DP1 and DP2 are 205 ± 8 MPa and 147 ± 6 MPa while the strength of their martensite is 2716 ± 62 MPa and 2880 ± 49 MPa, respectively.

- The ferrite phase is responsible for the early yielding of DP steels. A smaller CRSS of ferrite corresponding to a smaller yield strength of DP steels.

5 Influence of strain rate on the activation of {110}, {112}, {123} slip in ferrite of DP800[3]

5.1 Introduction

DP steels are a class of high strength steels predominantly used in the automotive industry and are of utmost importance to the steel industry as well [47, 174, 175]. In our previous work [176], we showed that slip activation of ferrite in DP800 occurs for all three slip plane families, namely {110}, {112}, and {123}. The micropillar compression tests conducted in the aforementioned study were performed at room temperature and a strain rate of 10^{-3} s^{-1}. The mean CRSS values for all three slip systems above are nearly identical, and activation of the slip systems follows Schmid´s law. However, it is well-known that the deformation behavior of bcc materials has a strong temperature and strain rate dependence [177, 178]. For instance, temperature not only impacts the strength of bcc materials, but also which slip plane family is activated [179, 180]. At low temperatures, only straight slip traces on {110} slip planes are observed, while at medium and higher temperatures (compared with the critical transition temperature T_c, above which the thermal activation assisted dislocation motion is less important) slip on {110}, {112}, and {123} is evident in iron or ferrite [181, 182]. Former work on the impact of strain rate on the deformation behavior focuses either on single crystals with limited orientations or on nanocrystalline materials, and mainly describes the relationship between strain rate and size effects [22, 23, 183]. A systematic study of the influence of strain rate on activated slip systems at the microscale is still pending. Therefore, within this study, we aim to understand the strain rate dependence of the slip system activation.

5.2 Results

The *post mortem* images (see Fig. 5.1) were used in combination with the orientation information from EBSD to determine the activated slip system(s). For instance, the determined slip systems of the four pillars exhibiting single slip in Fig.1 are (011) [11$\bar{1}$], ($\bar{1}$12) [1$\bar{1}$1], (101) [11$\bar{1}$] and (2$\bar{1}$3) [$\bar{1}$11], respectively. The slip traces appear to be smooth in the SEM and no secondary slip systems are observed, as can also be seen in Fig. 5.1. Generally, if a secondary slip system was found to be activated for a given pillar, we only consider the slip system which was activated first. Among the 86 pillars, 49 show single slip system activation during the tested

strain range. The identification was, in such cases, based on snapshots from *in situ* recording. Only micropillars where the slip trace can unambiguously be identified are taken into account during the subsequent analysis of the influence of strain rate on slip system activation. In total, 71 out of 86 pillars are clearly identified regarding their slip trace. A more detailed description is presented in [184]. Note that the slip systems of the four pillars presented in Fig. 5.1 were activated according to the highest Schmid factor, regardless of the strain rate.
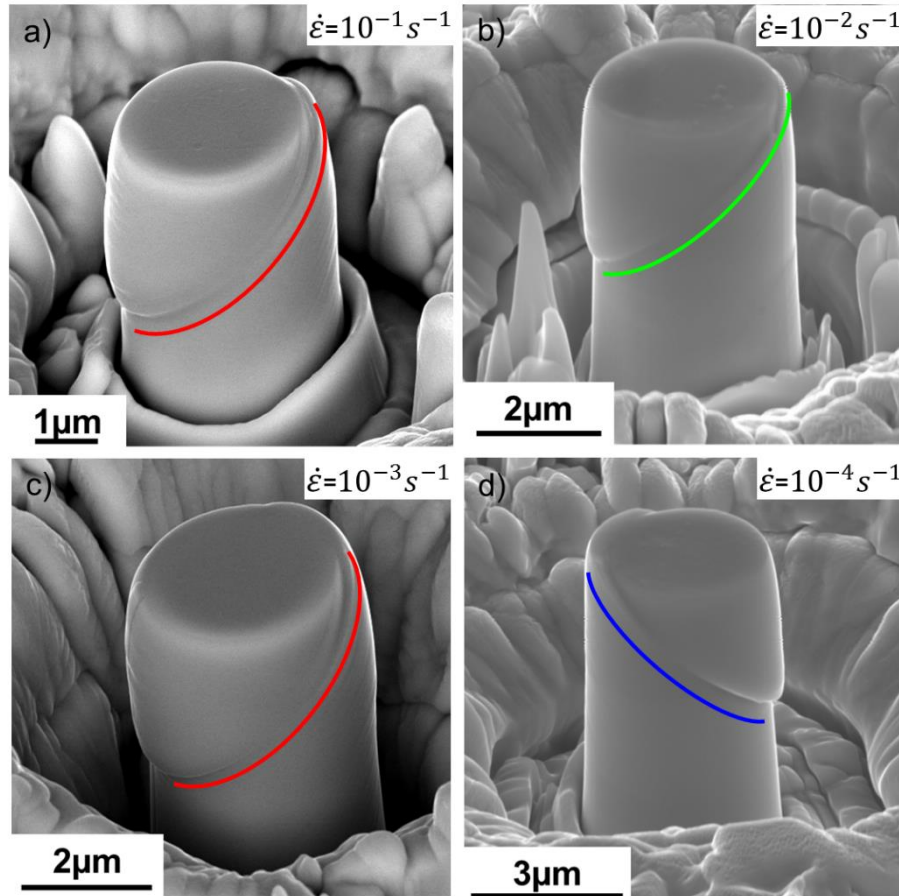
Fig. 5.1 (a)-(d) *Post mortem* SEM images recorded at the indicated strain rate. The identified slip system was overlapped slightly below the experimental slip traces. Red represents {110} slip systems, green {112} and blue {123}, respectively. Note that the pillars are milled from different grains and therefore exhibit a different orientation. Compression axes are (a) [11 25 1], (b) [$\overline{17}$ 19 6], (c) [$\overline{17}$ $\overline{9}$ $\overline{1}$] and (d) [$\overline{9}$ 6 $\overline{2}$].

This trend, that the slip system with the highest Schmid factor is activated for a wide range of strain rates, also remains when a large number of samples is tested. This can be seen in Fig. 5.2, where the identified slip systems are shown on inverse polefigures for the different strain rates used. In addition to the experimental data, Fig. 5.2 also color-codes the slip system family with

the highest Schmid factor from the {110}, {112} or {123} families. Given the possible uncertainty in determining crystal orientations using EBSD, we discard those experimental data points very close to or on the boundaries indicated by a bold line. The difference of the first and second highest Schmid factor at these orientations is within 2%. Consequently, if the CRSS of all slip system families is identical [176] and non-Schmid behavior can be neglected, the slip system activation is according to the color code presented in Fig. 5.2. In the investigated strain rate range we do not see a systematic shutdown of {112} and {123} slip system activation. At slow strain rates the slip systems are activated within the expected orientation, or at least close to it (see for instance Fig. 5.2c and d). However, with increasing strain rate (e.g. 10^{-2} and 10^{-1} s^{-1}) the probability of slip system activation in an unpredicted slip system rises. For instance, 5 out of 16 pillars tested at 10^{-1} s^{-1} do not activate the slip system expected from the Schmid factor, and neither do 8 out of 17 at 10^{-2} s^{-1}. By contrast, only 1 out of 14 and 2 out of 15 pillars activated unexpected slip systems when tested at the low strain rates 10^{-3} s^{-1} and 10^{-4} s^{-1}.
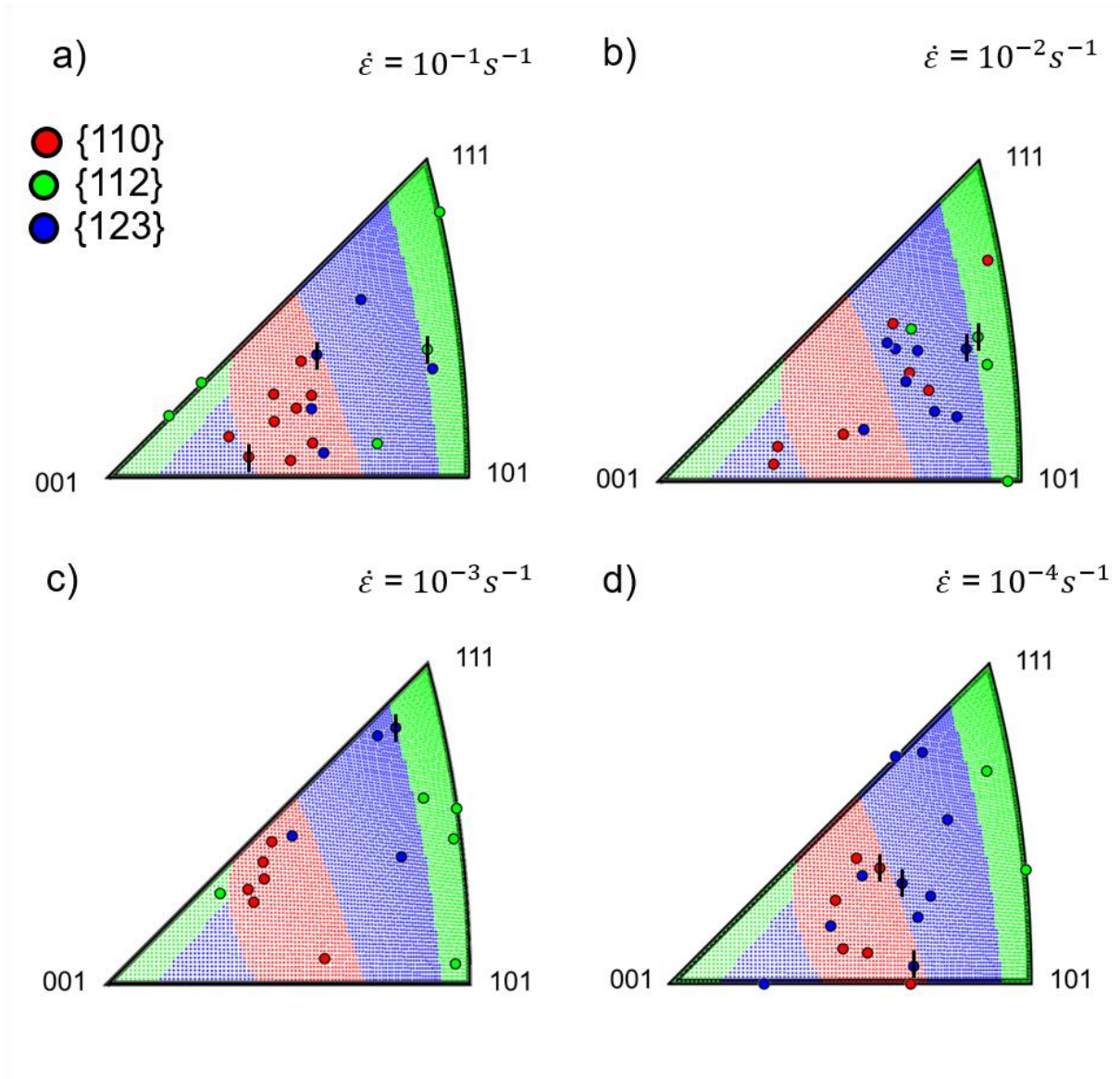
Fig. 5.2 Inverse polefigures showing the activated slip system (in cases where it was unambiguously identified) on top of the expected (background) slip system family according to the color code: Red represents slip on {110}, green on {112} and blue on {123} planes. Data points near or on the boundaries are discarded, marked by bold line. The strain rate varies: (a) 10^{-1} s^{-1}; (b) 10^{-2} s^{-1}; (c) 10^{-3} s^{-1}; (d) 10^{-4} s^{-1}.

Representative engineering stress versus engineering strain curves of nominally identically sized pillars are shown in Fig. 5.3a. The orientation of the four pillars from up to bottom is $(\overline{12}\,6\,\overline{1})[\overline{4}\,\overline{7}\,6]$, $(\overline{7}\,\overline{2}\,\overline{25})[\overline{19}\,4\,5]$, $(\overline{17}\,\overline{9}\,\overline{1})[\overline{10}\,17\,17]$, $(13\,4\,6)[2\,\overline{5}\,\overline{1}]$, while the corresponding Schmid factor is 0.50, 0.49, 0.50 and 0.48. Hence, it is evident that higher strain rates result in substantially higher stresses during the entire deformation process. This is also evident from the cumulative probability plots in Fig. 5.3b, for which we multiplied the normal stress at an

engineering strain of 0.01 with the Schmid factor of the identified slip system in order to obtain the CRSS (*CRSS$_{0.01}$*). The normal stress at 0.01 engineering strain is defined as the intersection of the engineering stress versus strain curve with a line parallel to the unloading slope through the 0.01 engineering strain intercept. The strain rate sensitivity (SRS), defined as $m = \frac{\partial \ln \sigma}{\partial ln\dot{\varepsilon}}$, is obtained by taking a linear fit to the logarithmic plot of the CRSS versus the strain rate $\dot{\varepsilon}$. When we analyze the SRS irrespective of the activated slip system, we find that the value obtained from our 3 µm sized ferrite pillars at 0.01 strain ($m = 0.054 \pm 0.006$, Table 5-1) closely matches the literature values of carburized iron single crystals containing a comparable carbon content of roughly 0.05 wt.% ($m = 0.06$) [185]. Note that the SRS is closely related to carbon content and increases with a decrease in carbon content [185, 186]. The similarities in SRS *m* of our ferrite pillars and literature values suggests similar rate controlling mechanisms of ferrite in DP800 and iron single crystal during deformation [186]. In addition, we observe that the SRS *m* tends to drop during straining slightly, as can be seen from Fig. 5.4 and SRS corresponding to different engineering strains is summarized in as can be seen from Table 5-1.
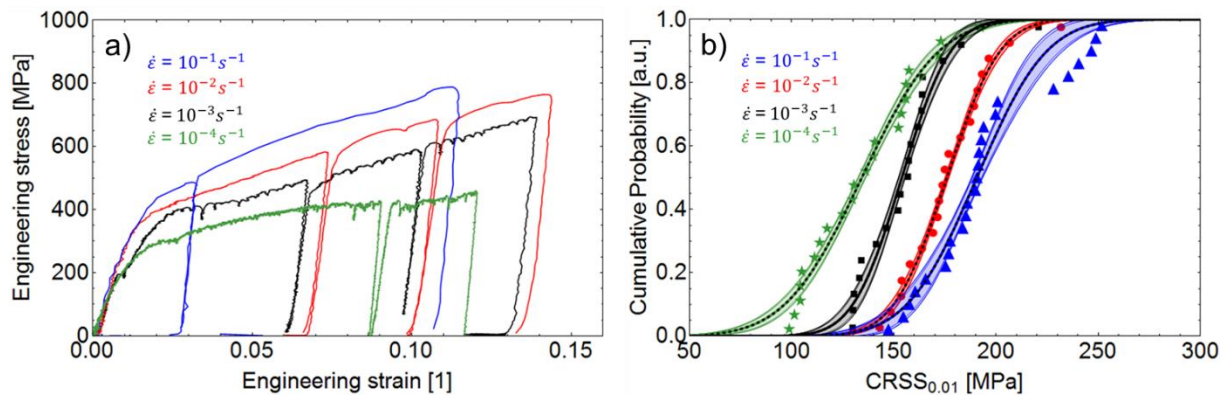
Fig. 5.3 (a) Representative engineering stress versus engineering strain curves recorded at different strain rates. (b) The cumulative probability distribution functions of the CRSS at 0.01 engineering strain (CRSS$_{0.01}$) at different strain rates. A normal distribution is fit to the data including the 90% and 99% confidence intervals. Note that we did not differentiate between activated slip plane families in either of these plots.

Table 5-1 The SRS corresponding to different levels of engineering strain.

Engineering strain (1)	0.01	0.02	0.05	0.1
SRS	0.054 ± 0.006	0.039 ± 0.007	0.038 ± 0.009	0.033 ± 0.016
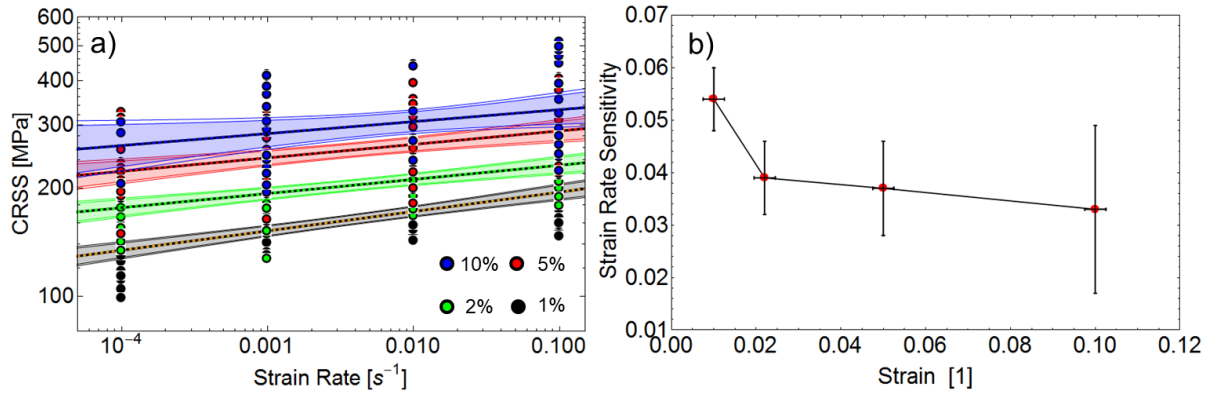
Fig. 5.4 (a) CRSS variation with strain rate taken at different engineering strains. (b) SRS varies with engineering strain.

We introduce the variable χ to investigate the non-Schmid behavior of bcc metals similar to [61, 64]. This orientation parameter describes the angle between the Maximum Resolved Shear Stress Plane (MRSSP) for a specific loading direction and the corresponding {110} plane, which is explained in detail by the standard stereographic projection in Fig. 5.5a. After identifying this orientation parameter for each pillar, the values are correlated to the $CRSS_{0.01}$ values in Fig. 5.5b. The data points at low strain rates are, to a large extent, horizontally distributed, i.e. there is no change of the CRSS with the orientation parameter χ. Upon increasing strain rates, CRSS scatters more and rises by a non-significant amount with χ The color coded slip plane activation is no longer predicted by the closest slip plane family to the MRSSP, which is consistent with the slip trace observation. Furthermore, based on the weak χ dependence of the CRSS in the range of tested strain rates, the SRS m does not notably depend on the orientation.
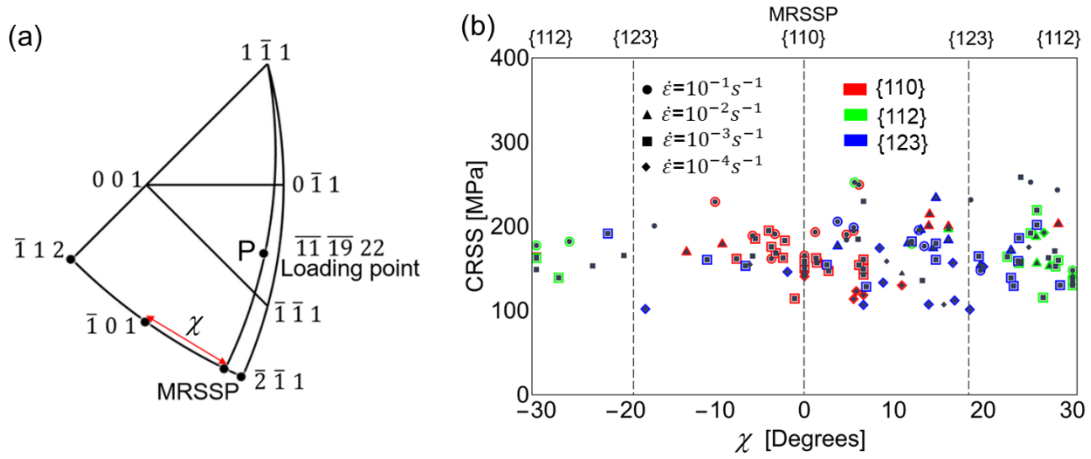
Fig. 5.5 (a) Part of standard stereographic projection showing the definition of the χ angle for one of our pillars. P is the crystallographic loading direction and the great circle going through $(\bar{1}\,1\,2) - (\bar{2}\,\bar{1}\,1)$ represents the projected planes belonging to the $[1\bar{1}1]$ zone axis. The intercept point of this great circle with that passing through $(1\bar{1}1) - P$ defines the Maximum Resolved Shear Stress Plane (*MRSSP*). χ is the angle between *MRSSP* and $(\bar{1}01)$, as shown by the red double-ended arrow. When the intercept stays closer to $(0\bar{1}1) - (\bar{1}\bar{1}1)$ great circle, χ is positive as in this case, otherwise it is negative. (b) CRSS dependence on χ and strain rate. The color code marks the identified slip plane as {110}, {112} or {123}. Pillars where the slip traces were not uniquely identified are not color coded.

From Fig. 5.3b, we deduce not only the SRS but also estimate the activation volume $V = kT * \partial ln\dot{\varepsilon}/\partial\tau$, where k is the Boltzmann constant and T the testing temperature (293K) and τ the CRSS. The activation volume is a common indicator of the rate controlling mechanisms. For instance, 10^1-10^2 b^3 is a typical value for overcoming lattice friction force and 10^2-10^4 b^3 for dislocation-dislocation interactions [93]. At the onset of yield defined at 1% strain we find an activation volume $V = 13$-16 b^3 with the Burgers vector b of pure iron. This activation volume indicates that lattice friction of dislocations might be the rate controlling parameter in our ferrite pillars. The Peierls-Nabarro force – which is the inherent resistance of the crystal lattice against dislocation motion – is the most effective short range obstacle that has to be overcome by an external force under the assistance of thermal activation [93]. With the SRS dropping with strain, the activation volume increases slightly during deformation. The increased flow stress caused by strain hardening is comprised of both thermal and athermal contributions. Predominantly, it is the thermally activated component that reacts most sensitively to strain rate changes, while

the athermal part remains almost constant with strain rate [93, 187, 188]. However, as concluded by Spitzig et al., the athermal stress contribution changes significantly with work hardening, which produces dislocations tangles that act as long range obstacles [189]. On the contrary, the thermal contribution caused by local obstacles, here lattice friction, is insensitive to strain. Consequently, at higher strains the thermal activation of Peierls processes becomes less important, which is reflected by a drop in SRS m, which is also comprised of both thermal and athermal components. This is also the reason why we choose the yielding point for calculation of activation volume.

5.3 Discussion

For bcc it is assumed that dislocation motion is limited by kink pair formation and migration of screw dislocations [90, 190] at temperatures lower than the critical temperature T_c [18, 25], which is 340 K for pure iron [23, 191]. Because of their undefined slip plane, kinks on screw dislocations can extend to any of the {110} planes that are believed to be the elementary slip planes in bcc structures [25, 90, 192]. The observed slip traces of {112} and {123} are comprised of intensive atomistic cross slips between two {110} planes. With increasing strain rates, i.e. increased stress, the kink nucleation rate and migration rate are also increased [190, 193, 194] so that several kinks are likely to be formed on one dislocation line. Kink formation can happen even on different {110} planes, thereby generating a conflict configuration—so-called cross-kinks. Hence, a regular cross slip event on two {110} planes might be interrupted, rendering the dislocations involved immobile. From our data we see an increased tendency for activation of slip systems with lower Schmid factor at high strain rates (see Fig. 5.2a,b), which supports the picture that cross-kink formation shuts down dislocation mobility on planes with higher shear stress, requiring the activation of additional slip systems. The cross-kink formation at higher strain rates, also observed in molecular dynamics simulations, can lead to small loops and debris production [190]. The occurrence of cross-kinks as well as our finding of non-primary slip system activation imply a size scaling of the SRS m in bcc materials, as this cross-kink formation could depend on the dislocation line length. While our 3 µm sized samples show nearly identical SRS m as on the macro scale, if the size of micropillars is further reduced to less than 1 µm, size effects on the SRS are reported (see Huang et al. [23]).

5.4 Conclusion

In summary, we show that the rate controlling process in our 3 µm sized pillars is the Peierl's mechanism, with an activation volume of 13 b^3 to 16 b^3. Within the investigated strain rate

range, all three slip plane families ({110}, {112} and {123}) are active. However, with higher strain rate there is an increasing tendency for activation of slip planes with lower Schmid factor. We attribute this behavior to the formation of cross-kinks resulting in an immobilization of dislocations on the primary slip system. Based on the current data, we do not see a strong orientation dependence of SRS.

6 The fracture toughness of martensite islands in dual phase DP800 steel[4]

6.1 Introduction

In the previous work, the plasticity of ferrite and marensite in dual phase DP800 was investigated [176]. A main issue still raising large research interest is their damage initiation and evolution mechanisms, which mainly arise from the two phases and their huge mechanical heterogeneity. Martensite islands are believed to be one of the most susceptible damage initiation sites primarily recognized by post mortem morphology observation through microscopes [134, 195, 196]. However, a quantitative assessment of their fracture toughness is still pending.

Micromechanical testing became an important tool to locally investigate mechanical properties by extracting the targeted microconstituents [118, 197] with FIB milling. This also applies for fracture properties. Most of the previous small scale fracture mechanical studies focused on brittle materials, in particular thin films or layered structure [122, 198, 199]. Due to the small sample size, the assumptions of the linear elastic fracture models are often not met and small scale EPFM needs to be applied [30, 31, 111]. So far, most materials investigated with small scale EPFM are model materials (e.g. ultrafine grained tungsten or tungsten single crystals), and the application of microscopic EPFM to daily used and industrially produced micro constituent still remains rare.

This work aims at measuring the fracture properties of martensite islands to quantitatively assess the damage initiation of an advanced DP800 steel, corresponding to DP2 in [176].

6.2 Results

6.2.1 Microstructure and chemical composition

The DP steel microstructure is comprised of two phases, namely the matrix ferrite and the dispersed martensite island as shown in Fig. 6.1a. The latter has a much smaller grain (colony) size compared to the former and exhibits irregular shapes (Fig. 6.1b). Further, the colored inverse pole figure (IPF) of an EBSD mapping clearly illustrates that the martensite islands exhibits a complex substructure with subboundaries called packets, blocks and laths. As expected, they are following the K-S orientation relationship with the PAG [44]. Theoretically,

---

[4] This chapter is based on the accepted manuscript: Chunhua Tian, Christoph Kirchlechner. The fracture toughness of martensite islands in dual phase DP800 steel.

24 variants with six in each of four packets should be formed inside one PAG. However, in our case the martensite islands consist typically of one or two packets – which is also common in DP steels [47].
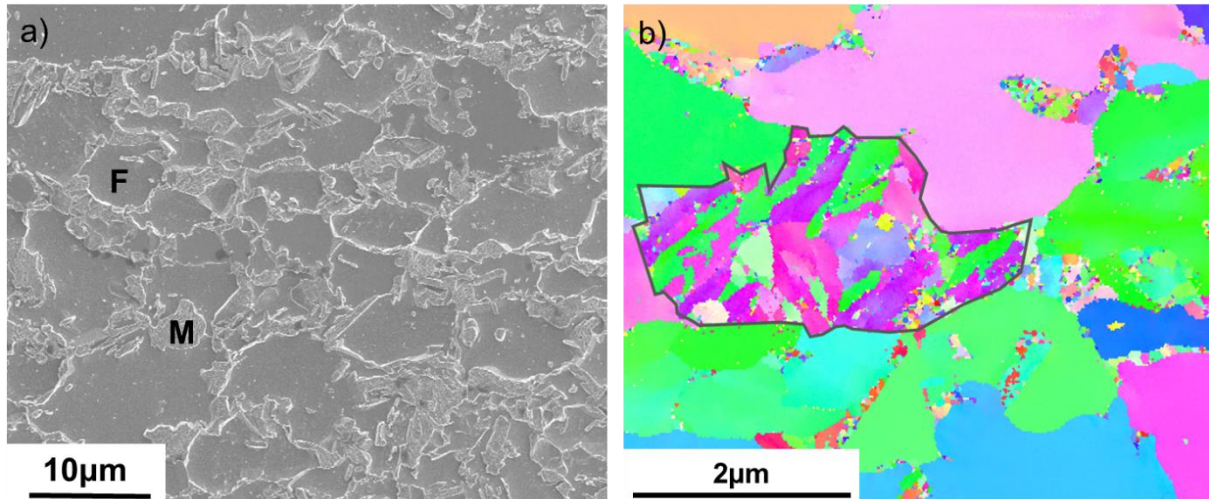
Fig. 6.1 (a) Representative microstructure of DP steel etched by Nital solution, showing ferrite matrix (**F**) and martensite islands (**M**). (b) An IPF of a martensite island, showing the subboundaries. The island is bordered by a black solid line for clarity.

Besides the different variants, the chemical composition is also heterogeneous across the martensite islands. Mn, Cr and Si are predominantly homogeneously distributed in both phases, as can be seen from APT measurements (Fig. 6.2) of an area containing both martensite and ferrite. Along the green cylinder, assume the region belongs to ferrite until the first data point with carbon content larger than 1 at.% C and the rest to martensite. The chemical content of ferrite is 1.90 ± 0.14 at.% Mn, 0.74 ± 0.09 at.% Cr and 0.41 ± 0.08 at.% Si. Here, the error bar is defined as the standard deviation of all data points of ferrite in the cylinder divided by the square root of points' number. Martensite has a comparable content of the three elements, with 2.19 ± 0.20 at.% Mn, 0.97 ± 0.04 at.% Cr and 0.54 ± 0.04 at.% Si. However, a large difference exists for the carbon content. Carbon locates mainly in martensite with 3.77 ± 0.20 at.% while very scarcely in ferrite with only 0.06 ± 0.03 at.% (see Fig. 6.2a and b). It tends to segregate at defects like dislocations, subboundaries, in particular along the phase boundary. No carbides formation is observed in the martensite of this particular DP800, while it is clearly noted that depending on manufacturer and process this can change considerably.
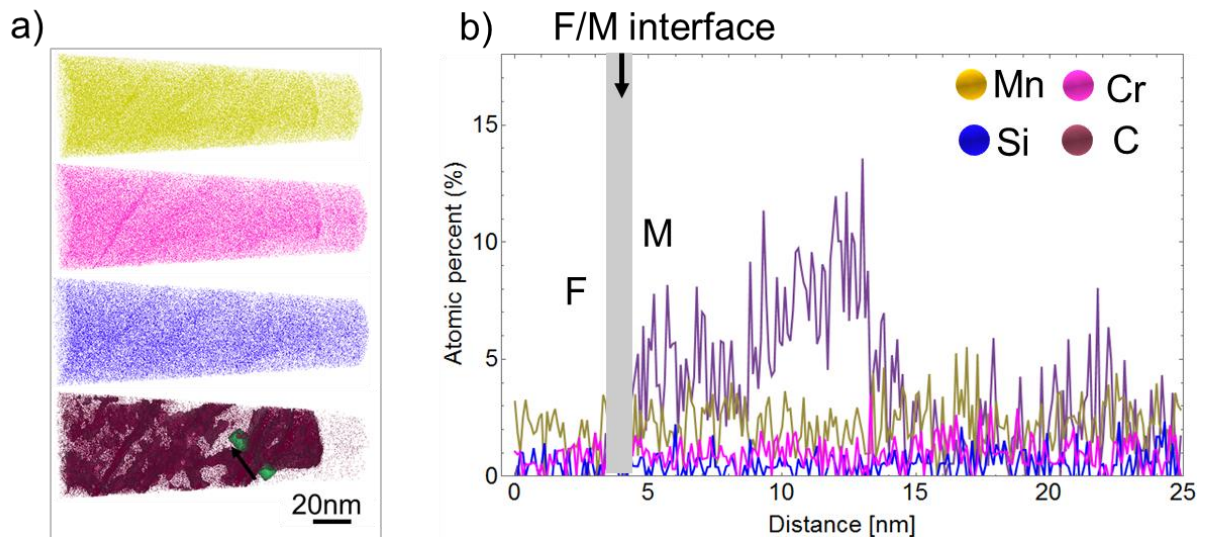
Fig. 6.2 Chemical distribution of Mn, Si, Cr and C in an APT tip containing a ferrite-martensite boundary. (a) Spatial distribution of four main elements Mn, Cr, Si and C. (b) 1-D concentration profile along the green cylinder in (a). Left side is ferrite and right side martensite.

6.2.2 Fracture properties

Fig. 6.3 shows a representative micro cantilever exhibiting fracture of the martensite island and negligible deformation of the softer ferrite. The force initially shows a linear (and elastic) increase, pronounced plasticity and subsequently the force decreases with displacement (Fig. 6.3a). The snapshots in Fig. 6.3c obtained from *in situ* SEM imaging are labelled in the load displacement curve in Fig. 6.3a. The FIB-notch gradually grows to a natural crack exhibiting extensive crack blunting (see Fig. 6.3c.5). Hence, the observed fracture behavior is stable with pronounced ductility near the crack tip. This is consistent with macroscopic observations of lath martensite fracture, which exhibits brittle transgranular cleavage behavior only at low temperature, while it shows a typical dimple ductile fractography at room temperature [200-202]. Massive plastic deformation is evident, for instance by slip trace aligned approximately 45° to the horizontal direction near the crack tip.
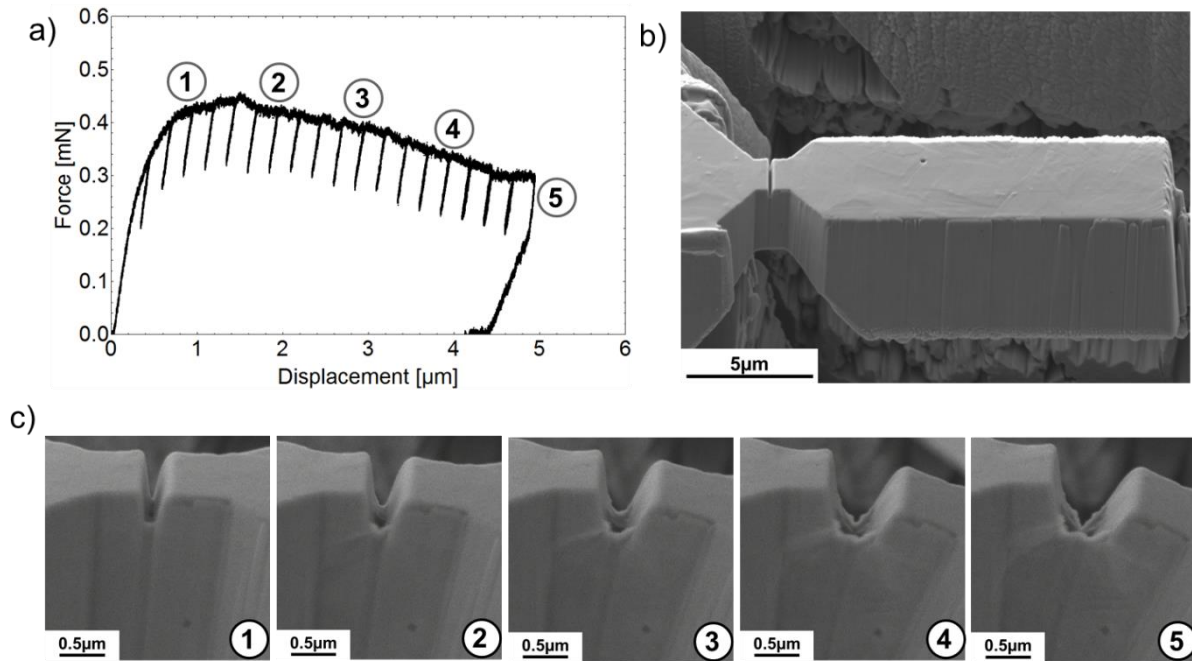
Fig. 6.3 (a) The representative force-displacement curve of a tested sample exhibiting crack growth. (b) The corresponding as milled micro cantilever. (c) Snapshots showing the crack evolution corresponding to unloading states 1 to 5.

In some cases, the plastic deformation of the softer ferrite cannot be neglected anymore. Then, the force-displacement curve (Fig. 6.4) does not show a drop and the unloading stiffness generally remains constant. The notch-tip is blunting but no crack extension is visible in the SEM. Also, a significant amount of plasticity is observed in ferrite close to the clamping end (Fig. 6.4c, arrow).

After carefully screening for ferrite plasticity we discard 25 out of 30 samples because of negligible crack growth but extensive ferrite plasticity, i.e. only in 5 out of 30 cantilevers are further analyzed to assess the fracture toughness of martensite.
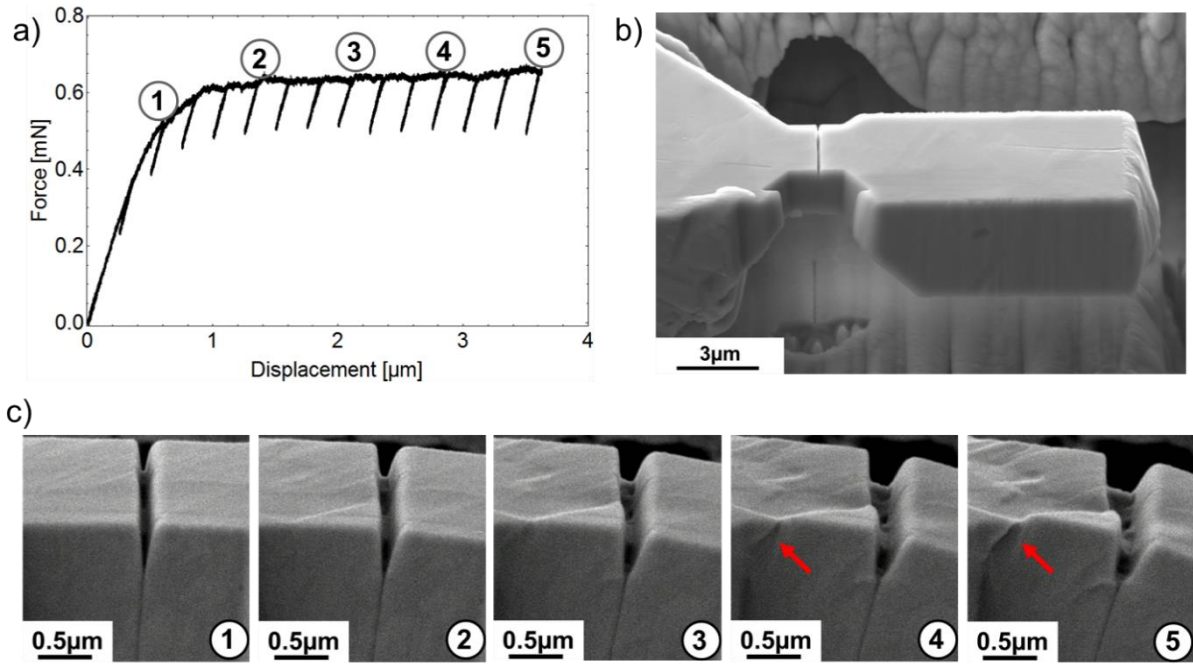
Fig. 6.4 (a) Representative force-displacement curve of a sample exhibiting negligible crack growth in martensite but pronounced ferrite plasticity. (b) The as milled micro cantilever. (c) The snapshots showing the crack evolution corresponding to unloading states 1 to 5.

The crack extension is measured from *in situ* snapshots and plotted versus displacement (see Fig. 6.5a). The red points are the measured crack length at the end of the unloading sequence. The crack extension is fitted by a polynomial fit (black solid line). The crack length remains almost constant to a displacement of ~1 µm, as indicated by the arrow in Fig. 6.5a. Based on the load-displacement data and the crack extension curve, the J-integral was obtained following Eq. (2.11), (2.16)-(2.18)and (3.1), (see crack resistance curve in Fig. 6.5b).
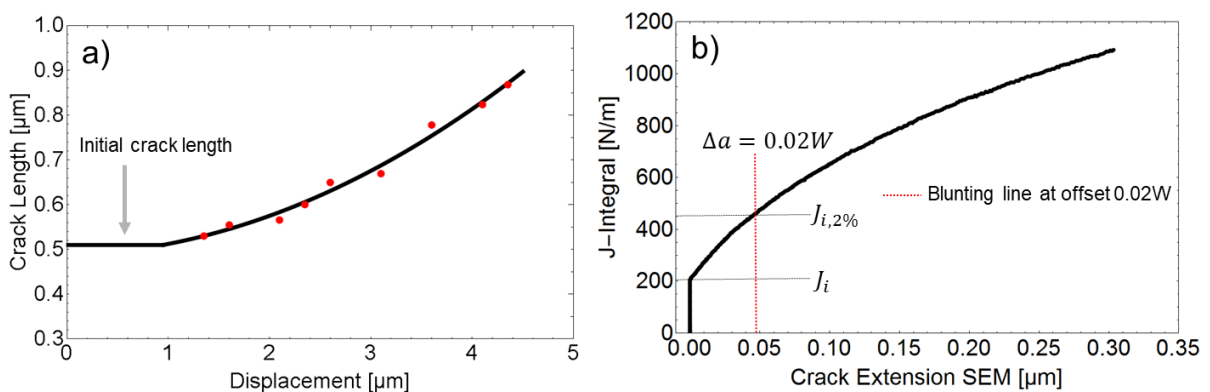
Fig. 6.5 (a) The measured crack evolution versus displacement; (b) a representative *J-R* curve corresponding to the sample in Fig. 6.3. It labels out two approaches of determining the crack initiation toughness.

The R-curve is used to extract the crack initiation toughness J_i (Fig. 6.5b) – which is, by definition, the transition point from crack blunting to crack growth stage and known to be less geometry dependent than the subsequent R-curve [60]. However, an unambiguous identification of the initiation toughness is in most cases not possible. Therefore, we additionally use Pippan´s transfer criterion of the 0.02 W blunting line offset to determine the crack initiation toughness as $J_{i,2\%}$[116, 117]. This transfer criterion can further minimize the influence of polynomial fit degree applied for the crack length versus displacement (see Fig. 6.6). For instance, the $J_{i,2\%}$ determined by 0.02 W transfer criterion equals 359 N/m for a polynomial fit of degree 2 (used in analysis) and 361 N/m for degree 3, respectively. By contrast, the J_i through intersection of fitting line with initial crack length is affected much more, comparing 147 N/m for polynomial fit of degree 2 and 114 N/m for degree 3.
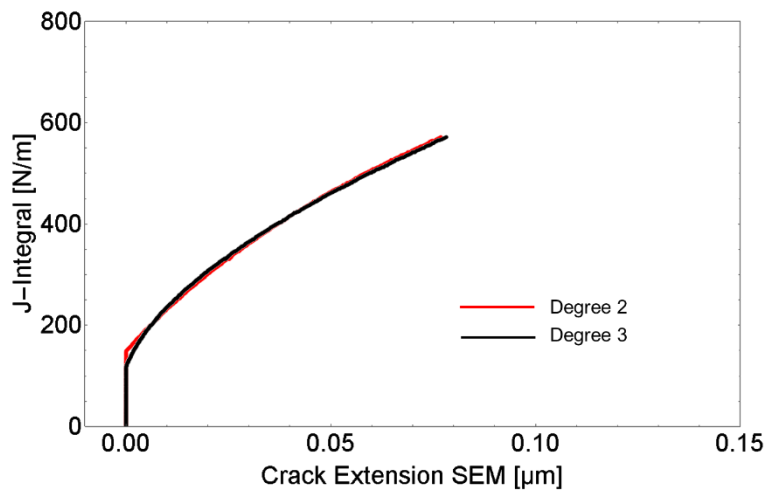
Fig. 6.6 Compare the influence of polynomial fit degree on the determined fracture toughness value.

We summarized all J-R curves of the five successfully tested beams in Fig. 6.7. To a large extent, they coincide with each other. In particular, the crack initiation seems to appear at a similar value for all five cantilevers, and the curve deviates during subsequent crack growth (see Fig. 6.7a and b). Finally, for comparison, we converted the *J*-integral to the stress intensity *K* using Eq. (2.17).
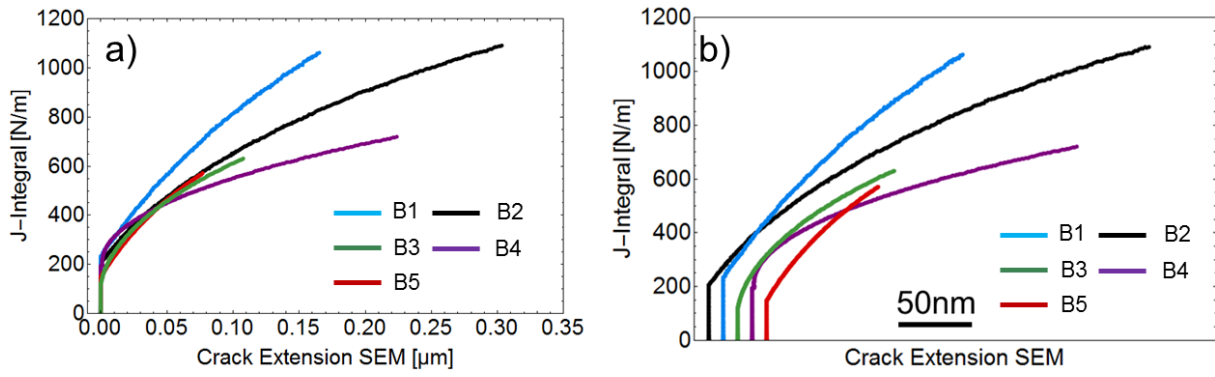
Fig. 6.7 (a) a comparison of *J-R* curves of five successfully tested samples and (b) a better visualization of (a) with shifted *J-R* curves.

Table 6-1 summarizes all five beams including both geometrical dimensions and fracture properties. Note that the a/W ratio for our samples is mainly between 0.2~0.3, smaller than 0.4~0.5 proposed in ASTM 1820. There are two reasons choosing a smaller a/W ratio. First, due to the FIB milling technique a certain limited aspect ratio of milling depth to milling width can be achieved. Already well before this maximum aspect ratio one deviates from a sharp notch. We decided to sacrifice the a/W ratio in order to get sharp notches [31]. Second, the small martensite islands do not allow extensive crack. We try to keep the initial notch small in order to see crack blunting and stable crack growth. It is evident that the crack initiation toughness neither by K_i nor by Pippan´s transfer criterion varies significantly among the five beams. During the remainder of this manuscript, if not specifically pointed out, we discuss and compare only $K_{i,2\%}$, as the discussion would be identically for K_i. On average, the crack initiation toughness of martensite island is $J_{i,2\%} = 423 \pm 22$ J/m^2 and $K_{i,2\%} = 10.1 \pm 0.3$ MPa m$^{1/2}$.

Table 6-1 Summary of five successfully tested beams, including both the geometrical dimensions and fracture property.

	a_0	W	a/W	B	L	L/W	J_i	K_i	$J_{i,2\%}$	$K_{i,2\%}$
* Note: unit of the geometry parameters a_0, W, B, L is all μm and of J is J/m^2 while of K is $MPa.m^{1/2}$.										
B1	0.49	1.84	0.26	1.69	9	5	233.5	7.5	485.8	10.8
B2	0.51	2.30	0.22	1.59	9	4	205.0	7.0	456.8	10.5
B3	0.43	1.86	0.23	1.00	12	6	122.6	5.4	405.9	9.9
B4	0.38	1.73	0.22	1.46	11	6	193.9	6.8	407.7	9.9
B5	0.50	1.47	0.33	1.64	10	6.8	147.4	6.0	358.6	9.3
						Average:	180	6.5	423	10.1
						Standard error:	± 20	± 0.4	± 22	± 0.3

6.3 Discussions

6.3.1 Did we obtain a geometry independent plane strain fracture toughness?

Within this work, we aimed for the fracture toughness of martensite as material property, i.e. as geometry-independent plane-strain critical stress intensity factor K_{IC}. Macroscopically, stringent requirements are listed both in E399 and in E1820 [106, 203] to ensure a plane strain state. For instance, a high-triaxiality region should be considerably larger than the plastic zone size and the ductile tearing section at the two beam edges. The former is mainly guaranteed by the beam thickness, while the latter by beam width according to the definition of our work. To assure plane-strain conditions a critical sample dimension D_{EPFM} (Eq.(6.1)) needs to be present, also for the micron scale [31, 204].

$$D_{EPFM} = 10 \dots 50 \frac{J_{Ic}}{\sigma_y} \tag{6.1}$$

Where J_{Ic} is the critical J integral for *Mode I* fracture and σ_y is the yield strength of the tested material. If we consider the obtained J-integral (423.0 ± 22.1 J/m^2) and the yield strength of martensite islands in our DP800 steel (2880 ± 49 MPa) [176], the critical sample dimension D_{EPFM} ranges from 1.4 ~ 6.8 µm that sets the lower limit of the sample thickness W and width B. As shown in Table 6-1, this condition is not fulfilled. What is obtained here can be rather considered as conditional fracture toughness for this dimension. Unfortunately, due to the limited martensite island size and the considerable large fracture toughness of martensite one

cannot obtain a geometry independent fracture toughness under plane strain conditions in this DP800 steel grade. Still, the results obtained here could be used as an input parameter for modelling damage initiation [205].

6.3.2 Comments on deviation of the crack resistance curve during crack growth

Although the conditional fracture initiation toughness of five beams is consistent with one another, the crack resistance curves deviate with further crack extension. One possible explanation could be the slightly different *a/W* ratio of the investigated cantilevers. The top most curve in Fig. 6.7a was measured on the cantilever with a high *a/W* ratio, in other words, shorter left ligament. While the crack initiation is less influenced by the ligament length, the crack resistance curve depends strongly on initial crack depth at macroscopic investigations [206, 207]. However, this trend was recently not observed at the micrometer length scale [31], where shorter ligaments lead to higher crack resistance.

Hence, the more likely explanation of the strong variation in crack resistance curve is the strong variation of microstructure in the 5 tested beams: Neither the number of probed variants nor the orientation of the martensite island is identical for all the samples. While the influence of the local microstructure seems to be negligible for crack initiation, crack growth is obviously significantly influenced by the hierarchical microstructure of the martensite.

Another factor that might lead to the deviation of crack growth resistance curve is the roughness of the crack front due to the heterogenous microstructure in the martensite island, as shown in Fig. 6.8. The data was obtained by FIB serial sectioning of the tested cantilever. In Fig. 6.8, the crack length exhibits a minimum length of 717 nm and a maximum length of 974 nm. In the *in situ* SEM micrographs, the crack length was measured at the front face of the cantilevers and is 840 nm. It is expected and well-known from literature [31], that the variation of the crack length at crack initiation is smaller compared to the region showing pronounced crack growth (Fig.

6.8). Hence, the crack front roughness has a larger influence on the R-curve behavior than on the crack initiation toughness value.
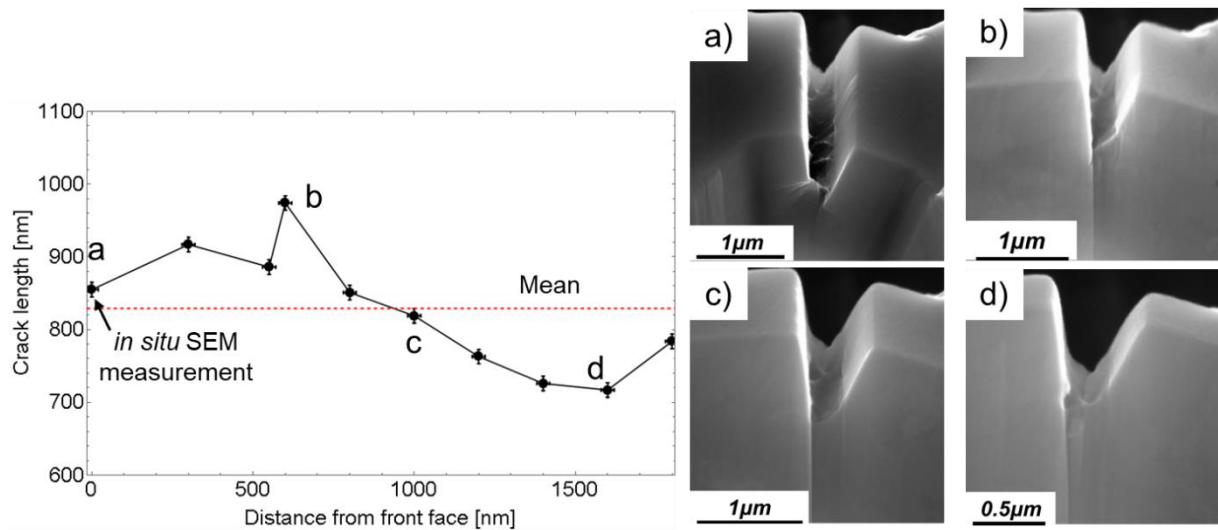
Fig. 6.8 Crack propagation across the cantilever measured via serial sectioning (left). Corresponding SEM images as marked in the graph (a-d). The error bar is given based on ten times' measurement of one crack in depth direction and in width's direction. They have a standard error of the mean in the order 10nm and 20nm, respectively.

6.3.3   Comparison with other Fe-based materials

The obtained fracture toughness of DP800 martensite islands is substantially lower than that of tested bulk martensite (can reach dozens of MPa. $m^{1/2}$) which has a similar carbon content but much larger substructure size [202, 208].

Recently, the toughness of different steels at the micron scale including white etching layers – which might be similar to martensite in terms of carbon supersaturation, but not in terms of microstructure – was correlated with the hardness via an empirical equation $K_Q = \frac{10^4}{HV}$, where HV is the Vickers hardness [116]. The Vickers hardness of martensite was statistically reported following $H_V = 0.4(\sigma_Y - 100)$ [209]. In this empirical way, the estimated fracture toughness K_{IQ} is 8.8 ~ 9.2 MPa.$m^{1/2}$, which is close to our experimental results of 10.1 ± 0.3 MPa.$m^{1/2}$. Hence, the martensite in DP800 follows the expected trend for steels.

Unravelling the reason for the observed toughness is more complicated and only a brief speculation is presented here. The carbon content of martensite and its distribution plays a critical role in the fracture toughness of Fe-based alloys [210, 211]). Supersaturated carbon has an adverse effect on fracture toughness, such as in severely deformed pearlite. The lamellar shape cementite in pearlitic steels is dissolved into the ferrite matrix upon severe plastic deformation (e.g. wire drawing), reducing strain hardening ability of soft ferrite. This partly results in an inferior fracture toughness [210, 211]. The nominal carbon content in our material (0.13 wt. %) is much lower than that in the pearlitic rail steel (0.72 wt. %) where WELs are formed [110, 116]. However, in our case almost the entire carbon is present in the martensite (see Fig. 6.2) with an average amount similar to carbon content of 3 at. % present in WELs [110]. Besides, both show a heterogeneous distribution of carbon segregating at defects like dislocations and boundaries. No obvious carbides are formed in both cases, which are believed to play a critical role in microcrack or microvoid initiation and deteriorate fracture toughness [200]. Hence, carbon should not be the key reason inducing more brittleness of martensite islands compared with WELs.

Another important factor is the grain size of the two microstructures. For lath martensite, containing abundant substructures as in our case, block boundaries act as the most efficient obstacles for dislocation motion [48, 212]. The block size is in the order of 100 nm in our sample, substantially finer than the one in literatures [110, 202], which strongly impedes dislocation motion in martensite islands and deteriorates ductility. In addition, grains of martensite in WELs exhibit almost equiaxed morphology, while martensite islands in DP steels have a hierarchical structure with lath, blocks and packets arranging themselves complying with orientation of the PAG. This kind of structural ordering might be very detrimental for toughness. A significantly lower fracture toughness (5 $MPa.m^{1/2}$) of nanostructured pearlitic steels was reported when the loading direction is in parallel with lamellar microstructures. By contrast, under a perpendicular loading, fracture toughness up to 40 $MPa.m^{1/2}$ was found [213].

6.3.4 Damage initiation at martensite islands in DP steels

The low toughness of martensite islands, as quantitatively proven by the micro cantilever bending test, is responsible for the crack nucleation in martensite. This was also shown by *in situ* macroscopic tensile testing on the same DP steel combined with machine learning to statistically identify the main damage initiation sites [195]. Martensite cracking at lower strain

was also found by Calcagnotto et al. [214], where a coarse grained DP steel grade showed cleavage fractography.

Based on the measured initiation fracture toughness value, we can estimate the critical defect size for crack initiation according to the Eq. (6.2) [60],

$$K_i = Y\sqrt{\pi a_{critical}}\sigma_y \tag{6.2}$$

Here, Y is dimensionless geometrical factor, varying with different geometries and σ_y is the yield strength 2880 MPa. Assuming that we have a penny shape crack with Y as $2/\pi$, the estimated critical defect size is approximately 4 µm. Note that for a more conservative value, we take the smaller K_i instead of $K_{i,2\%}$ to calculate. As the critical defect size is larger than the mean martensite island size, it is suggested that most isolated martensite islands would rather deform plastically than initiate a crack. However, large martensite islands or a banded martensite structure are sufficiently large to show crack initiation. This observation is in agreement with [215, 216], showing that crack initiation is preferably found at martensite bands or closely agglomerating martensite regions. Having said that, it is clear that a damage tolerance of DP steels can only be obtained by avoiding a banded microstructure.

6.4 Conclusion

We investigated the fracture behavior of martensite islands in DP800 steel and can conclude:

- Our martensite islands have a hierarchical substructure. Most of the carbon is located at substructure boundaries.
- Due to the small martensite we often provoke plastic deformation of surrounding ferrite, which renders the measurement of crack initiation and growth challenging. Only 5 out of 30 samples showed negligible plasticity in ferrite.
- The martensite islands in our DP800 steel are semi-brittle, possessing a conditional fracture initiation toughness $J_{i,2\%} = 423 \pm 22$ J/m^2 and $K_{i,2\%} = 10.1 \pm 0.3$ MPa m$^{1/2}$.
- The estimated critical defect size shows that damage initiation can happen either in very large martensite islands or in agglomerated or even banded martensite.

7 Summary and outlook

7.1 Summary

The present work focused on the understanding of damage behaviors in DP800 steels from the perspective of micromechanics. All micro specimens were fabricated by FIB milling. We first performed pillar compression tests for plasticity investigation of two phase components, ferrite and martensite, through which the activated slip systems of ferrite were identified and CRSS of each slip plane family was quantitatively determined, along with consideration of the well-known size effect, steel grade and SRS. For martensite, compressive yield strength instead of CRSS, due to the limitation of small colony size, was acquired and the role of substructures typical in lath martensite was briefly investigated. In addition to pillar compression, micro cantilever bending tests were also conducted to extract fracture toughness in load mode I of martensite islands that were found to be the predominant crack initiation sites in our DP steels. Moreover, focus was not only put on micromechanical testing, but also on microstructural characterization such as grain size by SEM/EBSD, dislocation density by ECCI and chemical elements by APT, which further facilitates us understanding the obtained micromechanical properties. On the basis of our present work, light is shed on the following aspects.

Slip system activation and CRSS in ferrite

Controversy always exists concerning the activated slip systems in bcc structures. Thanks to the simple uniaxial loading state, pillar compression evolves to be an appropriate effective tool for tackling this controversial issue. By comparing the SEM observed slip pattern and the imposed theoretical slip trace through considering pillar orientation, our results show that three slip plane families $\{110\}$, $\{112\}$ and $\{123\}$ are all activated in ferrite of our DP800 steels. The activation of slip systems, in most cases, is guided by their corresponding Schmid factor and hence, follows Schmid's law. The three slip families have a nearly identical CRSS value, specifically 147 ± 6, 143 ± 9 and 146 ± 4 MPa of 3 μm sized pillars, respectively. We attribute the identical CRSS to the effective elementary slip plane as $\{110\}$ as put forward by Caillard through TEM investigation [25]. The activation of 48 slip systems in ferrite grains enables a good shape accommodation at the phase boundaries and reduces the chance of boundary discontinuity acting as damage initiation sites as supported by our partners.

Strength (CRSS) of ferrite exhibits a non-negligible size effect which is currently elucidated by the dislocation density gradient across from ferrite grain interior to the phase boundary. The

ECCI images clearly show a higher dislocation density near ferrite martensite phase boundary resulted from volume expansion of austenite phase transformation. In addition to size scaling, strain rate is also an important factor influencing strength of ferrite. The CRSS increases from 135 ± 6 MPa at a strain rate of 10^{-4} s^{-1} to 195 ± 6 MPa at 10^{-1} s^{-1}, resulting in a SRS of 0.054 ± 0.006 and an activation volume $13b^3$ to $16b^3$ which is an appropriate indicator for identifying the rate controlling process during plastic deformation of ferrite. Such a small activation volume indicates Peierls process dominates ferrite deformation. Furthermore, with an increase in strain rate, an increasing tendency of non-Schmid slip activation is observed. By comparing ferrite in two DP800 steels sharing identical UTS, we arrive at a significant difference of ferrite strength. One possible explanation we propose for the moment is the different dislocation density. Further experiments, however, are required to have a more comprehensive understanding of this point.

Plasticity of martensite islands

Limited by martensite islands' size, we milled pillars comprised of all substructures not differentiating their orientations. Pillars of martensite islands yield at a much higher strength (nearly 3000 MPa) compared with that of ferrite, which is credited to the abundant sub boundaries and tangles of dislocations. Those sub boundaries are introduced by different transformed variants from one PAG following the K-S orientation relationship. Not all 24 variants occur in one martensite island. Instead of slip traces on compressed martensite pillars, we observe sub boundary sliding that plays the leading role in plasticity of martensite islands. Besides, difference is also found in martensite strength of two DPs. From the APT element analysis, we see a distinguished carbon distribution. Martensite islands in both steels grades are rich in carbon, but one is in a solid solution state while the other forms bulk carbide form, along block boundaries. Therefore, with carbide formation, solid solution hardening effect of carbon is accordingly weakened and leads to a lower compressive yield strength of martensite islands in one DP steel.

Fracture toughness of martensite islands

If, as enlightened by linking micro and macroscopic mechanical properties, plasticity of two phases and their mechanical heterogeneity is mainly responsible for damage initiation, what matters afterwards is then fracture resistance of initiated damage sites. In our DP800 steels, the predominant damage initiation sites are martensite colonies as reported by our cooperators [195]. Further, according to the cracks' orientation distribution with respect to the principle

tensile direction, the fracture of martensite is dominated by fracture mode *I*. Through micro cantilever bending tests, we did not observe an ideally brittle fracture. Instead, cracks propagate elastic-plastically. Plasticity of martensite islands increases the fracture resistance and the estimated conditional fracture initiation toughness is K_i=6.5 ± 0.4 MPa.m$^{0.5}$ extracted by definition and K_i=10.1 ± 0.3 MPa.m$^{0.5}$ by Pippan's 2% width criterion for microscale fracture tests. The captured fracture toughness can further provide insights on the critical defect size. By assuming a penny shape and a load of yield stress, we arrive at a critical crack size of approximately 4 μm, at which the crack begins to grow. It implies that by reducing the martensite colony size, the potential of martensite acting as fracture initiation site can be decreased, which further contributes to toughness of DP steels.

7.2 Outlook

Although this work, mainly based on micromechanical tests, provides a further understanding of damage initiation behaviors in DP steels, still there are issues remaining unclear or incomplete.

We found the slip plane activation of {110}, {112} and {123} families under our specific conditions such as room temperature and relatively low strain rates (10^{-4} to 10^{-1} s^{-1}). However, during the forming process, high temperature and high strain rates are frequently required. Do these parameters also influence slip system activation? Although we made efforts to study the influence of strain rates on slip plane family activation, improvement could be made if pillars were milled from one large single grain orientated for preferred slip plane so that repetivity was further enhanced. Besides, it could also be possible to extract the SRS of each slip plane family due to a larger data volume. By comparing ferrite strength in two DP800 steels, a big difference exists, which is, for the moment, mainly rather qualitatively attributed to a various dislocation density in two ferrite types. It is not yet quantitatively verified. One possible approach is to testify the strength convergence of the two ferrite after severe prestraining.

We tested fracture initiation toughness of martensite islands in one DP800 steel, since, on the basis of collaborators' findings, they are the predominant damage initiation sites [195]. In this respect, there are at least two issues that can be further polished. As lath martensite is comprised of complex substructures, full of different subboundaries, one could have a second thought on the most sensitive boundary (sub/block, packet, prior austenite) to damage initiation and the specific fracture initiation toughness. Further, in our DP800 steel, martensite acts as the predominant damage initiation. However, phase boundary is also reported as frequent damage

initiation sites. It might also be worthwhile to find out if a limit value of mechanical heterogeneity exists determining the main damage initiators. Besides, through the APT analysis, carbon in martensite can exist either in solid solution or as carbides. Whether this influences fracture initiation toughness or even fracture mechanism (ductile fracture/cleavage fracture), still remains unknown, since we, limited by time constraints, only tested martensite islands in one DP grade.

At this stage, we are primarily engaged in investigating damage initiation behaviors of DP steels at microscale. However, to design a damage tolerant component, what matters also is the consecutive damage growth process, on which our current results already shed light. Through observation of the fracture cross sections, a significantly larger amount of damage initiation sites is found in one DP steel, which, however, exhibits a notably longer uniform and fracture elongation compared with the other. We ascribe the higher tendency of damage initiation mainly to the larger mechanical heterogeneity of two phase components, while the superior elongation, by hypothesis, is probably closely related with the higher work hardening potential of softer ferrite in this DP steel grade. In regard to work hardening potential of ferrite in two DPs, we already have some preliminary results. Pillar compression, though as a good tool for isolating targeted features, is not appropriate for investigating work hardening. Therefore, prestraining of DP steels by uniaxial tensile testing was first performed and pillars were milled on these prestrained samples. The current results shown in Fig. 7.1, in the first place, support our hypothesis. With a prestrain of roughly 20%, the initial softer ferrite hardens significantly more than the initially harder one. As preliminarily demonstrated, work hardening of ferrite does play an important role in suppressing damage growth, such as growth of initiated cracks in martensite. Therefore, of great interest in the future is a detailed investigation on ferrite isotropic and anisotropic hardening behavior. For the isotropic hardening, a material model can be brought forward, describing CRSS as a function of pillar size, strain rate and deformed strain forward. For the anisotropic hardening, CRSS of ferrite can be correlated with dislocation density on each possible slip plane (latent hardening). When the deformation mechanism of two phases can be comprehensively understood and quantitatively described by physical based models, it is promising to design DP steels with desired yield strength, ultimate strength combined with excellent uniform, fracture elongation.
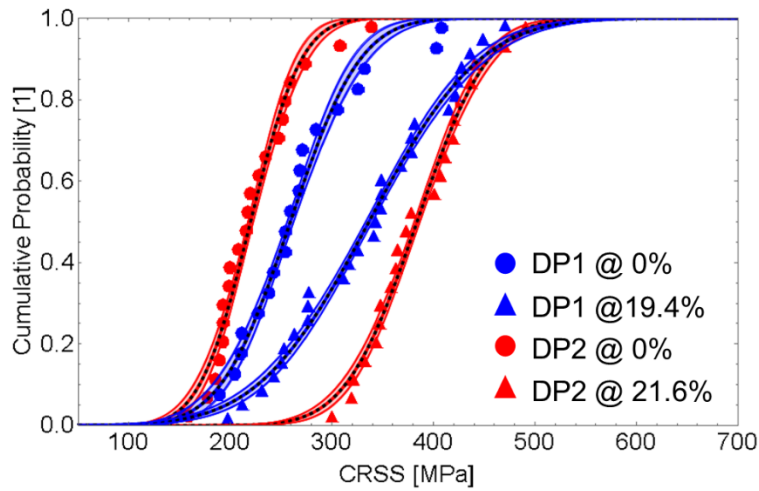
Fig. 7.1 Comparing the CRSS change of ferrite in two DPs, with a prestrain of approximately 20%. CRSS was calculated at 1% engineering strain.

8 Appendix I: FEM for geometry factor of tested beam shape

Since, compared with the standard regular one, a special beam shape with a neck was adopted in our micro cantilever bending tests, we performed a simple FEM in Abaqus 6.14 to check the geometry factor function with dimensions.

The Young's modulus is set as 210 GPa and Poisson's ratio as 0.3. The mesh type is assigned as quadratic brick. For the determination of the relationship between stress intensity factor and crack length, all other parameters except the initial assigned crack length, remain constant including geometry dimensions, boundary condition, load magnitude and crack position, as illustrated in Fig. 8.1a. The results show that there is no significant difference concerning geometry factor of the two beam types. Hence, during calculating fracture toughness of martensite islands, we simply use Matoy's equation Eq.(3.1).
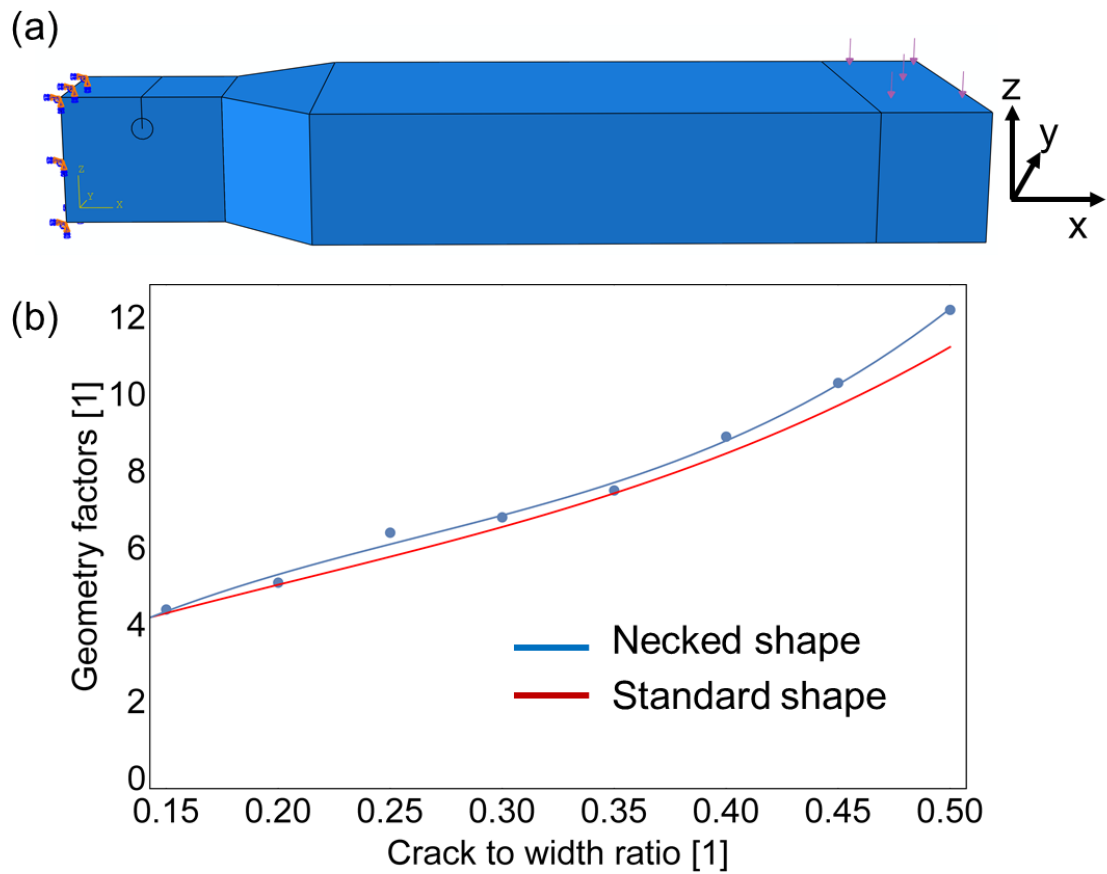
Fig. 8.1 (a) an beam example showing the boundary conditions and loading position; (b) Comparison of geometry factor in two types of beam shape, blue representing necked and red standard.

List of figures

List of tables

Reference

[1] J. Dargay, D. Gately, M. Sommer, Vehicle ownership and income growth, worldwide: 1960-2030, The energy journal 28(4) (2007) 143-170.

[2] A. Mayyas, A. Qattawi, M. Omar, D. Shan, Design for sustainability in automotive industry: A comprehensive review, Renewable and sustainable energy reviews 16(4) (2012) 1845-1862.

[3] C.C. Tasan, M. Diehl, D. Yan, M. Bechtold, F. Roters, L. Schemmann, C. Zheng, N. Peranio, D. Ponge, M. Koyama, An overview of dual-phase steels: advances in microstructure-oriented processing and micromechanically guided design, Annual Review of Materials Research 45 (2015) 391-431.

[4] N. Fonstein, Dual-phase steels, Automotive Steels, Elsevier2017, pp. 169-216.

[5] M. Rashid, Dual phase steels, Annu. Rev. Mater. Sci. 11(1) (1981) 245-266.

[6] H. Ghadbeigi, C. Pinna, S. Celotto, Failure mechanisms in DP600 steel: Initiation, evolution and fracture, Mater. Sci. Eng., A 588 (2013) 420-431.

[7] E. Ahmad, T. Manzoor, K.L. Ali, J. Akhter, Effect of microvoid formation on the tensile properties of dual-phase steel, J. Mater. Eng. Perform. 9(3) (2000) 306-310.

[8] J. Kadkhodapour, A. Butz, S.Z. Rad, Mechanisms of void formation during tensile testing in a commercial, dual-phase steel, Acta Mater. 59(7) (2011) 2575-2588.

[9] M. Erdogan, The effect of new ferrite content on the tensile fracture behaviour of dual phase steels, J. Mater. Sci. 37(17) (2002) 3623-3630.

[10] M. Calcagnotto, Y. Adachi, D. Ponge, D. Raabe, Deformation and fracture mechanisms in fine- and ultrafine-grained ferrite/martensite dual-phase steels and the effect of aging, Acta Mater. 59(2) (2011) 658-670.

[11] L. Schemmann, S. Zaefferer, D. Raabe, F. Friedel, D. Mattissen, Alloying effects on microstructure formation of dual phase steels, Acta Mater. 95 (2015) 386-398.

[12] C. Peng-Heng, A. Preban, The effect of ferrite grain size and martensite volume fraction on the tensile properties of dual phase steel, Acta Metall. 33(5) (1985) 897-903.

[13] E. Maire, O. Bouaziz, M. Di Michiel, C. Verdu, Initiation and growth of damage in a dual-phase steel observed by X-ray microtomography, Acta Mater. 56(18) (2008) 4954-4964.

[14] D. Di Maio, S. Roberts, Measuring fracture toughness of coatings using focused-ion-beam-machined microbeams, J. Mater. Res. 20(2) (2005) 299-302.

[15] N.V. Malyar, J.S. Micha, G. Dehm, C. Kirchlechner, Size effect in bi-crystalline micropillars with a penetrable high angle grain boundary, Acta Mater. 129 (2017) 312-320.

[16] J.R. Greer, W.C. Oliver, W.D. Nix, Size dependence of mechanical properties of gold at the micron scale in the absence of strain gradients, Acta Mater. 53(6) (2005) 1821-1830.

[17] T. Bieler, P. Eisenlohr, F. Roters, D. Kumar, D. Mason, M. Crimp, D. Raabe, The role of heterogeneous deformation on damage nucleation at grain boundaries in single phase metals, Int. J. Plast. 25(9) (2009) 1655-1683.

[18] C.R. Weinberger, B.L. Boyce, C.C. Battaile, Slip planes in bcc transition metals, Int. Mater. Rev. 58(5) (2013) 296-314.

[19] W. Spitzig, A. Keh, Orientation and temperature dependence of slip in iron single crystals, Metall. Trans. 1(10) (1970) 2751.

[20] K.I.V. Vitek, Atomistic study of non-Schmid effects in the plastic yielding of bcc metals, Philos. Mag. A 81(5) (2001) 1387-1407.

[21] R. Gröger, V. Vitek, Breakdown of the Schmid Law in BCC Molybdenum Related to the Effect of Shear Stress Perpendicular to the Slip Direction, Mater. Sci. Forum 482 (2005) 123-126.

[22] Q. Zhou, J. Zhao, J. Xie, F. Wang, P. Huang, T. Lu, K. Xu, Grain size dependent strain rate sensitivity in nanocrystalline body-centered cubic metal thin films, Mater. Sci. Eng., A 608 (2014) 184-189.

[23] R. Huang, Q.-J. Li, Z.-J. Wang, L. Huang, J. Li, E. Ma, Z.-W. Shan, Flow stress in submicron BCC iron single crystals: sample-size-dependent strain-rate sensitivity and rate-dependent size strengthening, Mater. Res. 3(3) (2015) 121-127.

[24] V. Vitek †, Core structure of screw dislocations in body-centred cubic metals: relation to symmetry and interatomic bonding, Philos. Mag. 84(3-5) (2004) 415-428.

[25] D. Caillard, Kinetics of dislocations in pure Fe. Part I. In situ straining experiments at room temperature, Acta Mater. 58(9) (2010) 3493-3503.

[26] D. Caillard, Kinetics of dislocations in pure Fe. Part II. In situ straining experiments at low temperature, Acta Mater. 58(9) (2010) 3504-3515.

[27] M. Ashby, The deformation of plastically non-homogeneous materials, The Philosophical Magazine: A Journal of Theoretical Experimental and Applied Physics 21(170) (1970) 399-424.

[28] M. Mazinani, W. Poole, Effect of martensite plasticity on the deformation behavior of a low-carbon dual-phase steel, Metallurgical and materials transactions A 38(2) (2007) 328-339.

[29] C. Du, J. Hoefnagels, R. Vaes, M. Geers, Plasticity of lath martensite by sliding of substructure boundaries, Scripta Mater. 120 (2016) 37-40.

[30] S. Wurster, C. Motz, R. Pippan, Characterization of the fracture toughness of micro-sized tungsten single crystal notched specimens, Philos. Mag. 92(14) (2012) 1803-1825.

[31] A.K. Saxena, S. Brinckmann, B. Völker, G. Dehm, C. Kirchlechner, Experimental conditions affecting the measured fracture toughness at the microscale: Notch geometry and crack extension measurement, Materials & Design 191 (2020) 108582.

[32] R. Kuziak, R. Kawalla, S. Waengler, Advanced high strength steels for automotive industry, Archives of civil and mechanical engineering 8(2) (2008) 103-117.

[33] S. Gündüz, Effect of chemical composition, martensite volume fraction and tempering on tensile behaviour of dual phase steels, Mater. Lett. 63(27) (2009) 2381-2383.

[34] T. Sakaki, K. Sugimoto, T. Fukuzato, Role of internal stress for continuous yielding of dual-phase steels, Acta Metall. 31(10) (1983) 1737-1746.

[35] T. Hilditch, T. de Souza, P. Hodgson, Properties and automotive applications of advanced high-strength steels (AHSS), Welding and Joining of Advanced High Strength Steels (AHSS), Elsevier 2015, pp. 9-28.

[36] X. Zuo, Y. Chen, M. Wang, Study on microstructures and work hardening behavior of ferrite-martensite dual-phase steels with high-content martensite, Materials Research 15(6) (2012) 915-921.

[37] M. Calcagnotto, D. Ponge, D. Raabe, Effect of grain refinement to 1 μm on strength and toughness of dual-phase steels, Mater. Sci. Eng., A 527(29-30) (2010) 7832-7840.

[38] M. Calcagnotto, D. Ponge, D. Raabe, On the effect of manganese on grain size stability and hardenability in ultrafine-grained ferrite/martensite dual-phase steels, Metallurgical and Materials Transactions A 43(1) (2012) 37-46.

[39] P. Movahed, S. Kolahgar, S. Marashi, M. Pouranvari, N. Parvin, The effect of intercritical heat treatment temperature on the tensile properties and work hardening behavior of ferrite–martensite dual phase steel sheets, Mater. Sci. Eng., A 518(1-2) (2009) 1-6.

[40] R. Davies, Influence of martensite composition and content on the properties of dual phase steels, Metall. Trans. A 9(5) (1978) 671-679.

[41] S. Hansen, R. Pradhan, Structure--Property Relationships and Continuous Yielding Behavior in Dual-Phase Steels, Fundamentals of dual-phase steels (1981) 113-144.

[42] A. Kumar, S.B. Singh, K. Ray, Influence of bainite/martensite-content on the tensile properties of low carbon dual-phase steels, Mater. Sci. Eng., A 474(1-2) (2008) 270-282.

[43] A. Bag, K. Ray, E. Dwarakadasa, Influence of martensite content and morphology on tensile and impact properties of high-martensite dual-phase steels, Metallurgical and Materials Transactions A 30(5) (1999) 1193-1202.

[44] S. Morito, H. Tanaka, R. Konishi, T. Furuhara, Maki, The morphology and crystallography of lath martensite in Fe-C alloys, Acta Mater. 51(6) (2003) 1789-1799.

[45] H. Kitahara, R. Ueji, N. Tsuji, Y. Minamino, Crystallographic features of lath martensite in low-carbon steel, Acta Mater. 54(5) (2006) 1279-1288.

[46] A. Stormvinter, P. Hedström, A. Borgenstam, Investigation of lath and plate martensite in a carbon steel, Solid state phenomena, Trans Tech Publ, 2011, pp. 61-66.

[47] C. Du, J. Hoefnagels, S. Kölling, M. Geers, J. Sietsma, R. Petrov, V. Bliznuk, P. Koenraad, D. Schryvers, B. Amin-Ahmadi, Martensite crystallography and chemistry in dual phase and fully martensitic steels, Mater. Charact. 139 (2018) 411-420.

[48] S. Morito, H. Yoshida, T. Maki, X. Huang, Effect of block size on the strength of lath martensite in low carbon steels, Mater. Sci. Eng., A 438 (2006) 237-240.

[49] G. Gottstein, Physical foundations of materials science, Springer Science & Business Media 2013.

[50] L. Morsdorf, O. Jeannin, D. Barbier, M. Mitsuhara, D. Raabe, C.C. Tasan, Multiple mechanisms of lath martensite plasticity, Acta Mater. 121 (2016) 202-214.

[51] C. Du, R. Petrov, M. Geers, J. Hoefnagels, Lath martensite plasticity enabled by apparent sliding of substructure boundaries, Materials & Design 172 (2019) 107646.

[52] M. Abbasi, T.W. Nelson, C.D. Sorensen, L. Wei, An approach to prior austenite reconstruction, Mater. Charact. 66 (2012) 1-8.

[53] N.J. Kim, A.H. Nakagawa, Effective grain size of dual-phase steel, Mater.Sci. 83(1) (1986) 145-149.

[54] N. Kim, G. Thomas, Effects of morphology on the mechanical behavior of a dual phase Fe/2Si/0.1 C steel, Metall. Trans. A 12(3) (1981) 483-489.

[55] F.G. Caballero, A. Garcia-Junceda, C. Capdevila, C.G. de Andrés, Evolution of microstructural banding during the manufacturing process of dual phase steels, Materials transactions 47(9) (2006) 2269-2276.

[56] S.W. Thompson, P. Howell, Factors influencing ferrite/pearlite banding and origin of large pearlite nodules in a hypoeutectoid plate steel, Mater. Sci. Technol. 8(9) (1992) 777-784.

[57] W. Bleck, Material science of steel, Department of Ferrous Metallurgy, RWTH Aachen University (2007).

[58] P. Uggowitzer, H.P. Stüwe, The tensile fracture of ferritic-martensitic carbon steels, Mater.Sci. 55(2) (1982) 181-189.

[59] T. Kunio, M. Shimizu, K. Yamada, H. Suzuki, An effect of the second phase morphology on the tensile fracture characteristics of carbon steels, Eng. Fract. Mech. 7(3) (1975) 411-417.

[60] T.L. Anderson, Fracture mechanics: fundamentals and applications, CRC press 2017.

[61] K. Ito, V. Vitek, Atomistic study of non-Schmid effects in the plastic yielding of bcc metals, Philos. Mag. A 81(5) (2001) 1387-1407.

[62] R. Gröger, V. Vitek, Breakdown of the Schmid law in bcc molybdenum related to the effect of shear stress perpendicular to the slip direction, Mater. Sci. Forum, Trans Tech Publ, 2005, pp. 123-126.

[63] J.-Y. Kim, D. Jang, J.R. Greer, Crystallographic orientation and size dependence of tension–compression asymmetry in molybdenum nano-pillars, Int. J. Plast. 28(1) (2012) 46-52.

[64] A. Seeger, L. Hollang, The flow-stress asymmetry of ultra-pure molybdenum single crystals, Mater. Trans., JIM 41(1) (2000) 141-151.

[65] H. Cosrad, Effect of temperature on yield and flow stress of BCC metals, Philos. Mag. 5(55) (1960) 745-751.

[66] D. Bailey, W. Flanagan, The strain-rate sensitivity of the flow stress for a peierls mechanism, Philos. Mag. 19(162) (1969) 1093-1103.

[67] D. Caillard, An in situ study of hardening and softening of iron by carbon interstitials, Acta Mater. 59(12) (2011) 4974-4989.

[68] D. Caillard, A TEM in situ study of alloying effects in iron. I—Solid solution softening caused by low concentrations of Ni, Si and Cr, Acta Mater. 61(8) (2013) 2793-2807.

[69] D. Brunner, J. Diehl, The Effect of Atomic Lattice Defects on the Softening Phenomena of High‐Purity α‐Iron, physica status solidi (a) 160(2) (1997) 355-372.

[70] D. Caillard, On the stress discrepancy at low-temperatures in pure iron, Acta Mater. 62 (2014) 267-275.

[71] D. Rodney, J. Bonneville, Dislocations, Physical Metallurgy, Elsevier2014, pp. 1591-1680.

[72] V. Vitek, R. Perrin, D. Bowen, The core structure of ½ (111) screw dislocations in bcc crystals, Philos. Mag. 21(173) (1970) 1049-1073.

[73] V. Vitek, Structure of dislocation cores in metallic materials and its impact on their plastic behaviour, Prog. Mater. Sci. 36 (1992) 1-27.

[74] V. Vitek, Core structure of screw dislocations in body-centred cubic metals: relation to symmetry and interatomic bonding, Philos. Mag. 84(3-5) (2004) 415-428.

[75] M.a.-S. Duesbery, V. Vitek, Plastic anisotropy in bcc transition metals, Acta Mater. 46(5) (1998) 1481-1492.

[76] S.L. Frederiksen, K.W. Jacobsen, Density functional theory studies of screw dislocation core structures in bcc metals, Philos. Mag. 83(3) (2003) 365-375.

[77] F. Nabarro, Fifty-year study of the Peierls-Nabarro stress, Mater. Sci. Eng., A 234 (1997) 67-76.

[78] E. Schmid, W. Boas, Plasticity of crystals, Springer US 1968.

[79] R. Peierls, The size of a dislocation, Proceedings of the Physical Society 52(1) (1940) 34.

[80] F. Nabarro, Dislocations in a simple cubic lattice, Proceedings of the Physical Society 59(2) (1947) 256.

[81] S. Takeuchi, E. Kuramoto, Thermally activated motion of a screw dislocation in a model bcc crystal, J. Phys. Soc. Jpn. 38(2) (1975) 480-487.

[82] M. Mendelev, S. Han, D. Srolovitz, G. Ackland, D. Sun, M. Asta, Development of new interatomic potentials appropriate for crystalline and liquid iron, Philos. Mag. 83(35) (2003) 3977-3994.

[83] L. Ventelon, F. Willaime, Core structure and Peierls potential of screw dislocations in α-Fe from first principles: cluster versus dipole approaches, J. Comput. Aided Mater. Des. 14(1) (2007) 85-94.

[84] D. Rodney, L. Proville, Stress-dependent Peierls potential: Influence on kink-pair activation, Phys. Rev. B 79(9) (2009) 094108.

[85] D. Caillard, J.-L. Martin, Thermally activated mechanisms in crystal plasticity, Elsevier 2003.

[86] T. Suzuki, Y. Kamimura, H. Kirchner, Plastic homology of bcc metals, Philos. Mag. A 79(7) (1999) 1629-1642.

[87] I. Shin, E.A. Carter, Possible origin of the discrepancy in Peierls stresses of fcc metals: First-principles simulations of dislocation mobility in aluminum, Phys. Rev. B 88(6) (2013) 064106.

[88] D.L. Olmsted, K.Y. Hardikar, R. Phillips, Lattice resistance and Peierls stress in finite size atomistic dislocation simulations, Modell. Simul. Mater. Sci. Eng. 9(3) (2001) 215.

[89] Y. Kamimura, K. Edagawa, S. Takeuchi, Experimental evaluation of the Peierls stresses in a variety of crystals and their relation to the crystal structure, Acta Mater. 61(1) (2013) 294-309.

[90] M. Wen, A. Ngan, Atomistic simulation of kink-pairs of screw dislocations in body-centred cubic iron, Acta Mater. 48(17) (2000) 4255-4265.

[91] A. Kraych, P. Carrez, P. Cordier, On dislocation glide in MgSiO3 bridgmanite at high-pressure and high-temperature, Earth. Planet. Sci. Lett. 452 (2016) 60-68.

[92] J.E. Dora, S. Rajnak, Nucleation of kink pairs and the Peierls' mechanism of plastic deformation, Lawrence Berkeley National Laboratory, 1963.

[93] H. Conrad, Thermally activated deformation of metals, JOM 16(7) (1964) 582-588.

[94] K. Hoge, A. Mukherjee, The temperature and strain rate dependence of the flow stress of tantalum, J. Mater. Sci. 12(8) (1977) 1666-1672.

[95] A.A. Griffith, VI. The phenomena of rupture and flow in solids, Philosophical transactions of the royal society of london. Series A, containing papers of a mathematical or physical character 221(582-593) (1921) 163-198.

[96] G. Irwin, TlFracture Dynamics,! 1 Fracture of Metals (Symposium), Am. Soc. Metals, Cleveland (1948) 147-166.

[97] E. Orowan, Fracture and strength of solids, Rep. Prog. Phys. 12(1) (1949) 185.

[98] G.R. Irwin, Onset of fast crack propagation in high strength steel and aluminum alloys [Report], Naval Research Lab Washington DC, 1956.

[99] H.M. Westergaard, Bearing pressures and cracks, Trans AIME, J. Appl. Mech. 6 (1939) 49-53.

[100] G.R. Irwin, Analysis of stresses and strains near the end of a crack transversing a plate, Trans. ASME, Ser. E, J. Appl. Mech. 24 (1957) 361-364.

[101] I.N. Sneddon, The distribution of stress in the neighbourhood of a crack in an elastic solid, Proceedings of the Royal Society of London. Series A. Mathematical and Physical Sciences 187(1009) (1946) 229-260.

[102] J.R. Rice, A path independent integral and the approximate analysis of strain concentration by notches and cracks [J], (1968).

[103] J. Hutchinson, Singular behavior at the end of a tensile crack in hardening material, J. Mech. Phys. Solids 16(1) (1968) 13-31.

[104] J. Rice, G.F. Rosengren, Plane strain deformation near a crack tip in a power-law hardening material, J. Mech. Phys. Solids 16(1) (1968) 1-12.

[105] E. Astm, 399-90:" Standard test method for plane-strain fracture toughness of metallic materials, Annual book of ASTM standards 3(01) (1997) 506-536.

[106] A. Standard, Standard test method for measurement of fracture toughness, ASTM, E1820-01 (2001) 1-46.

[107] K. Jonnalagadda, S.W. Cho, I. Chasiotis, T. Friedmann, J. Sullivan, Effect of intrinsic stress gradient on the effective mode-I fracture toughness of amorphous diamond-like carbon films for MEMS, J. Mech. Phys. Solids 56(2) (2008) 388-401.

[108] D.H. Alsem, O.N. Pierron, E.A. Stach, C.L. Muhlstein, R.O. Ritchie, Mechanisms for fatigue of micron‐scale silicon structural films, Adv. Eng. Mater. 9(1‐2) (2007) 15-30.

[109] S. Kalácska, J. Ast, P.D. Ispánovity, J. Michler, X. Maeder, 3D HR-EBSD Characterization of the plastic zone around crack tips in tungsten single crystals at the micron scale, Acta Mater. 200 (2020) 211-222.

[110] A. Kumar, A. Saxena, C. Kirchlechner, M. Herbig, S. Brinckmann, R. Petrov, J. Sietsma, In situ study on fracture behaviour of white etching layers formed on rails, Acta Mater. 180 (2019) 60-72.

[111] J. Ast, M. Göken, K. Durst, Size-dependent fracture toughness of tungsten, Acta Mater. 138 (2017) 198-211.

[112] M. Sebastiani, K. Johanns, E.G. Herbert, F. Carassiti, G.M. Pharr, A novel pillar indentation splitting test for measuring fracture toughness of thin ceramic coatings, Philos. Mag. 95(16-18) (2015) 1928-1944.

[113] B.N. Jaya, C. Kirchlechner, G. Dehm, Can microscale fracture tests provide reliable fracture toughness values? A case study in silicon, J. Mater. Res. 30(5) (2015) 686.

[114] S. Liu, J. Wheeler, P. Howie, X. Zeng, J. Michler, W. Clegg, Measuring the fracture resistance of hard coatings, Appl. Phys. Lett. 102(17) (2013) 171907.

[115] S. Massl, W. Thomma, J. Keckes, R. Pippan, Investigation of fracture properties of magnetron-sputtered TiN films by means of a FIB-based cantilever bending technique, Acta Mater. 57(6) (2009) 1768-1776.

[116] A.K. Saxena, A. Kumar, M. Herbig, S. Brinckmann, G. Dehm, C. Kirchlechner, Micro fracture investigations of white etching layers, Materials & Design 180 (2019) 107892.

[117] R. Pippan, S. Wurster, D. Kiener, Fracture mechanics of micro samples: fundamental considerations, Materials & Design 159 (2018) 252-267.

[118] G. Dehm, B.N. Jaya, R. Raghavan, C. Kirchlechner, Overview on micro-and nanomechanical testing: New insights in interface plasticity and fracture at small length scales, Acta Mater. 142 (2018) 248-282.

[119] F. Hofmann, E. Tarleton, R.J. Harder, N.W. Phillips, P.-W. Ma, J.N. Clark, I.K. Robinson, B. Abbey, W. Liu, C.E. Beck, 3D lattice distortions and defect structures in ion-implanted nano-crystals, Sci. Rep. 7 (2017) 45993.

[120] J.P. Best, J. Zechner, I. Shorubalko, J.V. Oboňa, J. Wehrs, M. Morstein, J. Michler, A comparison of three different notching ions for small-scale fracture toughness measurement, Scripta Mater. 112 (2016) 71-74.

[121] S. Brinckmann, K. Matoy, C. Kirchlechner, G. Dehm, On the influence of microcantilever pre-crack geometries on the apparent fracture toughness of brittle materials, Acta Mater. 136 (2017) 281-287.

[122] K. Matoy, H. Schönherr, T. Detzel, T. Schöberl, R. Pippan, C. Motz, G. Dehm, A comparative micro-cantilever study of the mechanical behavior of silicon based passivation films, Thin Solid Films 518(1) (2009) 247-256.

[123] I. Gutierrez-Urrutia, S. Zaefferer, D. Raabe, Electron channeling contrast imaging of twins and dislocations in twinning-induced plasticity steels under controlled diffraction conditions in a scanning electron microscope, Scripta Mater. 61(7) (2009) 737-740.

[124] J.-l. Zhang, S. Zaefferer, D. Raabe, A study on the geometry of dislocation patterns in the surrounding of nanoindents in a TWIP steel using electron channeling contrast imaging and discrete dislocation dynamics simulations, Mater. Sci. Eng., A 636 (2015) 231-242.

[125] S. Zaefferer, N.-N. Elhami, Theory and application of electron channelling contrast imaging under controlled diffraction conditions, Acta Mater. 75 (2014) 20-50.

[126] A. Melmed, M. Martinka, S. Girvin, T. Sakurai, Y. Kuk, Analysis of high resistivity semiconductor specimens in an energy‑compensated time‑of‑flight atom probe, Appl. Phys. Lett. 39(5) (1981) 416-417.

[127] M. Gilbert, F. Vurpillot, A. Vella, H. Bernas, B. Deconihout, Some aspects of the silicon behaviour under femtosecond pulsed laser field evaporation, Ultramicroscopy 107(9) (2007) 767-772.

[128] B. Gault, M. Müller, A. La Fontaine, M. Moody, A. Shariq, A. Cerezo, S. Ringer, G. Smith, Influence of surface migration on the spatial resolution of pulsed laser atom probe tomography, J. Appl. Phys. 108(4) (2010) 044904.

[129] Y. Li, D. Ponge, P. Choi, D. Raabe, Segregation of boron at prior austenite grain boundaries in a quenched martensitic steel studied by atom probe tomography, Scripta Mater. 96 (2015) 13-16.

[130] Y. Li, M. Herbig, S. Goto, D. Raabe, Atomic scale characterization of white etching area and its adjacent matrix in a martensitic 100Cr6 bearing steel, Mater. Charact. 123 (2017) 349-353.

[131] C.C. Tasan, M. Diehl, D. Yan, M. Bechtold, F. Roters, L. Schemmann, C. Zheng, N. Peranio, D. Ponge, M. Koyama, K. Tsuzaki, D. Raabe, An Overview of Dual-Phase Steels: Advances in Microstructure-Oriented Processing and Micromechanically Guided Design, Annual Review of Materials Research 45(1) (2015) 391-431.

[132] V.L. de la Concepción, H.N. Lorusso, H.G. Svoboda, Effect of Carbon Content on Microstructure and Mechanical Properties of Dual Phase Steels, Procedia Materials Science 8 (2015) 1047-1056.

[133] A. Ghatei Kalashami, A. Kermanpur, E. Ghassemali, A. Najafizadeh, Y. Mazaheri, Correlation of microstructure and strain hardening behavior in the ultrafine-grained Nb-bearing dual phase steels, Mater. Sci. Eng., A 678 (2016) 215-226.

[134] Q. Lai, O. Bouaziz, M. Gouné, L. Brassart, M. Verdier, G. Parry, A. Perlade, Y. Bréchet, T. Pardoen, Damage and fracture of dual-phase steels: Influence of martensite volume fraction, Mater. Sci. Eng., A 646 (2015) 322-331.

[135] J. Kang, Y. Ososkov, J. Embury, D. Wilkinson, Digital image correlation studies for microscopic strain distribution and damage in dual phase steels, Scripta Mater. 56(11) (2007) 999-1002.

[136] C.C. Tasan, J.P.M. Hoefnagels, M. Diehl, D. Yan, F. Roters, D. Raabe, Strain localization and damage in dual phase steels investigated by coupled in-situ deformation experiments and crystal plasticity simulations, Int. J. Plast. 63 (2014) 198-210.

[137] C.C. Tasan, M. Diehl, D. Yan, C. Zambaldi, P. Shanthraj, F. Roters, D. Raabe, Integrated experimental–simulation analysis of stress and strain partitioning in multiphase alloys, Acta Mater. 81 (2014) 386-400.

[138] S.S. J. Kadkhodapour, D. Raabe, S. Ziaei-Rad, U. Weber, M. Calcagnotto, Experimental and numerical study on geometrically necessary dislocations and non-homogeneous mechanical properties of the ferrite phase in dual phase steels, Acta Mater. 59(11) (2011) 4387-4394.

[139] J. Zhou, A.M. Gokhale, A. Gurumurthy, S.P. Bhat, Realistic microstructural RVE-based simulations of stress–strain behavior of a dual-phase steel having high martensite volume fraction, Mater. Sci. Eng., A 630 (2015) 107-115.

[140] H.J. Bong, H. Lim, M.-G. Lee, D.T. Fullwood, E.R. Homer, R.H. Wagoner, An RVE procedure for micromechanical prediction of mechanical behavior of dual-phase steel, Mater. Sci. Eng., A 695 (2017) 101-111.

[141] A. Srivastava, H. Ghassemi-Armaki, H. Sung, P. Chen, S. Kumar, A.F. Bower, Micromechanics of plastic deformation and phase transformation in a three-phase TRIP-assisted advanced high strength steel: Experiments and modeling, J. Mech. Phys. Solids 78 (2015) 46-69.

[142] P.C. Hassan Ghassemi-Armaki, Shrikant Bhat, Sriram Sadagopan, Sharvan Kumar, Allan Bower, Microscale-calibrated modeling of the deformation response of low-carbon martensite, Acta Mater. 61(10) (2013) 3640-3652.

[143] H. Ghassemi-Armaki, R. Maaß, S.P. Bhat, S. Sriram, J.R. Greer, K.S. Kumar, Deformation response of ferrite and martensite in a dual-phase steel, Acta Mater. 62 (2014) 197-211.

[144] P. Chen, H. Ghassemi-Armaki, S. Kumar, A. Bower, S. Bhat, S. Sadagopan, Microscale-calibrated modeling of the deformation response of dual-phase steels, Acta Mater. 65 (2014) 133-149.

[145] D.D. Tjahjanto, P. Eisenlohr, F. Roters, Multiscale deep drawing analysis of dual-phase steels using grain cluster-based RGC scheme, Modell. Simul. Mater. Sci. Eng. 23(4) (2015).

[146] B. Mohammed, T. Park, F. Pourboghrat, J. Hu, R. Esmaeilpour, F. Abu-Farha, Multiscale crystal plasticity modeling of multiphase advanced high strength steel, International Journal of Solids and Structures 151 (2018) 57-75.

[147] E.-Y. Kim, S.-H. Choi, E.-J. Shin, J. Yoon, Simulation of earing behaviors in bake hardening steel exhibiting a strong off-γ-fiber component, International Journal of Solids and Structures 49(25) (2012) 3573-3581.

[148] M.D. Uchic, D.M. Dimiduk, J.N. Florando, W.D. Nix, Sample dimensions influence strength and crystal plasticity, Science 305(5686) (2004) 986-989.

[149] J.R. Greer, J.T.M. De Hosson, Plasticity in small-sized metallic systems: Intrinsic versus extrinsic size effect, Prog. Mater. Sci. 56(6) (2011) 654-724.

[150] G. Dehm, B.N. Jaya, R. Raghavan, C. Kirchlechner, Overview on micro- and nanomechanical testing: New insights in interface plasticity and fracture at small length scales, Acta Mater. 142 (2018) 248-282.

[151] K.S. Ng, A.H.W. Ngan, Breakdown of Schmid's law in micropillars, Scripta Mater. 59(7) (2008) 796-799.

[152] J. Senger, D. Weygand, P. Gumbsch, O. Kraft, Discrete dislocation simulations of the plasticity of micro-pillars under uniaxial loading, Scripta Mater. 58(7) (2008) 587-590.

[153] C. Du, J.P.M. Hoefnagels, R. Vaes, M.G.D. Geers, Plasticity of lath martensite by sliding of substructure boundaries, Scripta Mater. 120 (2016) 37-40.

[154] K. Kwak, T. Mayama, Y. Mine, K. Takashima, Anisotropy of strength and plasticity in lath martensite steel, Mater. Sci. Eng., A 674 (2016) 104-116.

[155] Y. Mine, K. Hirashita, H. Takashima, M. Matsuda, K. Takashima, Micro-tension behaviour of lath martensite structures of carbon steel, Mater. Sci. Eng., A 560 (2013) 535-544.

[156] A. Ngan, A generalized Peierls-Nabarro model for nonplanar screw dislocation cores, J. Mech. Phys. Solids 45(6) (1997) 903-921.

[157] F.R.N. Nabarro, Fifty-year study of the Peierls-Nabarro stress, Mater. Sci. Eng., A 234-236 (1997) 67-76.

[158] A. Koester, A. Ma, A. Hartmaier, Atomistically informed crystal plasticity model for body-centered cubic iron, Acta Mater. 60(9) (2012) 3894-3901.

[159] C. Du, F. Maresca, M.G.D. Geers, J.P.M. Hoefnagels, Ferrite slip system activation investigated by uniaxial micro-tensile tests and simulations, Acta Mater. 146 (2018) 314-327.

[160] A.B. Hagen, B.D. Snartland, C. Thaulow, Temperature and orientation effects on the deformation mechanisms of α-Fe micropillars, Acta Mater. 129 (2017) 398-407.

[161] A.B. Hagen, C. Thaulow, Low temperature in-situ micro-compression testing of iron pillars, Mater. Sci. Eng., A 678 (2016) 355-364.

[162] P. Franciosi, L.T. Le, G. Monnet, C. Kahloun, M.H. Chavanne, Investigation of slip system activity in iron at room temperature by SEM and AFM in-situ tensile and compression tests of iron single crystals, Int. J. Plast. 65 (2015) 226-249.

[163] D. Caillard, A TEM in situ study of alloying effects in iron. II—Solid solution hardening caused by high concentrations of Si and Cr, Acta Mater. 61(8) (2013) 2808-2827.

[164] M.R. Gilbert, S. Queyreau, J. Marian, Stress and temperature dependence of screw dislocation mobility inα-Fe by molecular dynamics, Phys. Rev. B 84(17) (2011).

[165] L. Ventelon, F. Willaime, E. Clouet, D. Rodney, Ab initio investigation of the Peierls potential of screw dislocations in bcc Fe and W, Acta Mater. 61(11) (2013) 3973-3985.

[166] A.H.W.N. M. Wen, Atomistic simulation of kink-pairs of screw dislocations in body-centred cubic iron, Acta Mater. 48(17) 4255-4265.

[167] L.M. Hale, J.A. Zimmerman, C.R. Weinberger, Simulations of bcc tantalum screw dislocations: Why classical inter-atomic potentials predict {112} slip, Computational Materials Science 90 (2014) 106-115.

[168] H. Lim, L.M. Hale, J.A. Zimmerman, C.C. Battaile, C.R. Weinberger, A multi-scale model of dislocation plasticity in α-Fe: Incorporating temperature, strain rate and non-Schmid effects, Int. J. Plast. 73 (2015) 100-118.

[169] C.A. Volkert, E.T. Lilleodden, Size effects in the deformation of sub-micron Au columns, Philos. Mag. 86(33-35) (2006) 5567-5579.

[170] D.M. Dimiduk, M.D. Uchic, T.A. Parthasarathy, Size-affected single-slip behavior of pure nickel microcrystals, Acta Mater. 53(15) (2005) 4065-4077.

[171] H. Bei, S. Shim, G.M. Pharr, E.P. George, Effects of pre-strain on the compressive stress–strain response of Mo-alloy single-crystal micropillars, Acta Mater. 56(17) (2008) 4762-4770.

[172] K.E.J. P. Sudharshan Phani, G. Duscher, A. Gali, E.P. George, G.M. Pharr, Scanning transmission electron microscope observations of defects in as-grown and pre-strained Mo alloy fibers, Acta Mater. 59(5) (2011) 2172-2179.

[173] M. Umemoto, E. Yoshitake, I. Tamura, The morphology of martensite in Fe-C, Fe-Ni-C and Fe-Cr-C alloys, J. Mater. Sci. 18(10) (1983) 2893-2904.

[174] H. Kim, F. Barlat, Y. Lee, S.B. Zaman, C.S. Lee, Y. Jeong, A crystal plasticity model for describing the anisotropic hardening behavior of steel sheets during strain-path changes, Int. J. Plast. 111 (2018) 85-106.

[175] C. Scott, B.S. Amirkhiz, I. Pushkareva, F. Fazeli, S. Allain, H. Azizi, New insights into martensite strength and the damage behaviour of dual phase steels, Acta Mater. 159 (2018) 112-122.

[176] C. Tian, D. Ponge, L. Christiansen, C. Kirchlechner, On the mechanical heterogeneity in dual phase steel grades: Activation of slip systems and deformation of martensite in DP800, Acta Mater. 183 (2020) 274-284.

[177] E. Kuramoto, Y. Aono, K. Kitajima, Thermally activated slip deformation of high purity iron single crystals between 4.2 K and 300 K, Scr. Metall. 13(11) (1979) 1039-1042.

[178] W. Spitzig, A. Keh, Orientation dependence of the strain-rate sensitivity and thermally activated flow in iron single crystals, Acta Metall. 18(9) (1970) 1021-1033.

[179] T. Suzuki, S. Takeuchi, H. Yoshinaga, Dislocation dynamics and plasticity, Springer Science & Business Media 2013.

[180] K. Srivastava, D. Weygand, P. Gumbsch, Dislocation junctions as indicators of elementary slip planes in body-centered cubic metals, J. Mater. Sci. 49(20) (2014) 7333-7337.

[181] H.D. Nine, Slip planes and asymmetric slip in fatigue of iron single crystals, Philos. Mag. 26(6) (1972) 1409-1418.

[182] A. Opinsky, R. Smoluchowski, The Crystallographic Aspect of Slip in Body‐Centered Cubic Single Crystals. II. Interpretation of Experiments, J. Appl. Phys. 22(12) (1951) 1488-1492.

[183] G. Malygin, Analysis of the strain-rate sensitivity of flow stresses in nanocrystalline FCC and BCC metals, Phys. Solid State 49(12) (2007) 2266-2273.

[184] C. Tian, D. Ponge, L. Christiansen, C. Kirchlechner, On the mechanical heterogeneity in dual phase steel grades: Activation of slip systems and deformation of martensite in DP800, Acta Mater. (2019).

[185] D. Stein, The effect of carbon on the strain-rate sensitivity of iron single crystals, Acta Metall. 14(2) (1966) 99-104.

[186] T. Altshuler, J.W. Christian, The mechanical properties of pure iron tested in compression over the temperature range 2 to 293° K, Philos. Trans. R. Soc. London, Ser. A 261(1121) (1967) 253-287.

[187] R.T. Sato, A.K. Mukherjee, The asymmetric temperature dependence of yield stress in tantalum single crystals at low temperatures, Mater.Sci. 8(2) (1971) 74-82.

[188] G. Taylor, Thermally-activated deformation of BCC metals and alloys, Prog. Mater. Sci. 36 (1992) 29-61.

[189] W. Spitzig, A. Keh, The role of internal and effective stresses in the plastic flow of iron single crystals, Metall. Trans. 1(12) (1970) 3325.

[190] J. Marian, W. Cai, V.V. Bulatov, Dynamic transitions from smooth to rough to twinning in dislocation motion, Nat. 3(3) (2004) 158.

[191] T. Suzuki, H. Koizumi, H.O. Kirchner, Plastic flow stress of bcc transition metals and the Peierls potential, Acta metallurgica et materialia 43(6) (1995) 2177-2187.

[192] M. Gilbert, S. Queyreau, J. Marian, Stress and temperature dependence of screw dislocation mobility in α-Fe by molecular dynamics, Phys. Rev. B 84(17) (2011) 174103.

[193] Y. Cui, G. Po, N. Ghoniem, Temperature insensitivity of the flow stress in body-centered cubic micropillar crystals, Acta Mater. 108 (2016) 128-137.

[194] J. Chaussidon, M. Fivel, D. Rodney, The glide of screw dislocations in bcc Fe: atomistic static and dynamic simulations, Acta Mater. 54(13) (2006) 3407-3416.

[195] C. Kusche, T. Reclik, M. Freund, T. Al-Samman, U. Kerzel, S. Korte-Kerzel, Large-area, high-resolution characterisation and classification of damage mechanisms in dual-phase steel using deep learning, PLoS One 14(5) (2019).

[196] T. Sirinakorn, S. Wongwises, V. Uthaisangsuk, A study of local deformation and damage of dual phase steel, Materials & Design 64 (2014) 729-742.

[197] H. Ghassemi-Armaki, R. Maaß, S. Bhat, S. Sriram, J. Greer, K. Kumar, Deformation response of ferrite and martensite in a dual-phase steel, Acta Mater. 62 (2014) 197-211.

[198] Y. Wang, R. Fritz, D. Kiener, J. Zhang, G. Liu, O. Kolednik, R. Pippan, J. Sun, Fracture behavior and deformation mechanisms in nanolaminated crystalline/amorphous micro-cantilevers, Acta Mater. 180 (2019) 73-83.

[199] B.N. Jaya, C. Kirchlechner, G. Dehm, Can microscale fracture tests provide reliable fracture toughness values? A case study in silicon, J. Mater. Res. 30(5) (2015) 686-698.

[200] R. Dolby, K. JF, Toughness of martensitic and martensitic-bainitic microstructures with particular reference to heat affected zones in welded low alloy steels [J], (1972).

[201] S. Li, G. Zhu, Y. Kang, Effect of substructure on mechanical properties and fracture behavior of lath martensite in 0.1 C–1.1 Si–1.7 Mn steel, J. Alloys Compd. 675 (2016) 104-115.

[202] Y. Liang, S. Long, P. Xu, Y. Lu, Y. Jiang, Y. Liang, M. Yang, The important role of martensite laths to fracture toughness for the ductile fracture controlled by the strain in EA4T axle steel, Mater. Sci. Eng., A 695 (2017) 154-164.

[203] A. Standard, E399-90, Standard Test Method for Plane Strain Fracture Toughness of Metallic Materials. Philadelphia: American Society for Testing and Materials (1993).

[204] J. Ast, M. Ghidelli, K. Durst, M. Göken, M. Sebastiani, A. Korsunsky, A review of experimental approaches to fracture toughness evaluation at the micro-scale, Materials & Design 173 (2019) 107762.

[205] N. Vajragupta, V. Uthaisangsuk, B. Schmaling, S. Münstermann, A. Hartmaier, W. Bleck, A micromechanical damage simulation of dual phase steels using XFEM, Computational Materials Science 54 (2012) 271-279.

[206] O. Towers, S. Garwood, Influence of crack depth on resistance curves for three-point bend specimens in HY130, Fracture Mechanics: Seventeenth Volume, ASTM International 1986.

[207] X.-K. Zhu, J.A. Joyce, Review of fracture toughness (G, K, J, CTOD, CTOA) testing and standardization, Eng. Fract. Mech. 85 (2012) 1-46.

[208] J. Krawczyk, J. Pacyna, P. Bała, Fracture toughness of steels with nickel content in respect of carbide morphology, Mater. Sci. Technol. 31(7) (2015) 795-802.

[209] E. Pavlina, C. Van Tyne, Correlation of yield strength and tensile strength with hardness for steels, J. Mater. Eng. Perform. 17(6) (2008) 888-893.

[210] B.N. Jaya, S. Goto, G. Richter, C. Kirchlechner, G. Dehm, Fracture behavior of nanostructured heavily cold drawn pearlitic steel wires before and after annealing, Mater. Sci. Eng., A 707 (2017) 164-171.

[211] Y. Li, D. Raabe, M. Herbig, P.-P. Choi, S. Goto, A. Kostka, H. Yarita, C. Borchers, R. Kirchheim, Segregation stabilizes nanocrystalline bulk steel with near theoretical strength, Phys. Rev. Lett. 113(10) (2014) 106104.

[212] C. Du, J. Hoefnagels, R. Vaes, M. Geers, Block and sub-block boundary strengthening in lath martensite, Scripta Mater. 116 (2016) 117-121.

[213] A. Hohenwarter, B. Völker, M.W. Kapp, Y. Li, S. Goto, D. Raabe, R. Pippan, Ultra-strong and damage tolerant metallic bulk materials: a lesson from nanostructured pearlitic steel wires, Sci. Rep. 6 (2016) 33228.

[214] M. Calcagnotto, Y. Adachi, D. Ponge, D. Raabe, Deformation and fracture mechanisms in fine-and ultrafine-grained ferrite/martensite dual-phase steels and the effect of aging, Acta Mater. 59(2) (2011) 658-670.

[215] M. Ayatollahi, A.C. Darabi, H. Chamani, J. Kadkhodapour, 3D micromechanical modeling of failure and damage evolution in dual phase steel based on a real 2D microstructure, Acta Mechanica Solida Sinica 29(1) (2016) 95-110.

[216] A. Ramazani, Z. Ebrahimi, U. Prahl, Study the effect of martensite banding on the failure initiation in dual-phase steel, Computational materials science 87 (2014) 241-247.

126

Curriculum Vitae

Personal Information

Name: Chunhua Tian

Place and date of Birth: China | 22.05.1990

Address: Langerstraße 44, 40233 Düsseldorf

Phone: +49 176 5780 8591

Email： c.tian.mse@gmail.com

Education

03/2017-present *PhD* in Max-Planck-Institut für Eisenforschung, Düsseldorf

Dissertation: On the Damage Initiation of Dual Phase steels: Quantitative Insights from *in situ* micromechanics

09/2013-08/2016 *M.Sc.* in Metallurgical Engineering, RWTH Aachen University

Concentration: Physical Metallurgy

Grade: 1.6

09/ 2009-07/2013 *B.Sc.* in Materials Science and Engineering, University of Science and Technology Beijing (USTB, China)

GPA: 3.7/4.0 (4.0 corresponds to 1.0 in Germany)

Work Experiences

PhD in Max-Planck-Institut für Eisenforschung GmbH Düsseldorf, March 2017 – present
Responsibilities:

- Preparation of micro specimens (micro pillars and micro cantilevers) extracting ferrite and martensite in DP steels with FIB

- Plasticity investigation of component phases by *in situ* micro pillar compression tests

- Fracture initiation toughness evaluation of martensite islands through *in situ* micro cantilever bending tests

- Microstructure observation by SEM, pillar orientation determination by EBSD and dislocation distribution by ECCI

- Elements' distribution investigation through APT

- Data analysis, especially with Programming script in Mathematica

Master thesis in Gießerei Institut, RWTH Aachen, 02/2016-08/2016

Responsibilities:

- In vitro immersion corrosion tests of magnesium alloys in different solutions
- Investigation of top view and cross section after corrosion processes by SEM
- Identification of corrosion products through EDX and XRD

Intern in Selective Laser Melting (SLM) Group in Fraunhofer Institut für Lasertechnik (ILT) Aachen, 05/2015-10/2015

Responsibilities:

- Specimen manufacture of nickel based alloys through SLM technique
- Porosity investigation and morphology observation on formed melting pools
- Crack causes' analysis in specimens produced by SLM process

Minithesis in Institut für Eisenhüttenkunde, RWTH Aachen, 08/2014-02/2015

Responsibilities:

- Construction of 2D RVE based on SEM micrographs
- Tensile test simulation using Abaqus 13.0 combined constitutive equations
- Parameters optimization by comparing results of simulation and of tensile experiments

Bachelor thesis in Materials Science and Engineering Institute, USTB China, 02/2013-06/2013

Responsibilities:

- Analysis of grain size variation on the turbine plate (nickel based GH4169)
- Investigation on microstructure evolution, especially the strengthening precipitates $\gamma^{'}$ and $\gamma^{''}$, with different aging time and aging temperature
- Hardness measurement with aging conditions
- Comparison of GH4169 and In718 plus regarding microstructure evolution and hardness

Publications

Tian, C., Ponge, D., Christiansen, L., & Kirchlechner, C. (2020). On the mechanical heterogeneity in dual phase steel grades: Activation of slip systems and deformation of martensite in DP800. Acta Materialia, 183, 274-284.

Kusche, C. F., Dunlap, A., Pütz, F., *Tian, C.*, Kirchlechner, C., Aretz, A., ... & Korte-Kerzel, S. (2020). Efficient characterization tools for deformation-induced damage at different scales.

Production Engineering, 14(1), 95-104.

Tian, C., Dehm, G., Kirchlechner, C., Influence of strain rate on the activation of {110}, {112}, {123} slip in ferrite of DP800 [J]. Materialia, 2021, 15: 100983.

Tian, C., Kirchlechner, C., The fracture toughness of martensite islands in dual phase DP800 steel, Journal of Materials Research, accepted.

Tian, C., Kusche, C. F., Korte-Kertel, S., Al-Samman, T., Kirchlechner, C., Influence of work hardening potential of ferrite on damage growth in DP800, in preparation

Awards

2012	*Third Class of People Scholarship, China*
2011	*Kennametal* Scholarship*, China*
2010-2011	*Excellent Student Award, China*

EXTRA

Languages	Chinese: native speaker
	English: fluent
	German: good (C1)
IT Skills	MS-Office (Word, Excel, PPT): advanced level
	Mathematica: Since 2017
Driving	German license B1
Hobby	Singing, cooking, swimming, badminton